



RESEARCH MEMORANDUM

A COMPARISON AT MACH NUMBERS UP TO 0.92 OF THE
CALCULATED AND EXPERIMENTAL DOWNWASH
AND WAKE CHARACTERISTICS AT VARIOUS
HORIZONTAL TAIL HEIGHTS BEHIND A
WING WITH 45° OF SWEETBACK

By Jack D. Stephenson, Ralph Selan,
and Angelo Bandettini

Ames Aeronautical Laboratory
Moffett Field, Calif.

NATIONAL ADVISORY COMMITTEE
FOR AERONAUTICS
WASHINGTON

June 28, 1955
Declassified April 15, 1958

NATIONAL ADVISORY COMMITTEE FOR AERONAUTICS

RESEARCH MEMORANDUM

A COMPARISON AT MACH NUMBERS UP TO 0.92 OF THE
CALCULATED AND EXPERIMENTAL DOWNWASH
AND WAKE CHARACTERISTICS AT VARIOUS
HORIZONTAL TAIL HEIGHTS BEHIND A
WING WITH 45° OF SWEETBACK

By Jack D. Stephenson, Ralph Selan,
and Angelo Bandettini

SUMMARY

Wind-tunnel tests were conducted at Mach numbers from 0.25 to 0.92 to measure downwash and dynamic pressure in the region of the tail of a wing-fuselage-tail model having a wing with 45° of sweepback, an aspect ratio of 5.5, and NACA 64AO10 sections normal to the quarter-chord line. The data were analyzed in order to determine the origin and character of variations in the contribution of the horizontal tail to static longitudinal stability observed in tests of the model with the tail in various vertical positions. The spanwise distribution of downwash at the tail and the effect of tail height on downwash were not accurately predicted by a theory in which it is assumed that horseshoe vortices are distributed along the wing quarter-chord line and that there is no rolling-up of the vortex sheet. A somewhat improved prediction of the spanwise distribution of downwash was provided by an approximate theory based on the flow induced by a single swept vortex, but this theory still did not predict the large downwash at high angles of attack that were observed experimentally at the higher tail positions.

INTRODUCTION

Results of an investigation of the static longitudinal stability of a wing-fuselage-tail model having a wing swept back 45° and an aspect ratio of 5.5 were presented in reference 1. The model (which is the same as that used in the tests reported herein) had a severe longitudinal instability resulting from an extreme forward movement of the center of pressure of the wing with increasing lift coefficient. Reference 1 indicates that this instability, which is a characteristic of wings of this general plan form, might either be seriously aggravated or somewhat ameliorated, depending upon the choice of the vertical location of the

horizontal tail. When the tail was added below the wing chord plane, it provided a nearly uniform positive contribution to stability, but as the tail height was increased progressively to 0.255 semispan above the wing chord plane, the tail produced increasingly powerful positive pitching moments at high angles of attack.

In order to study in more detail the characteristics of the flow that caused the large variations in tail contribution to stability, dynamic-pressure surveys and downwash-angle surveys have been made in the region of the various horizontal tails. These surveys were made both with and without wing fences, since tests showed that the fences had a significant effect upon the tail contribution to stability.

The downwash behind the model without fences has been calculated in the region of the tail, and the results are compared with the measured downwash angles and with the effective downwash. One objective of this comparison was to determine whether a simple mathematical approximation assumed to represent the flow behind a wing with an extensive region of tip stall might be used to predict the effect of tail height on tail contribution to stability at high angles of attack.

NOTATION

b	wing span
b_t	tail span
c	local wing chord parallel to the plane of symmetry
\bar{c}	wing mean aerodynamic chord, $\bar{c} = \frac{\int_0^{b/2} c^2 dy}{\int_0^{b/2} c dy}$
c_{av}	average wing chord
C_D	drag coefficient, $\frac{\text{drag}}{qS_w}$
C_L	lift coefficient, $\frac{\text{lift}}{qS_w}$
c_l	section lift coefficient
C_m	pitching-moment coefficient about the quarter point of the wing mean aerodynamic chord, $\frac{\text{pitching moment}}{qS_w \bar{c}}$

l	length of body
l_t	tail length, distance from the quarter point of wing mean aerodynamic chord to the quarter point of horizontal-tail mean aerodynamic chord
M	free-stream Mach number
q	free-stream dynamic pressure
q_t	dynamic pressure at the tail
Δq	increment in dynamic pressure, $q_t - q$
R	Reynolds number based on wing mean aerodynamic chord
r	local radius of body
r_0	maximum radius of body
S_w	area of basic semispan wing
S_t	area of semispan tail
V_t	horizontal-tail volume, $\frac{S_t l_t}{S_w C}$
y_0	semispan of swept vortex
z	perpendicular distance from wing chord plane
x, y, z_1	coordinates for the system of wind axes with the origin at the apex of the quarter-chord line
x', y', z_1'	coordinates for the system of wind axes with the origin in the plane of the trailing vortices
α	angle of attack
ϵ	downwash angle
$\eta \frac{q_t}{q}$	product of the tail efficiency and the effective dynamic pressure ratio at the tail

Subscripts

<i>l</i>	local
<i>t</i>	horizontal tail
TE	wing trailing edge
av	average value
<i>u</i>	uncorrected

MODEL AND APPARATUS

Figure 1(a) is a sketch of the model, which was the same as that described in reference 1. Table I lists geometric data for the model. The wing had an aspect ratio of 5.5, a taper ratio of 0.53, and 45° of sweepback at the quarter-chord line. The airfoil normal to the quarter-chord line was the NACA 64A010. During part of the tests, the full-chord fences shown in figure 1(b) were mounted on the wing at two stations, 44 and 69 percent semispan.

Local downwash angles, total pressures, and dynamic pressures were measured in the region of the tail, using a survey rake. This rake consisted of three directional pitot tubes and three rows of pressure tubes (each row containing 25 total-pressure tubes and 6 static-pressure tubes). The survey data were recorded with the directional pitot tubes lying in the wing chord plane and $0.127b/2$ and $0.255b/2$ above this plane. These locations correspond to three of the vertical positions of the horizontal tail which were studied previously in the tests reported in reference 1. Dimensions and details of the rake and of the directional pitot tubes are shown in figures 1(a) and 1(b), and in the photographs presented in figure 2.

TESTS

Experiments were conducted to determine the spanwise distribution of downwash at three positions of the tail. The vertical distributions of total and dynamic pressure were measured at three spanwise stations, $0.10b/2$, $0.24b/2$, and $0.38b/2$, to provide wake profile data in the region of the tail. Downwash and wake data were obtained at Mach numbers from 0.25 to 0.92 and 2 million Reynolds number and at a Mach number of 0.25 and 10 million Reynolds number for the model with and without fences.

In order to observe the progress of separation as stalling occurred, tufts were added to the wing. The model with tufts (with and without fences) was tested at Mach numbers of 0.25, 0.85, 0.9, and 0.92 and 2 million Reynolds number and at a Mach number of 0.25 and 10 million Reynolds number.

CORRECTIONS TO DATA

The test data have been corrected to account for the blockage effects due to the tunnel walls, for tunnel-wall interference effects due to model lift, and for the drag tares associated with the turntable upon which the model was mounted.

Blockage corrections to the test-section Mach number and dynamic pressure were computed by the method given in reference 2 and are shown as functions of the corrected Mach number in table II(a).

The following corrections, calculated as indicated in reference 3, were added, respectively, to the measured angles of attack, pitching-moment coefficients, and drag coefficients, to account for the jet-boundary effect induced by wing lift.

$$\Delta\alpha = K_1 C_L$$

$$\Delta C_m = K_2 C_L \text{ (model without tail)}$$

$$\Delta C_m = K_3 C_L \text{ (model with tail)}$$

$$\Delta C_D = 0.0053 C_L$$

A correction (also calculated using ref. 3) has been applied to account for the tunnel-wall interference effect on the downwash angle measured with flow-angle survey tubes. This correction $\Delta\epsilon_t$ was calculated as follows and added to the measured flow-angle data.

$$\Delta\epsilon_t = K_4 C_L$$

Possible variations of this correction due to varying the position of the tail in relation to the wind-tunnel jet boundaries were neglected. The values of K_1 , K_2 , K_3 , and K_4 are listed in table II(b).

The drag tare corrections, which were subtracted from the measured drag coefficients in order to account for the drag of the exposed area of the turntable are listed in table II(c).

Tests of the isolated rake showed that the static pressures varied with angle of pitch and with position on the rake. In tests of the model,

a correction was applied to the static-pressure data to account for this effect. Since the correction was a function of the rake angle of attack, this angle had to be estimated from the flow-angle data. When the flow angle varied significantly across the rake span (i.e., large lateral variations of downwash) the effect of the flow angles on the dynamic-pressure measurements could only be estimated, so that some errors, believed to be small, were introduced into the values of q_t/q for such conditions.

The vertical location of the wake is influenced by the jet-boundary effect induced by model lift. The amount of displacement of the wake due to this effect was estimated to be small and was neglected.

RESULTS AND DISCUSSION

The lift and pitching-moment characteristics of the model were presented in reference 1 and are again presented for convenience in figures 3 through 8. The data show the effects of adding two full-chord fences and of varying the vertical position of the horizontal tail.

Local Downwash

Figures 9 through 12 show the downwash measured by the directional pitots at three spanwise stations at each of three horizontal planes, which were the planes of the center-line, the medium, and the high tails. It was shown in reference 1 that a rapid increase in downwash with angle of attack was the cause of a decrease or reversal of the tail contribution to longitudinal stability under certain conditions. A comparison of the data for the different spanwise locations at each vertical position indicates that at high angles of attack there were regions of particularly high downwash at the outer two directional pitots in the two higher tail locations. The large increases of downwash generally occurred earliest at the outer survey station. The slope of the downwash curve for the inboard station was least affected by increase in angle of attack. When sufficiently high angles of attack were attained, the downwash began to decrease with further increase in angle of attack. This effect is evident first near the outer survey station, being delayed to slightly higher angles of attack at the higher positions above the wing chord plane.

At a Reynolds number of 10 million and a Mach number of 0.25, slopes of the downwash curves increased sharply with angle of attack as the angle of attack exceeded 14° . When the Reynolds number was decreased to 2 million, such increases occurred at substantially lower angles of attack. Variation of Mach number from 0.25 to 0.92 had no large consistent effect

upon the angle of attack where these increases in slope occurred or upon the variation of slope of the downwash curves with spanwise or vertical position in the region of the survey.

All of the data for the tail position in the wing chord plane show nonlinearities in the downwash curve near zero angle of attack, such that the slopes of the downwash curves become negative within a small angle-of-attack range. The origin of these nonlinearities has not been completely established, but they appear to be due primarily to the effect of the dynamic-pressure gradient at the edge of the wake from the wing, resulting in erroneous indications of flow angle when measured with a relatively large diameter, spherical-head-type, directional pitot. (See fig. 1(b).) At most of the Mach numbers and a Reynolds number of 2 million, the variation of downwash angle with angle of attack at the outboard station for the medium-height tail position indicated nonlinearities within a small angle-of-attack range (from 9° to 11°) that are also apparently associated with the directional pitot tube entering and subsequently moving out of the wing wake. This explanation, however, does not account for the very high values of ϵ occurring at slightly higher angles of attack. These values appear to originate from strong vorticity concentrated near the wake outboard of the outermost survey tube.

A comparison of the data presented in figures 11 and 12 with data in figures 9 and 10 indicates that the addition of fences to the wing strongly affected the downwash at the locations of the two outer directional pitots. For moderate angles of attack at the outer station and medium-height tail position, adding fences eliminated the high downwash and produced negative variations of downwash with angle of attack. At higher angles of attack (above about 13°) the downwash was substantially decreased at both of the outer survey stations for Mach numbers below 0.90. At a Reynolds number of 10 million, there were only small effects on downwash at the other locations shown. At a Reynolds number of 2 million, the fences had little effect on the downwash curves at the survey plane nearest the plane of symmetry up to relatively high angles of attack. Within some limited ranges of angle of attack, when the strong negative variations of downwash with angle of attack developed at the outermost survey station, the downwash curves for the intermediate survey station (at the medium and high tail positions) had positive slopes that were even greater than those measured for the model without fences. This indicates that the downwash is distributed laterally as if the spanwise loading on the wing decreased abruptly with lateral distance at some station inboard of the fence at $0.44b/2$ and subsequently increased at some station outboard of the fence.

Varying the Mach number from 0.25 to 0.92 did not greatly change the character of the downwash distribution for the model either with or without fences.

Figures 13 and 14 show the vertical distribution of downwash at the three spanwise survey stations behind the model. The effect on this distribution of adding fences to the wing is also shown in the same figures. The greatest effect of the fences was in the localized region near the outer pitot tube in the plane of the medium tail.

Dynamic Pressure in the Wake

The vertical distributions of dynamic pressure loss at a Mach number of 0.25 and a Reynolds number of 10 million are shown at various angles of attack in figure 15 at three spanwise stations, $0.10b/2$, $0.24b/2$, and $0.38b/2$ from the plane of symmetry. A better illustration of the effect of angle of attack upon the wake and upon the location of the wake relative to the tail positions is provided by the type of graphs shown in figures 16 through 18, in which the vertical locations of the contour lines of constant q_t/q are plotted against angle of attack.

At a Reynolds number of 10 million (figs. 15 and 16), losses in the wake near the tail remained small everywhere except at the medium tail location near the plane of symmetry when the angle of attack exceeded 15° . A decrease of Reynolds number to 2 million had only a small effect, such that losses in the wake occurred at slightly lower angles of attack.

The data indicate that the region where large dynamic-pressure losses occurred would be avoided at all of the Mach numbers of the tests and at angles of attack where longitudinal instability occurred, if the tail were located above the wake center in the high position or below the wake center on the fuselage center line. At the medium tail position at angles of attack somewhat larger than those where model instability first occurred, decreases in the local dynamic pressure were measured which resulted in values of q_t/q as low as 0.7, but even at this position the effect of such losses was probably not large, because they occurred within only limited portions of the tail span. The losses were substantially smaller at the outer survey station, but since this station is near the wing mid-semispan, it is probable (judging from general observations of the characteristics of the wake from swept wings) that they would again be large still farther from the plane of symmetry. The wake survey data indicate that at low angles of attack the dynamic pressure was low in the region of the tail located on the fuselage center line, which is in accord with the low values of $\eta(q_t/q)$ shown in reference 1. However, the low values of $\eta(q_t/q)$ which were calculated for the tail in the medium position at low angles of attack cannot be similarly correlated with the measured local dynamic pressure.

The locations of the regions of large dynamic-pressure loss at the two outer survey stations were strongly affected by the addition of fences. The data from tests at a Reynolds number of 2 million indicate

that the large increase in downwash accompanying the initial stalling of the wing without fences deflected the wake downward; whereas with fences on the wing, the center of the wake moved continuously farther away from the wing chord plane with increasing angle of attack. The upward displacement of the wake due to fences means that at high angles of attack the outer portion of the horizontal tail mounted either in the high or medium position would be in a region of lower dynamic pressure than when the fences were off.

Mean Downwash at the Tail

Local measured downwash angles have been used to estimate an average downwash over the complete span of the horizontal tail. This average downwash was determined graphically using the following relation,

$$\epsilon_{av} = \frac{2}{b_t} \int_0^{\frac{b_t}{2}} \epsilon_l \left(\frac{c_l c}{C_L c_{av}} \right)_t dy \quad (1)$$

in which the local downwash angles from the data obtained with the directional pitots at spanwise stations $0.17b/2$, $0.31b/2$, and $0.45b/2$, are weighted according to the spanwise loading on the tail surface as calculated from reference 4. The effect on the spanwise load distribution of the variations of local angle of attack along the tail span was investigated. To take this effect into account, the local lift coefficient c_l in equation (1) was calculated as

$$c_l = c_{l_a} + C_L c_{l_b}$$

where c_{l_a} is the additional loading on the isolated tail and c_{l_b} is the basic loading obtained when it is assumed that the tail is twisted by an amount equal to the lateral variation of downwash. Calculations using this expression for c_l indicated that the effect of the basic-type loading on the average downwash was small except at some of the very high angles of attack. Since these high angles of attack were beyond the angles where model longitudinal instability due to downwash was considered significant, it was concluded that the effect of the basic loading could be neglected, so that the section lift coefficient in equation (1) would be the lift coefficient due to the additional loading. Since the local downwash angles required in equation (1) were not measured in regions corresponding to the portion of the tail near the plane of symmetry, they were obtained by extrapolating the data from the more outboard survey stations. Although such extrapolations may not be accurate, if errors in the extrapolations are similar for the two tail heights, it would be expected that the average downwash could be correlated to some

extent with effective downwash (calculated from force and moment data presented in reference 1). The average downwash was compared with effective downwash to determine whether such a correlation could be made of the variations in slope of the downwash curves with varying angle of attack and tail height.

The downwash obtained by averaging the local downwash measured with the directional pitots is compared in figure 19 with the effective downwash. Good agreement between data from these two sources was not obtained. The main reason for the lack of agreement probably was that the flow-angle data could not be accurately extrapolated to the plane of symmetry, as mentioned above, and that the fuselage apparently introduced significant localized flow angles which could not be evaluated from the directional pitot-tube data. The effect of the wing wake on the local indicated flow angles near the wing wake was discussed earlier and is apparent in this figure as the decreased and reversed variations of downwash with angle of attack near zero angle of attack for the centrally located tail.

Although the data for the model without fences (fig. 19(a)) show generally an increase in slope of the downwash curves with angle of attack, the averaged data do not show some of the particularly large variations in slopes that are evident in data derived from analysis of the measured lift and pitching moments. Apparently the method of obtaining the average values did not take into account adequately the large changes in downwash observed near the outer portion of the tail. If the effect of the lateral variation of downwash on the spanwise loading of the tail had not been neglected (as mentioned earlier) in calculating the average downwash, higher values of average downwash would have been calculated, but calculations (for typical angles of attack and Mach numbers) indicated that such increases would be small, that is, less than 0.2° at about 10° angle of attack.

Reference 1 indicated that the addition of fences decreased the effective downwash at the tail with the result that the tail contribution to stability was maintained up to high angles of attack. The average downwash data (fig. 19(b)) determined from the survey indicate that the fences decreased the slopes of the downwash curves at the center-line tail location, but at the medium tail location the average downwash does not indicate such decreases. Although the local downwash data at spanwise station 0.453b/2 shown in figures 11 and 12 do indicate such decreases, this station was so far outboard that it did not greatly affect the average downwash. It is concluded from figures 19(a) and 19(b) that a considerably more extensive and detailed survey of the downwash field, using more suitable survey apparatus, would be required to correlate the measured downwash angles with the downwash indicated by the model force and moment data.

Tuft Studies

The results of tuft studies of the flow on the model with and without fences are presented as graphic plan-form sketches of the model wing, showing the progress of separation through the angle-of-attack range.

In order to indicate whether the tufts themselves affected the pattern of separation in such a way as to alter the longitudinal stability, pitching-moment data are presented for the model with and without tufts. (See figs. 20 through 29.) At a Reynolds number of 10 million and a Mach number of 0.25, addition of tufts had a noticeable effect on the stability, so that the separation patterns probably differed from those on the wing without tufts. At the lower Reynolds number, 2 million, the pitching-moment data for the model with tufts were similar to the data for the model without tufts and the observed patterns of separation should be generally applicable to the model without tufts.

At a Mach number of 0.25 (figs. 20 through 23), the initial separation occurred at the leading edge near the tip. Addition of the fence had little effect on the angle of attack at which separation first occurred, but eliminated or retarded the separation just outboard of the fence. Decreasing the Reynolds number from 10 million to 2 million resulted in the initial separation occurring at a lower angle of attack; however, the general pattern of separation was similar to that at 10 million Reynolds number.

At Mach numbers of 0.85, 0.90, and 0.92 (figs. 24 through 29), separation first occurred a short distance behind the leading edge, probably due to the effect of compression shocks at these positions. Addition of fences produced a region where separation was retarded or eliminated just outboard of the fences as in the case of a Mach number of 0.25. The substantial increases in lift coefficient where longitudinal instability occurred that were apparent in the force and pitching-moment data at Mach numbers up to 0.85 (fig. 4) can be correlated with this retarded progress of the separation (figs. 20 through 25), indicating that the fences delayed the loss of lift near the tip that was characteristic of the plain wing. At Mach numbers of 0.90 and 0.92 (figs. 26 through 29) the fences had little effect on pitching-moment characteristics up to angles of attack where the stalled region had progressed over most of the wing, even though they still retarded some of the separation. With further increase in angle of attack, however, an abrupt forward movement of the center of pressure occurred for the model with the plain wing and was avoided when fences were added. The tuft data indicate that this improved moment characteristic observed for the model with fences was associated with the region of unseparated flow adjacent to the fences and with the other areas shown in the sketches on the rearward and outboard portions of the wing where separation was delayed up to the highest angles of attack of the test.

Theoretical Calculation of Downwash

Distributed horseshoe vortices.— The downwash behind the wing without fences has been calculated for three vertical positions of the horizontal tail by the method described in reference 5, which provides for calculation of the velocities induced at the tail by horseshoe vortices distributed along the quarter-chord line of the wing. It is assumed in the theory that the induced velocities at any point having known coordinates with reference to the actual vortex sheet would be the same as those calculated at a point having the same coordinates referred to the vortex sheet if the vortex sheet were flat and undistorted. The shape and position of the vortex sheet was calculated by integrating the vertical displacement of the flow between the trailing edge and the quarter chord of the tail using the expression

$$\Delta z_v = \int_{x_{TE}}^x \tan \epsilon_v dx \quad (2)$$

where ϵ_v is the downwash in the vortex sheet.

Typical wing spanwise load distributions which were used in the calculations are shown in figure 30. They were obtained from pressure distributions measured experimentally in tests reported in reference 6 of a full-span model having a wing and fuselage similar to those of the model used in the present tests. The spanwise loading data were obtained on the wing only outboard of $0.2b/2$. The loading curves were extrapolated to the wing-fuselage juncture (as shown by the dotted portions of the curves in figure 30) on the basis of pressure measurements on the fuselage, considering the effects of wing-body interference. The part of the loading curve over the wing enclosed by the fuselage is not shown, but an extrapolation of the illustrated curves to the body center line was made using (unpublished) pressure distributions obtained experimentally at the plane of symmetry in the tests reported in reference 6. This extrapolation gave slightly higher values of loading on the fuselage than would be predicted from theory. The spanwise distributions of downwash calculated by the method of reference 5 for three positions of the tail are shown for several angles of attack in figure 31. The distributions measured with the directional pitots at a Reynolds number of 2 million are also shown (dashed curves) in this figure for comparison. It is evident that the experimental distributions differed considerably from the theoretical. The high values of downwash measured at the outer positions at high angles of attack were not predicted by the theory. A comparison of the levels of the data for the various tail positions indicates that the theory does not predict the large increases in downwash with increased tail height that appear in the effective downwash data. The vertical and lateral distributions of the measured downwash suggest that there existed in the

vortex sheet behind the wing a strong concentration of vorticity near the wing mid-semispan and near the plane of the medium tail.

Another comparison that illustrates the source of some of the differences between the predicted and measured downwash characteristics can be made by comparing the calculated position of the vortex sheet with its position as indicated by the wake survey data. If it is assumed that the downwash causes a vertical displacement of the wake leaving the rear portion of the wing equal to the displacement of the potential flow leaving the wing trailing edge, then the vertical position of the vortex sheet corresponds to the center of the wake. The predicted vortex-sheet locations and the wake-center positions at the three wake survey stations are shown as functions of angle of attack in figure 32. A downward displacement of the wake at the outer stations as the angle of attack increased indicates high downwash in the wake in regions generally in agreement with those indicated by the flow-angle surveys (fig. 10). The effect of the high downwash in these regions is to produce a considerable difference between predicted and observed locations of the vortex sheet under some conditions. When such differences exist, it cannot be expected that the magnitude and distribution of downwash would be predicted with any accuracy.

Single swept vortex. - The observed positions of the vortex sheet and the measured lateral distribution of the downwash behind the wing illustrate some of the important characteristics of the downwash field. Some simple vortex systems that will induce distributions of downwash with similar characteristics have been examined to see if an approximate procedure for predicting downwash might be applicable. In one such procedure, it is assumed that the spanwise loading on the wing can be replaced by a rectangular loading distributed over a reduced span and that the resulting flow can be represented by the flow due to a simple swept horseshoe vortex. This flow would have some of the characteristics of the flow observed in the experimental survey: a large variation of downwash with lateral and vertical positions, and large values of downwash in regions above the wing chord plane relatively far from the plane of symmetry. It is evident that the accuracy of this type of calculation depends on the accuracy of representing the actual flow behind the wing by a flow due to a rectangular loading on the wing. A consideration of the factors (discussed in ref. 7) that determine the downstream distance where the vortex sheet is essentially rolled up indicates that the flow behind a high-aspect-ratio wing at low angles of attack cannot be well represented by such a flow. However, with increasing angle of attack, as the wing stalls and loses lift at the tips, the span load curve of a plane swept wing changes in such a way that it has some of the characteristics of the loading on a lower aspect ratio wing for which the rolling up of the vortex sheet takes place considerably nearer the wing. The changes in load distribution for the moderately high-aspect-ratio swept-wing model used in the tests reported herein were examined and downwash calculations were made based on the replacement of the measured loadings (from ref. 6) with simple rectangular loadings.

The span of the bound vortex was assumed to be the same as the distance between the trailing vortices formed by the complete rolling-up of the vortex sheet. As indicated in reference 7, this distance, which is designated as $2y_0$, can be computed for a wing alone by the relation

$$2y_0 = \frac{C_L S_w}{(c_l c)_{y=0}} \quad (3)$$

where $(c_l c)_{y=0}$ is the loading parameter at the plane of symmetry. Whether this relation is directly applicable to the loading on a wing-fuselage combination is doubtful, even if an accurate experimentally determined loading at the plane of symmetry were available. It was thought that a more realistic indication of the spacing of the rolled-up vortex would be provided by considering the circulation at the plane of symmetry in equation (3) to be equal to the value at the wing-fuselage juncture. Typical values of the loading parameters used in the calculations are shown in figure 30 as the inner extremity of the loading curve (at 0.09 semispan). On the basis of observations of the vertical displacement of rolled-up vortices behind some low-aspect-ratio wings, such as those reported in reference 7, it was assumed that the trailing vortices were parallel to the free-stream flow, that is, that they were undisplaced vertically and laterally after leaving the wing. Another simplification that is believed to be consistent with the accuracy of the method was the assumption that the bound vortex lay in the plane of the trailing vortices, rather than in the plane of the wing inclined at the angle of attack. The orientation of the vortex system with reference to the model components is illustrated in figure 33, where the vortex is assumed to lie along the line ABO'CD and the location of the chord plane of the wing is determined by the points BOC which are on the quarter-chord line of the wing. It was first assumed that the trailing vortices left the wing at the trailing edges. Preliminary calculations indicated that with this assumption the predicted regions of high downwash were closer to the chord plane than was indicated by experiment. Better agreement resulted when it was assumed that the flow breaks away from the wing surface ahead of the trailing edge and extends downstream from this more forward position. In the calculations, this location was assumed to be 25-percent chord (at the spanwise station y_0). The downwash corresponding to the vortex system derived on the basis of the considerations discussed above has been calculated. The calculations were made by a graphical procedure which was equivalent to solving equation (34) of reference 7.

The lateral variation of downwash predicted by the calculations for three Mach numbers, 0.6, 0.8, and 0.9, are compared with experimental results in figure 34. The calculations provide better predictions of the lateral variation of downwash than those obtained from the theory of reference 5, but still failed to predict the extremely high downwash at the outboard survey positions and the large increase in downwash with increased tail height (from the center to the medium position).

A limited study has indicated that calculations based on certain other assumed vortex patterns representing the flow due to the wing would afford better correlation of calculated and measured downwash than the two methods described in this report. It is probable that some empirical rules for calculating downwash when the wing is partially stalled might be determined as a result of tests in which local flow angles are measured behind the wing. However, it was concluded that such rules could not be specified except after a considerably more detailed survey of the flow field than was conducted in the tests reported herein.

CONCLUDING REMARKS

Measurements of downwash in the region of the horizontal tail of a model with a wing swept back 45° indicated that at high angles of attack there were regions of particularly high downwash at the outer portion of the tail (31 and 45 percent wing semispan) at the two higher tail locations (12.7 and 25.5 percent wing semispan above the wing chord plane). Addition of fences to the wing at 44 and 69 percent semispan considerably reduced these high values of downwash at the outermost portion of the tail.

Downwash data obtained from directional pitots were used to estimate the average effective downwash on the complete tail. These average values did not agree well with the effective values indicated by the force and moment data and it was concluded that the survey of the downwash field was not sufficiently complete to show the large observed effects of angle of attack and tail height on the longitudinal stability.

Theory based on calculating the flow induced by horseshoe vortices distributed along the wing quarter-chord line failed to predict accurately the effect of tail height on the variation of downwash angle with angle of attack and also did not predict either the observed lateral and vertical distributions of downwash at the tail locations, or the effective downwash at high angles of attack. An approximate procedure for estimating downwash at the tail based on calculating the flow induced by a single swept vortex did not indicate the large decreases in the tail contribution at high angles of attack that were indicated in the tests of the model, but afforded a slightly better prediction of the lateral and vertical distributions of downwash.

Ames Aeronautical Laboratory
National Advisory Committee for Aeronautics
Moffett Field, Calif., Apr. 27, 1955

REFERENCES

1. Stephenson, Jack D., Bandettini, Angelo, and Selan, Ralph: Longitudinal Stability Characteristics at Mach Numbers Up to 0.92 of a Wing-Body-Tail Combination Having a Wing With 45° of Sweepback and a Tail in Various Vertical Positions. NACA RM A54K09, 1955.
2. Herriot, John G.: Blockage Corrections for Three-Dimensional-Flow Closed-Throat Wind Tunnels, With Consideration of the Effect of Compressibility. NACA Rep. 995, 1950.
3. Sivells, James C., and Salmi, Rachel M.: Jet-Boundary Corrections for Complete and Semispan Swept Wings in Closed Circular Wind Tunnels. NACA TN 2454, 1951.
4. DeYoung, John, and Harper, Charles W.: Theoretical Symmetric Span Loading at Subsonic Speeds for Wings Having Arbitrary Plan Form. NACA Rep. 921, 1948.
5. Diederich, Franklin W.: Charts and Tables for Use in Calculations of Downwash of Wings of Arbitrary Plan Form. NACA TN 2353, 1951.
6. Walker, Harold J., and Maillard, William C.: A Correlation of Airfoil Section Data With the Aerodynamic Loads Measured on a 45° Sweptback Wing Model at Subsonic Mach Numbers. NACA RM A55C08, 1955.
7. Spreiter, John R., and Sacks, Alvin H.: The Rolling Up of the Trailing Vortex Sheet and its Effect on the Downwash Behind Wings. Jour. Aero. Sci., vol. 18, no. 1, Jan. 1951, pp. 21-32, 72.

TABLE I.- GEOMETRY OF THE MODEL

Wing		
Aspect ratio	5.5	
Taper ratio	0.532	
Sweep of quarter-chord line, deg	45	
Section normal to quarter-chord line	NACA 64A010	
Area (semispan) sq ft	3.812	
Semispan, ft	3.242	
Mean aerodynamic chord, ft	1.215	
Dihedral	0	
Incidence	0	
Position on body	on axis	
Wing fences		
Distance ahead of wing leading edge	0.05c	
Spanwise locations		
Inboard	0.44b/2	
Outboard	0.69b/2	
Body		
Fineness ratio	12.5	
Length, ft	7.292	
Frontal area/wing area	0.035	
Horizontal tail		
Aspect ratio	4.0	
Taper ratio	0.5	
Sweep, deg (50-percent chord)	0	
Section	63A004	
Area (semispan) sq ft	0.945	
Semispan, ft	1.375	
Tail length (l_t)	2.0c	
Location (vertical distance above wing chord plane extended)		
High tail	0.255b/2	
Medium tail	0.127b/2	
Center tail	0	
Low tail	-0.127b/2	
Survey rake		
Directional pitots		
Spanwise locations	0.170b/2, 0.312b/2, 0.453b/2	
Longitudinal distance to 1/4 point of wing M.A.C.	1.84c	
Vertical locations	0, 0.127b/2, 0.255b/2	
Total pressure tubes		
Spanwise locations	0.100b/2, 0.241b/2, 0.382b/2	
Longitudinal distance to 1/4 point of wing M.A.C.	2.15c	

TABLE II.- CORRECTIONS TO DATA

(a) Constriction due to tunnel walls

Corrected Mach number	Uncorrected Mach number	$\frac{q_{\text{corrected}}}{q_{\text{uncorrected}}}$
0.25	0.250	1.001
.60	.599	1.002
.80	.797	1.004
.85	.846	1.005
.90	.893	1.008
.92	.911	1.010

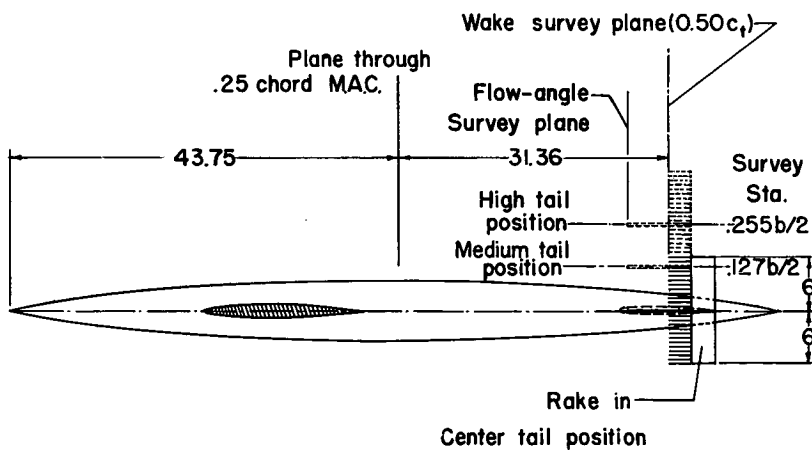
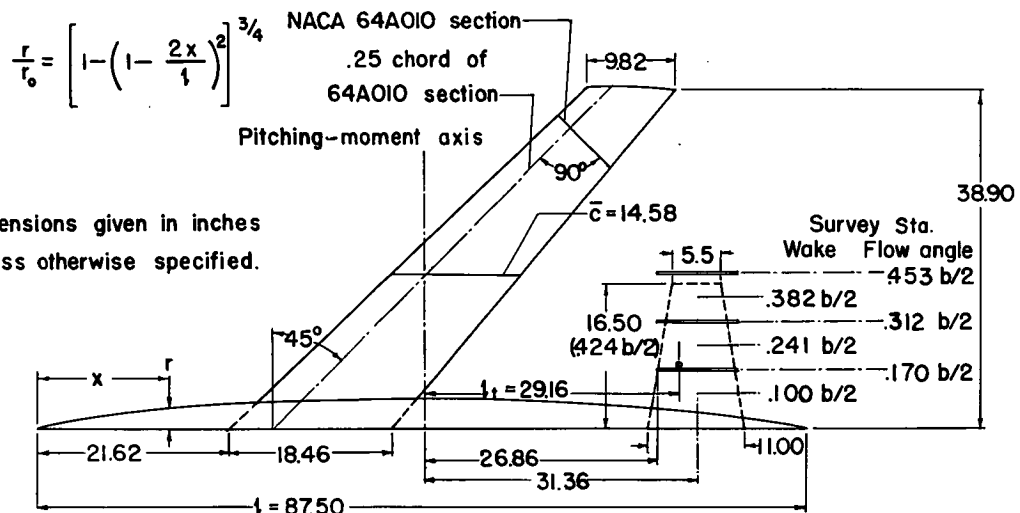
(b) Jet-boundary effects

M	$K_1 = \frac{\Delta \alpha}{C_L}$	$K_2 = \frac{\Delta C_m}{C_L}$	$K_3 = \frac{\Delta C_m}{C_L}$	$K_4 = \frac{\Delta \epsilon_t}{C_L}$
0.25	0.349	-0.0011	0.0038	0.147
.60	.349	-.0010	.0052	.161
.80	.349	-.0008	.0080	.192
.85	.349	-.0006	.0095	.205
.90	.349	-.0001	.0114	.223
.92	.360	.0001	.0123	.231

(c) Tare corrections

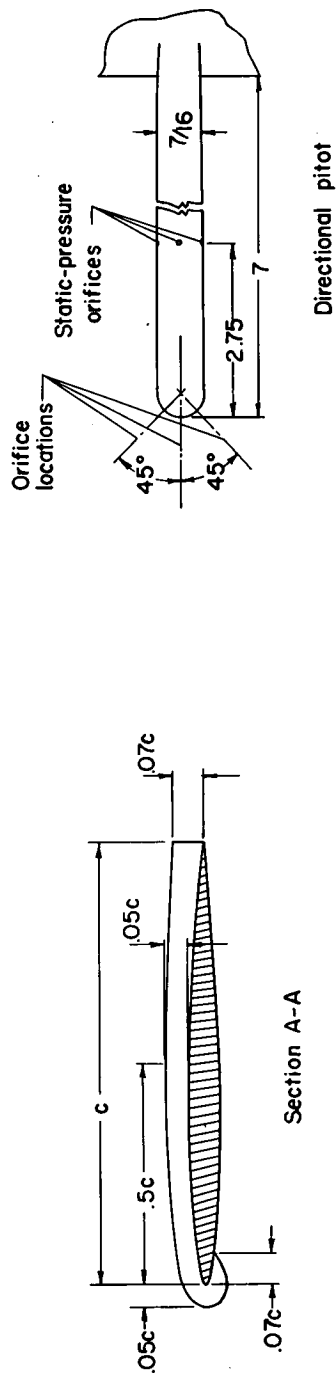
Reynolds number	Mach number	C_D _{Tare}
10,000,000	0.25	0.0049
2,000,000	.25	.0050
2,000,000	.60	.0051
2,000,000	.80	.0057
2,000,000	.85	.0060
2,000,000	.90	.0064
2,000,000	.92	.0067

Equation of body ordinates

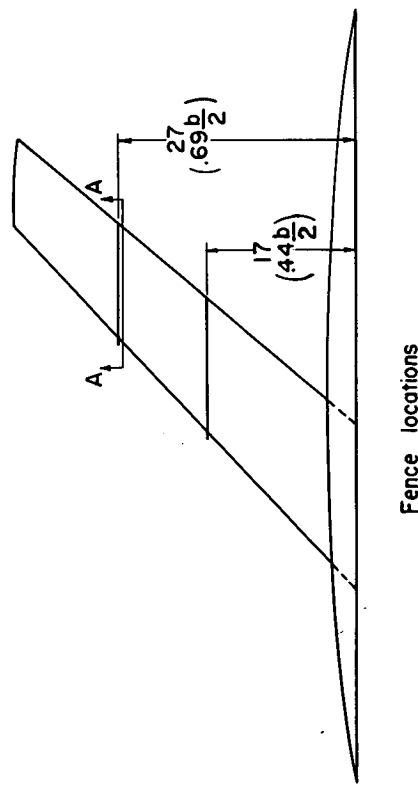


(a) Complete model showing tail and rake locations.

Figure 1.- Drawings of the model.

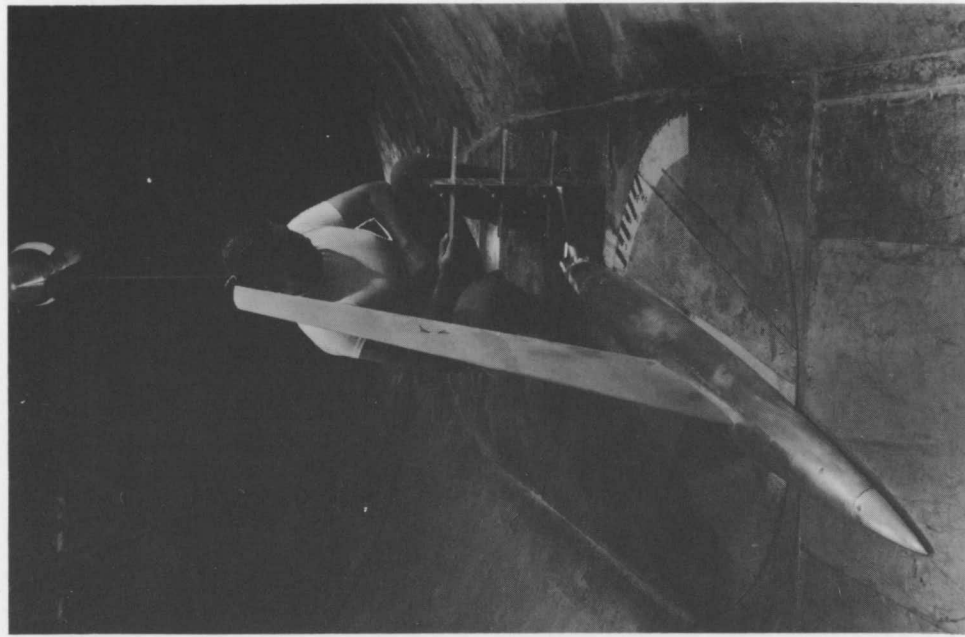


Note: All dimensions are
in inches.



(b) Fence and directional pitot details.

Figure 1.- Concluded.



A-19368

(a) Rake at center tail position.

A-19374

(b) Model with plain wing and rake at high tail position.

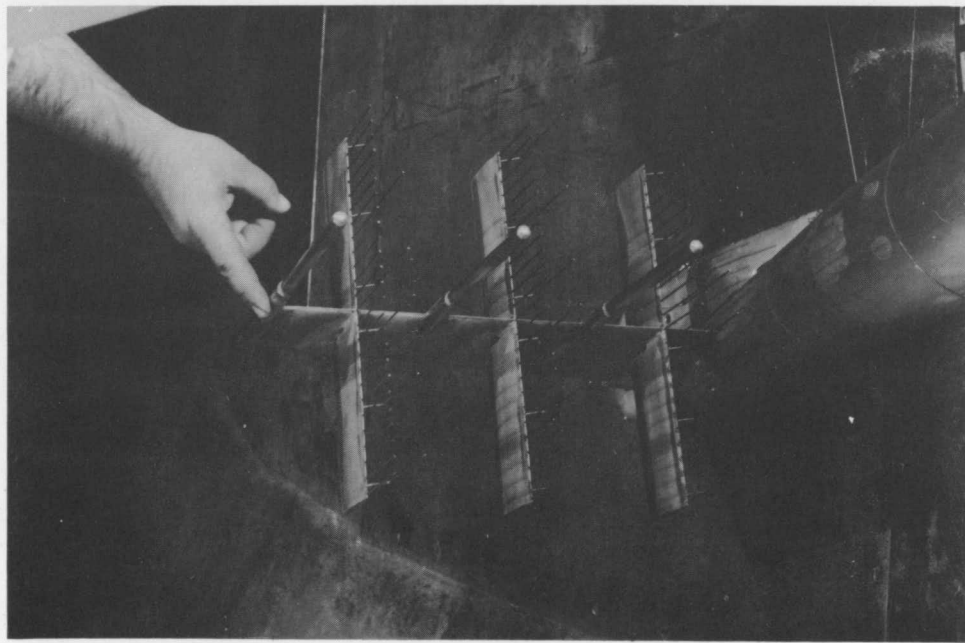


Figure 2.- Photographs of the model.

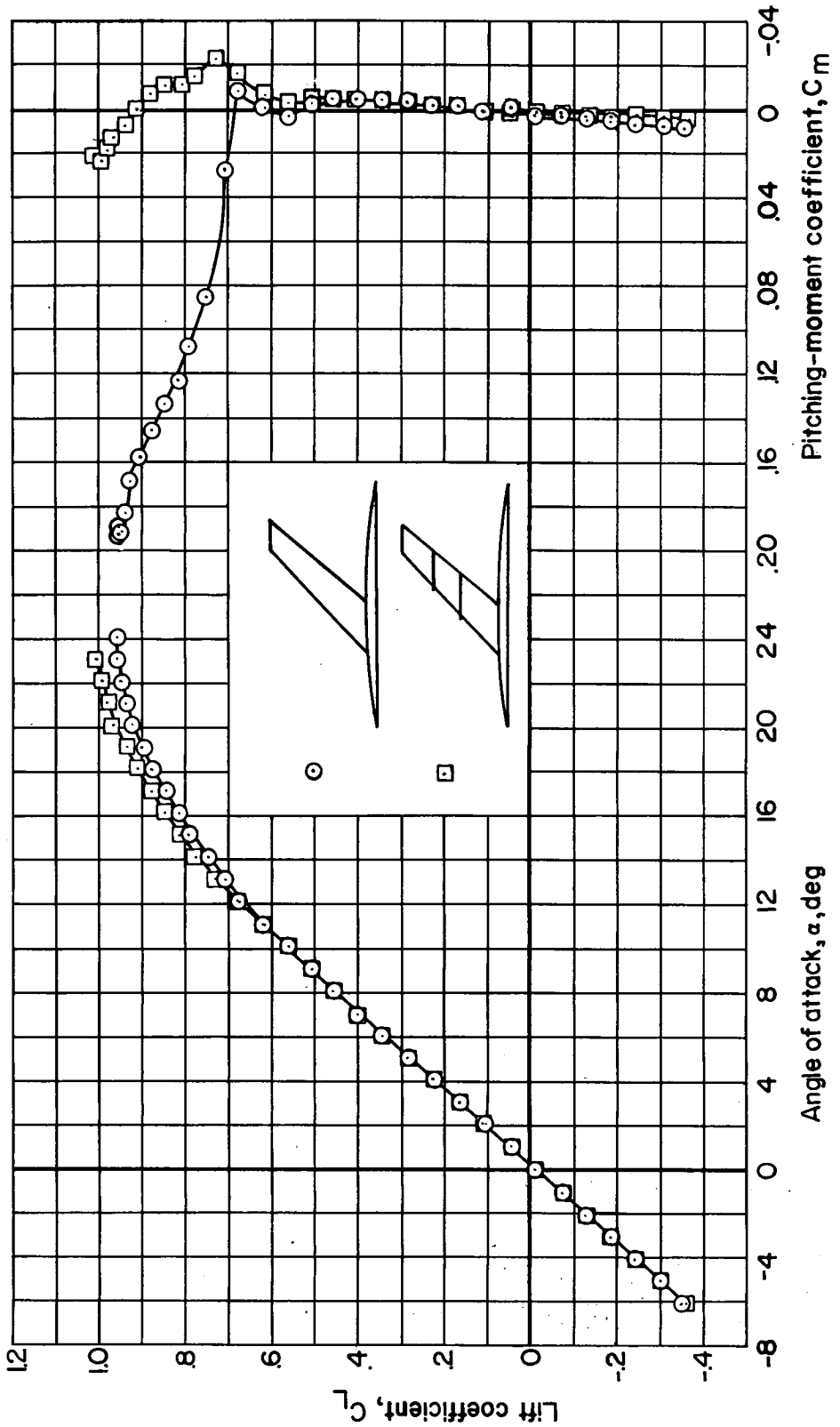


Figure 3. - Aerodynamic characteristics of the wing-body configuration with and without fences;
 $M=0.25$; $R=10,000,000$.

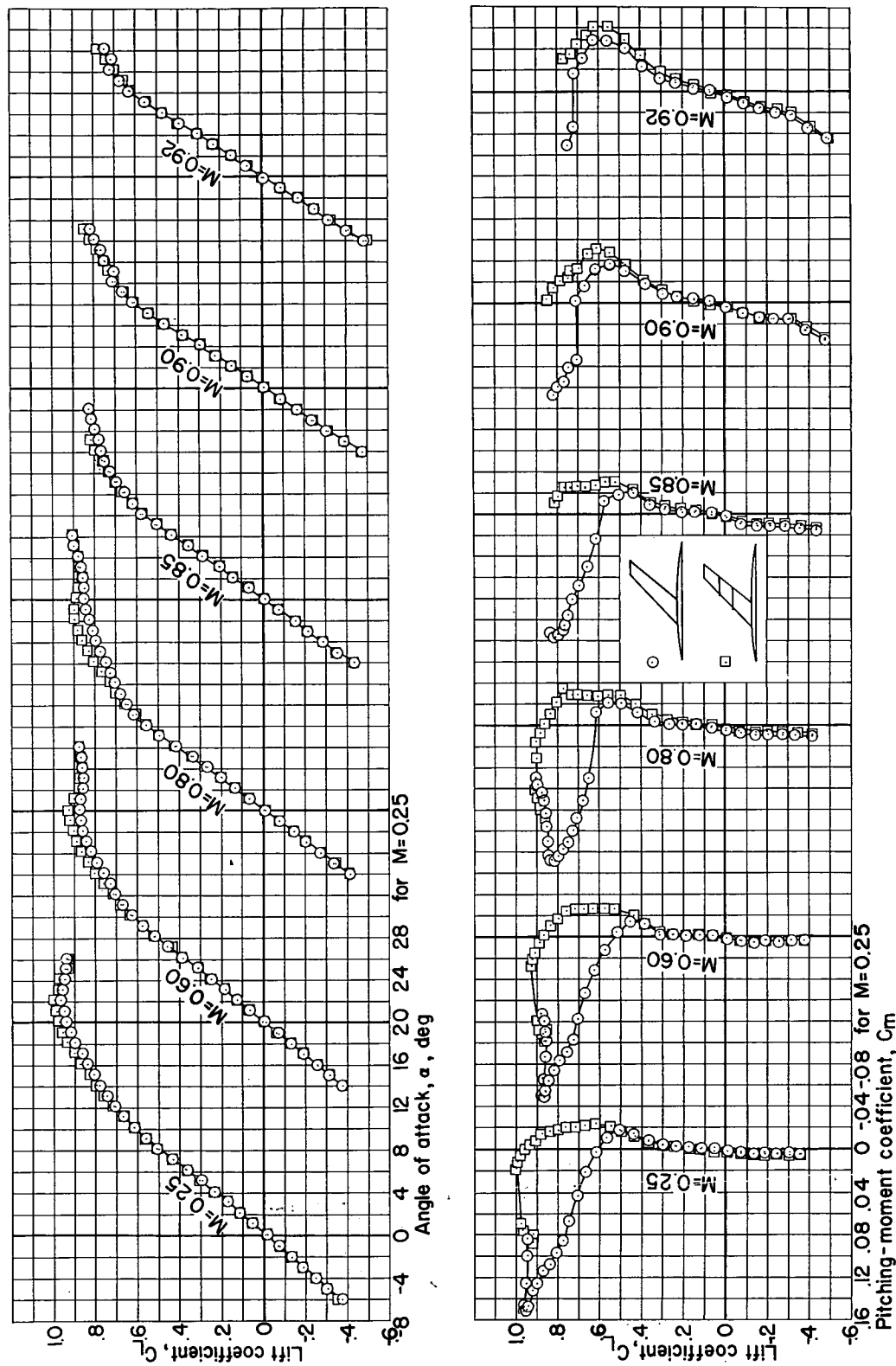


Figure 4.- Aerodynamic characteristics of the wing-body configuration with and without fences, for a series of Mach numbers; $R=2,000,000$.

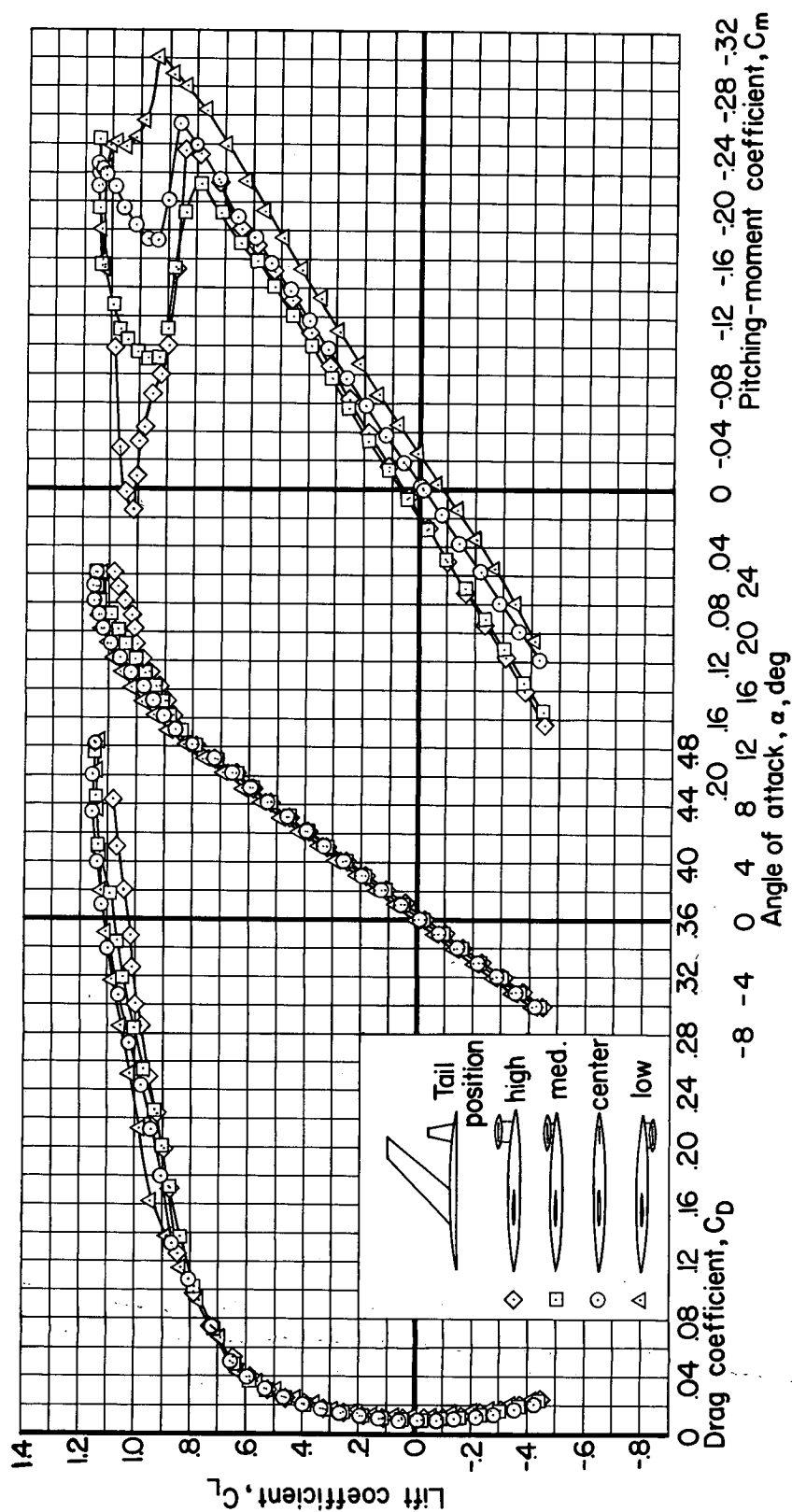


Figure 5.- The effect of tail height on the aerodynamic characteristics of the model at a Reynolds number of 10,000,000. Plain wing; $M=0.25$.

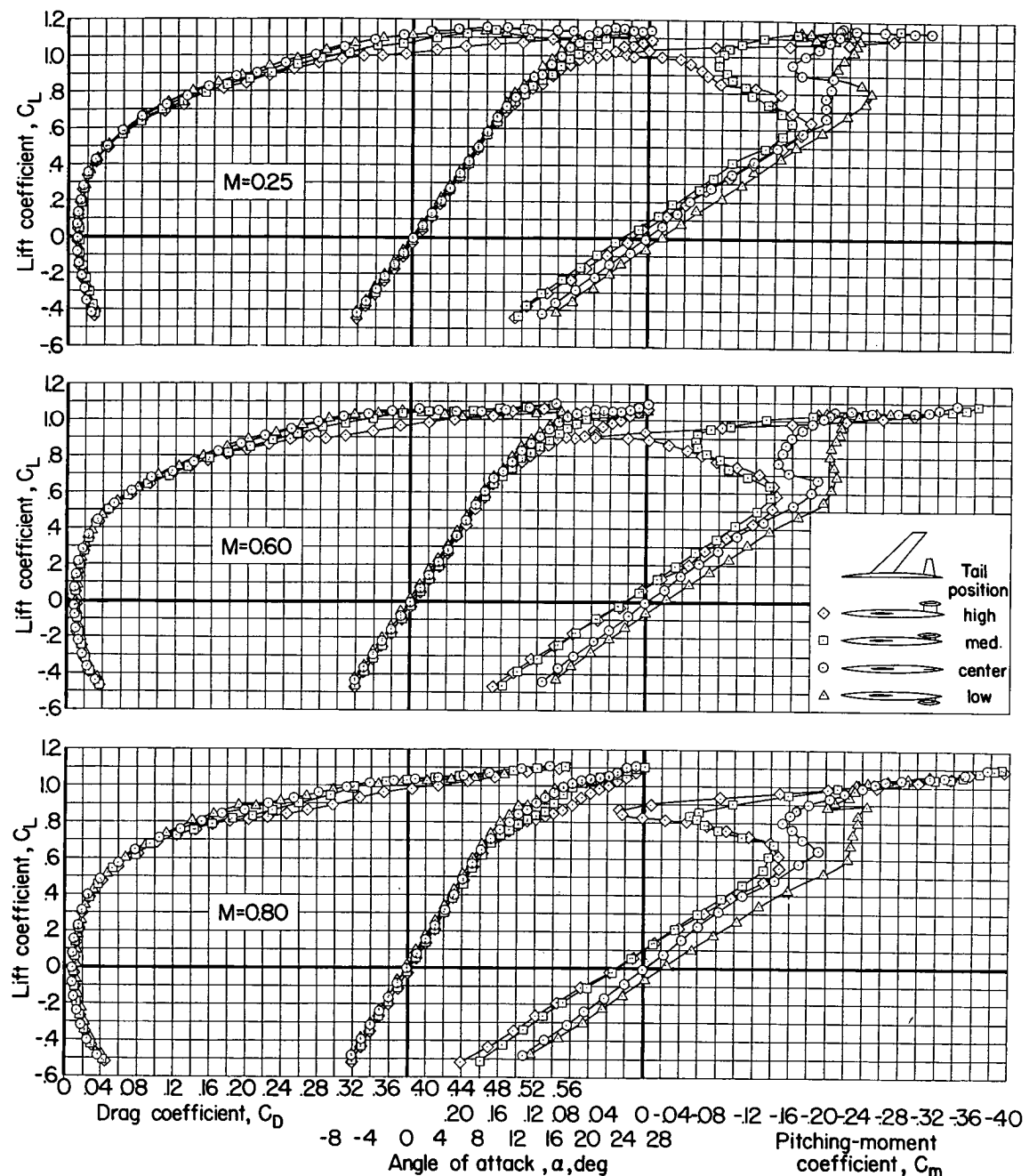
(a) $M=0.25$, 0.60 , and 0.80

Figure 6.- The effect of tail height on the aerodynamic characteristics of the model at various Mach numbers. Plain wing; $R=2,000,000$.

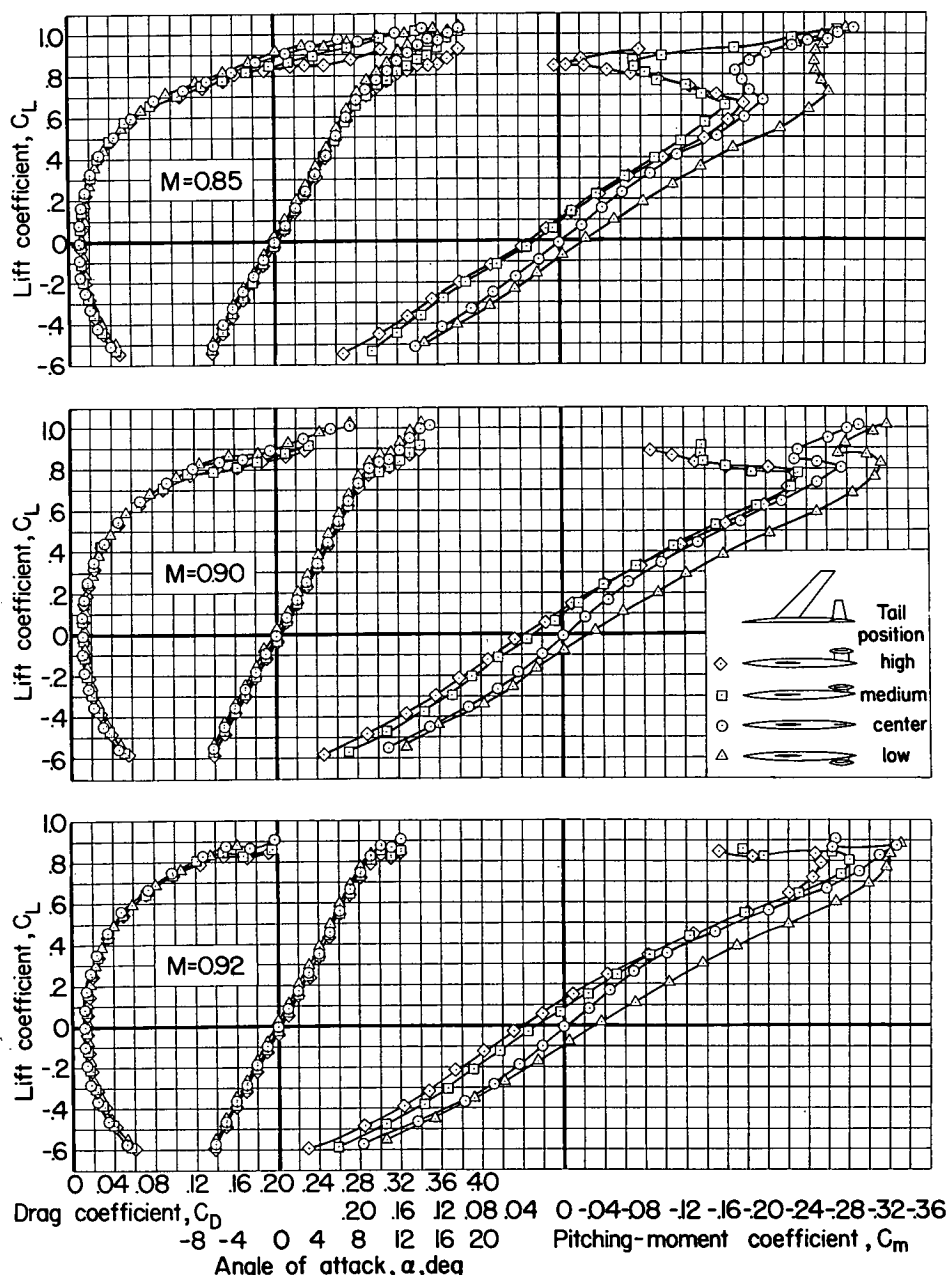
(b) $M=0.85, 0.90$, and 0.92

Figure 6.- Concluded.

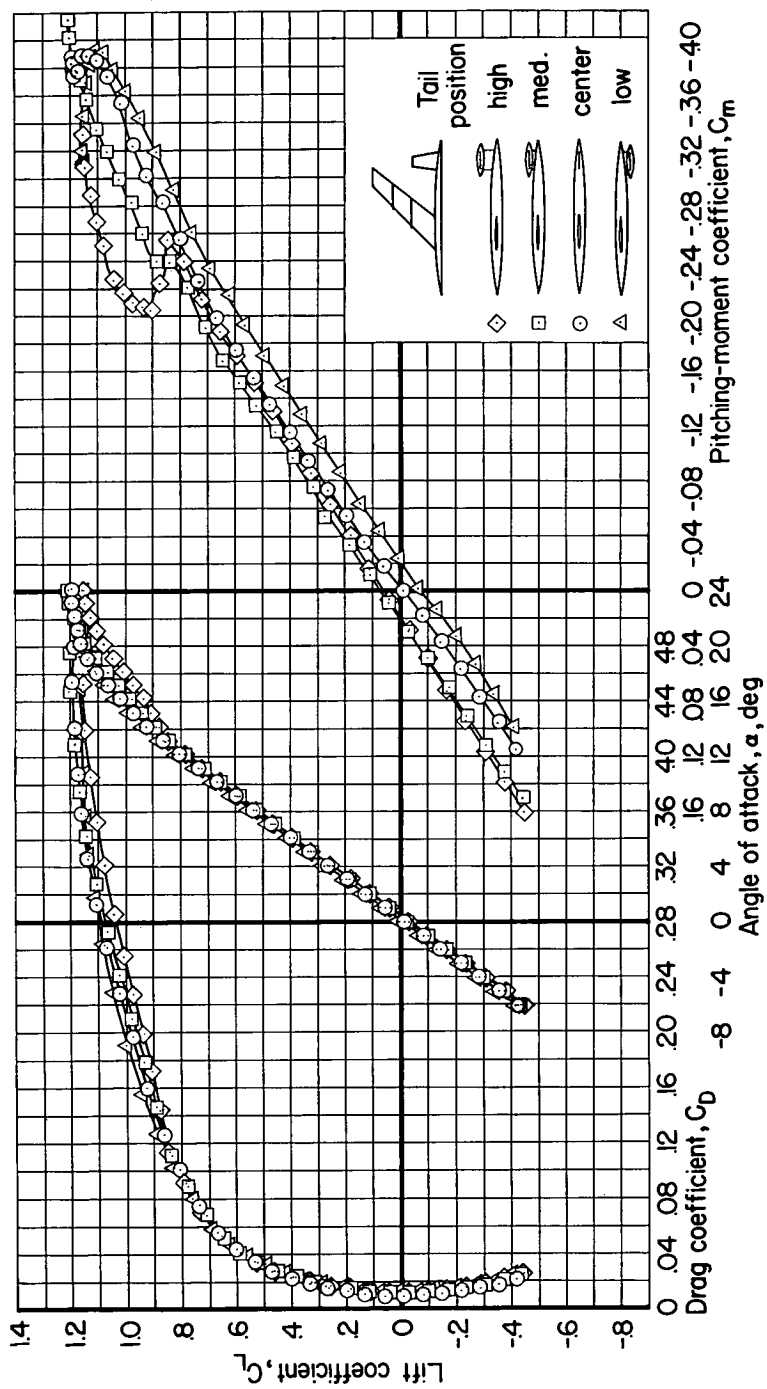


Figure 7.- The effect of tail height on the aerodynamic characteristics of the model at a Reynolds number of 10,000,000. Wing with fences; $M=0.25$.

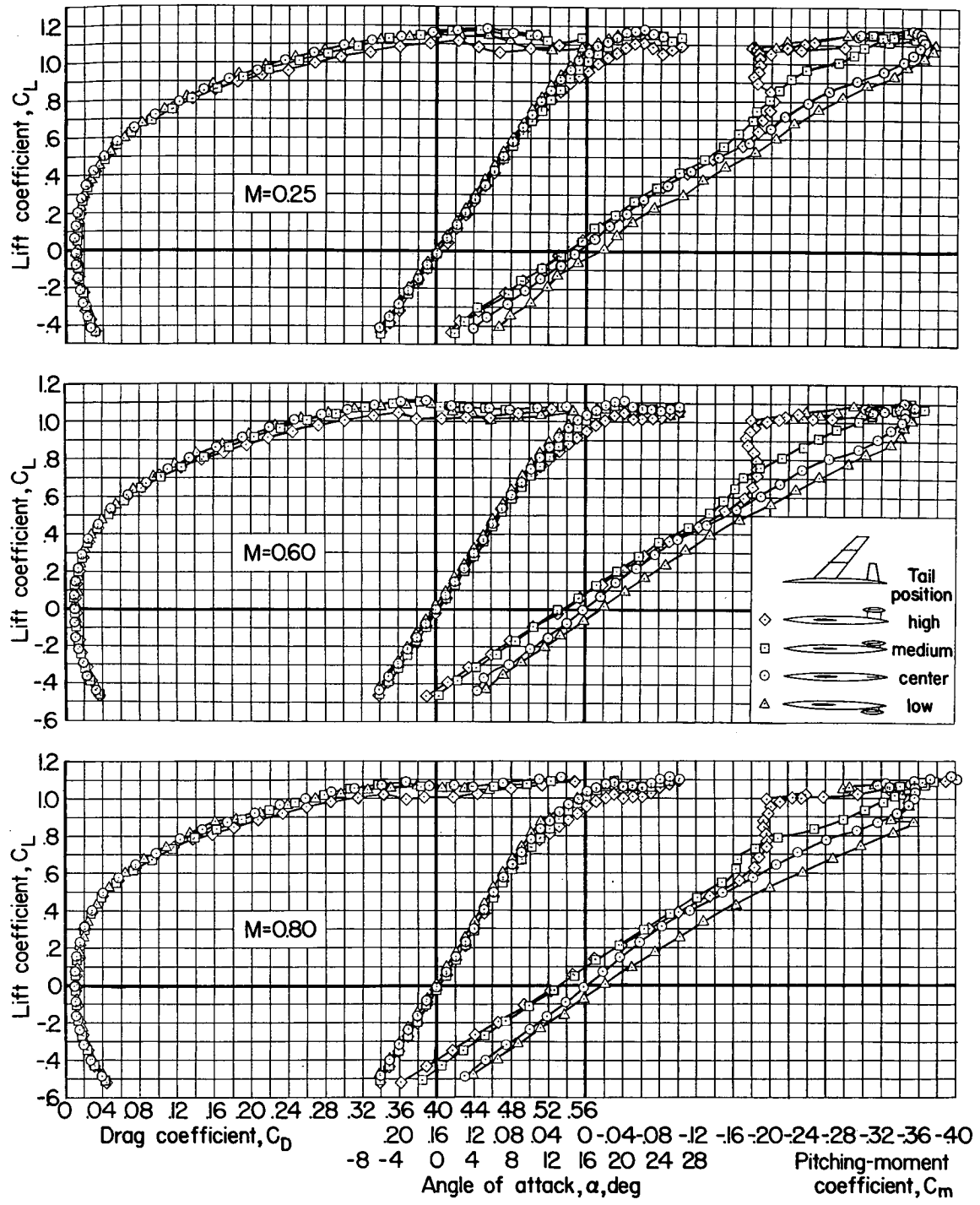
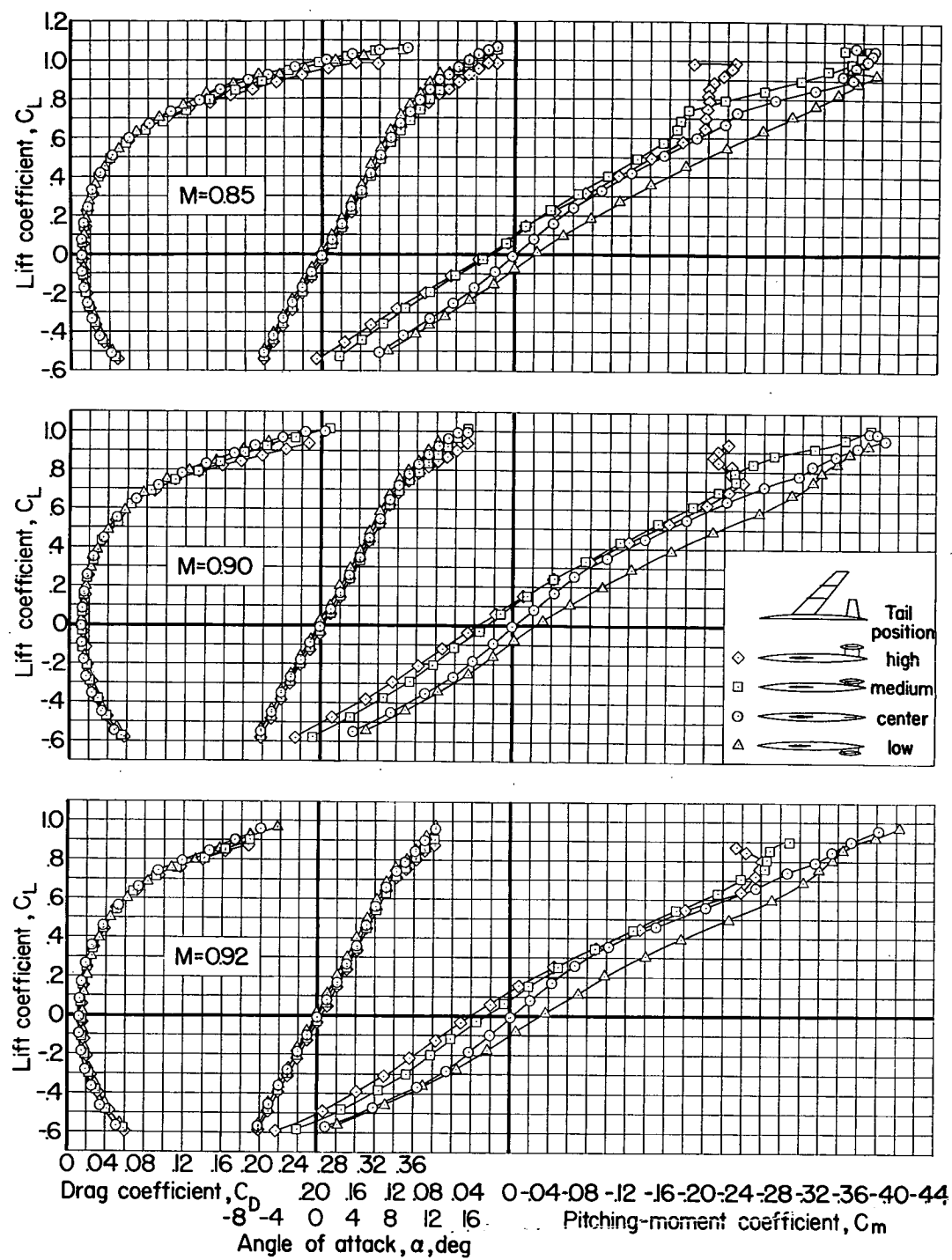


Figure 8.- The effect of tail height on the aerodynamic characteristics of the model at various Mach numbers. Wing with fences; $R=2,000,000$.



(b) $M=0.85, 0.90$, and 0.92

Figure 8.- Concluded.

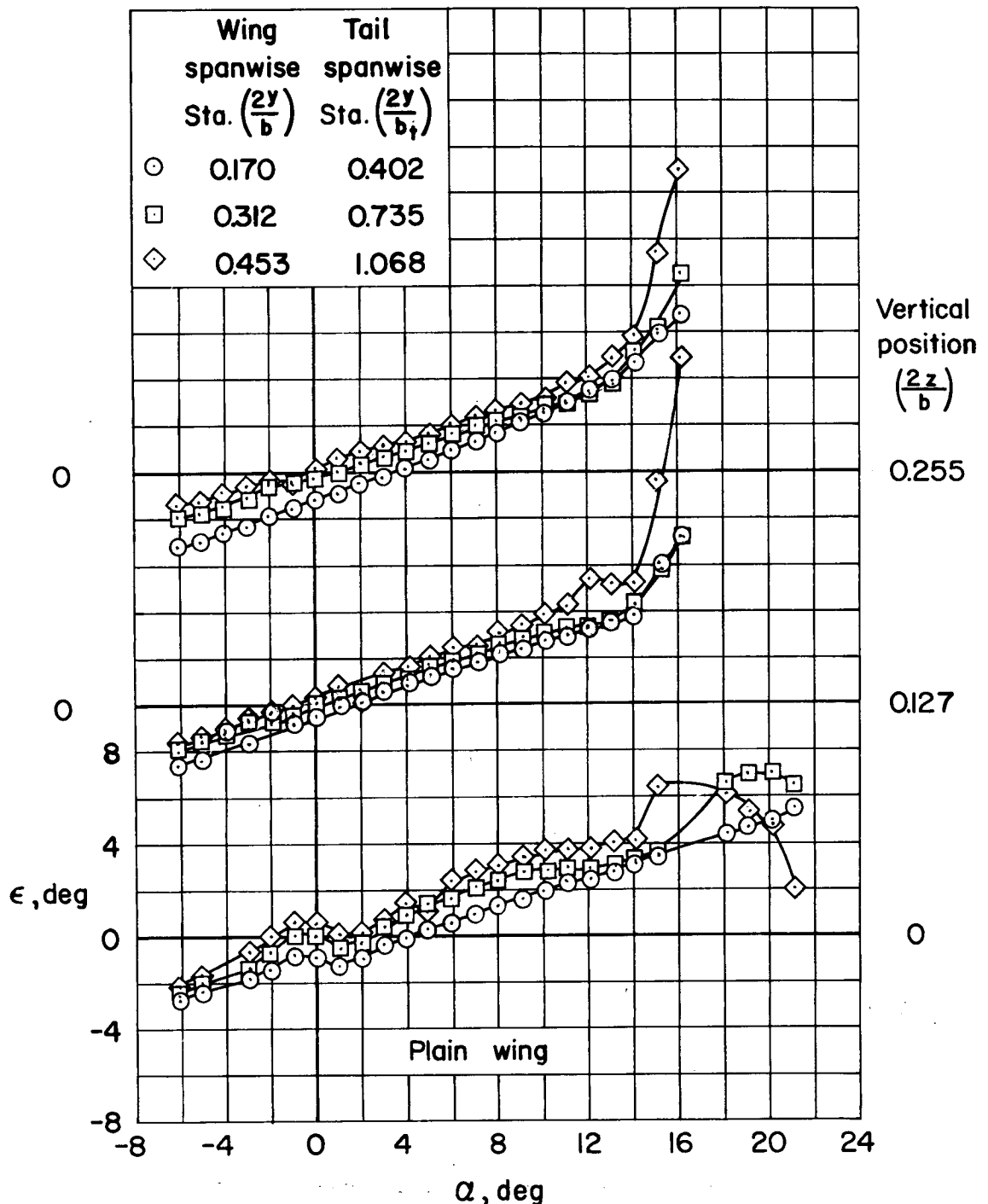


Figure 9.- The variation of local downwash with angle of attack at various points along the horizontal tail span and for three vertical locations. Plain wing; $M=0.25$; $R=10,000,000$.

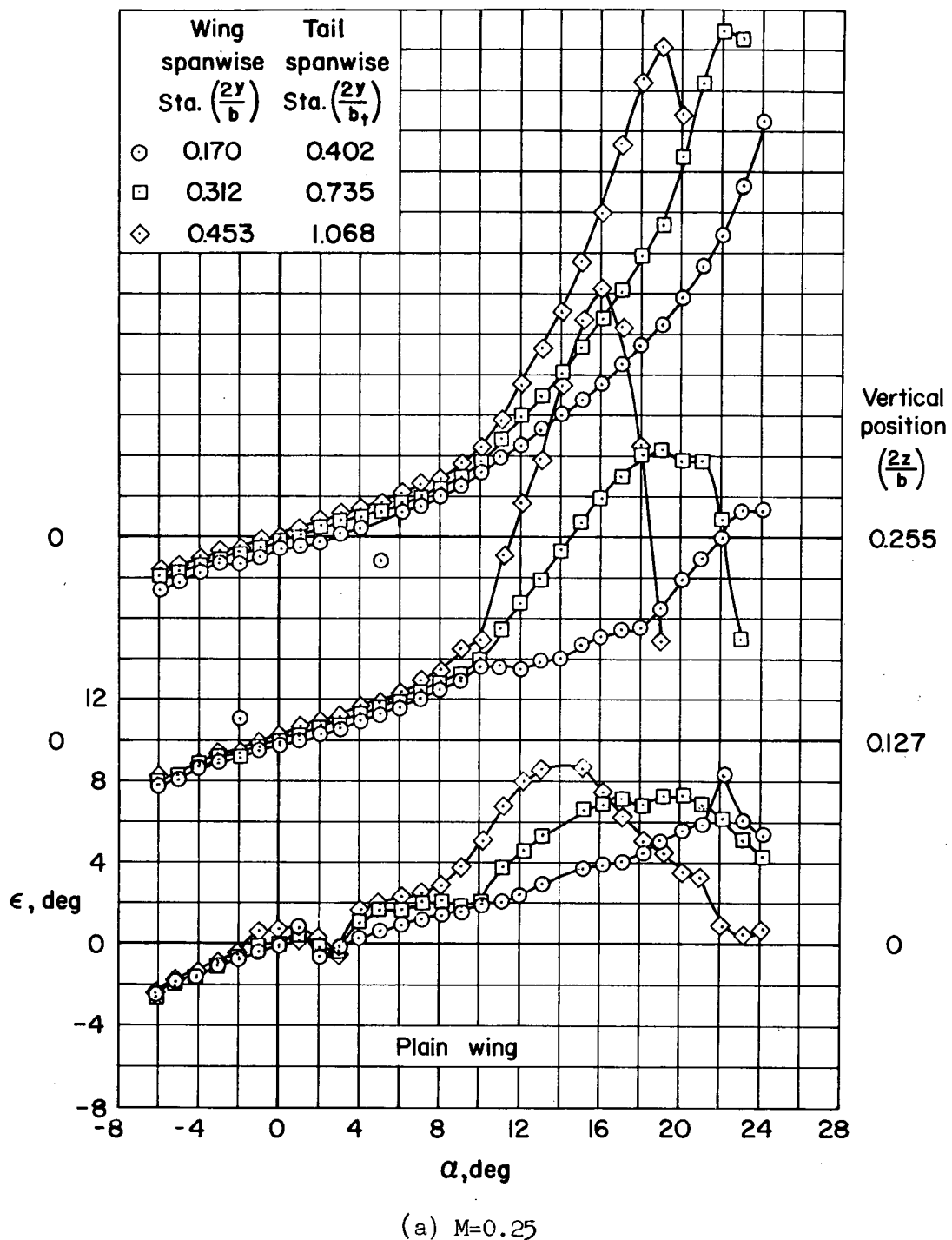


Figure 10.- The variation of local downwash with angle of attack at various points along the horizontal tail span and for three vertical locations. Plain wing; $R=2,000,000$.

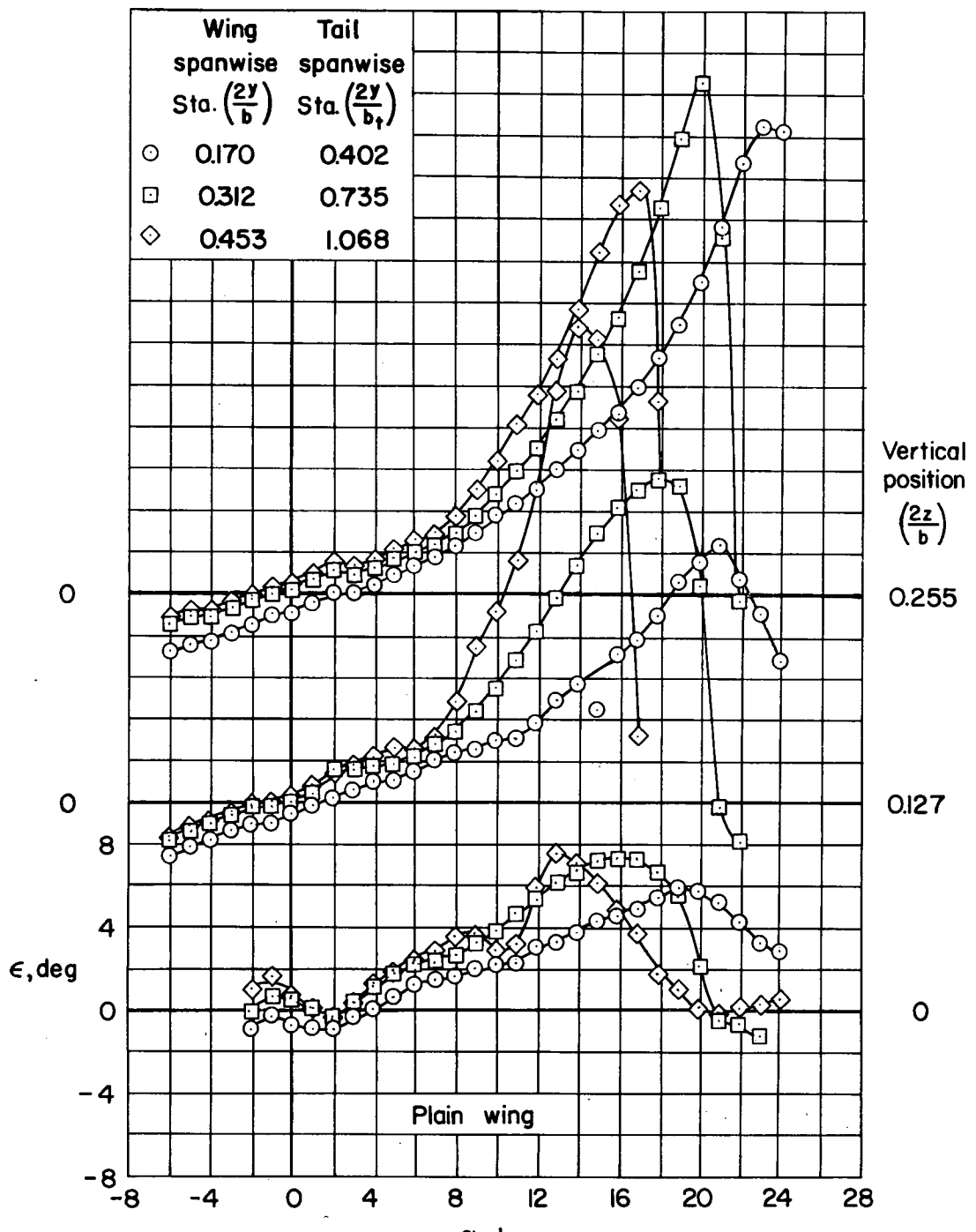
(b) $M=0.60$

Figure 10.- Continued.

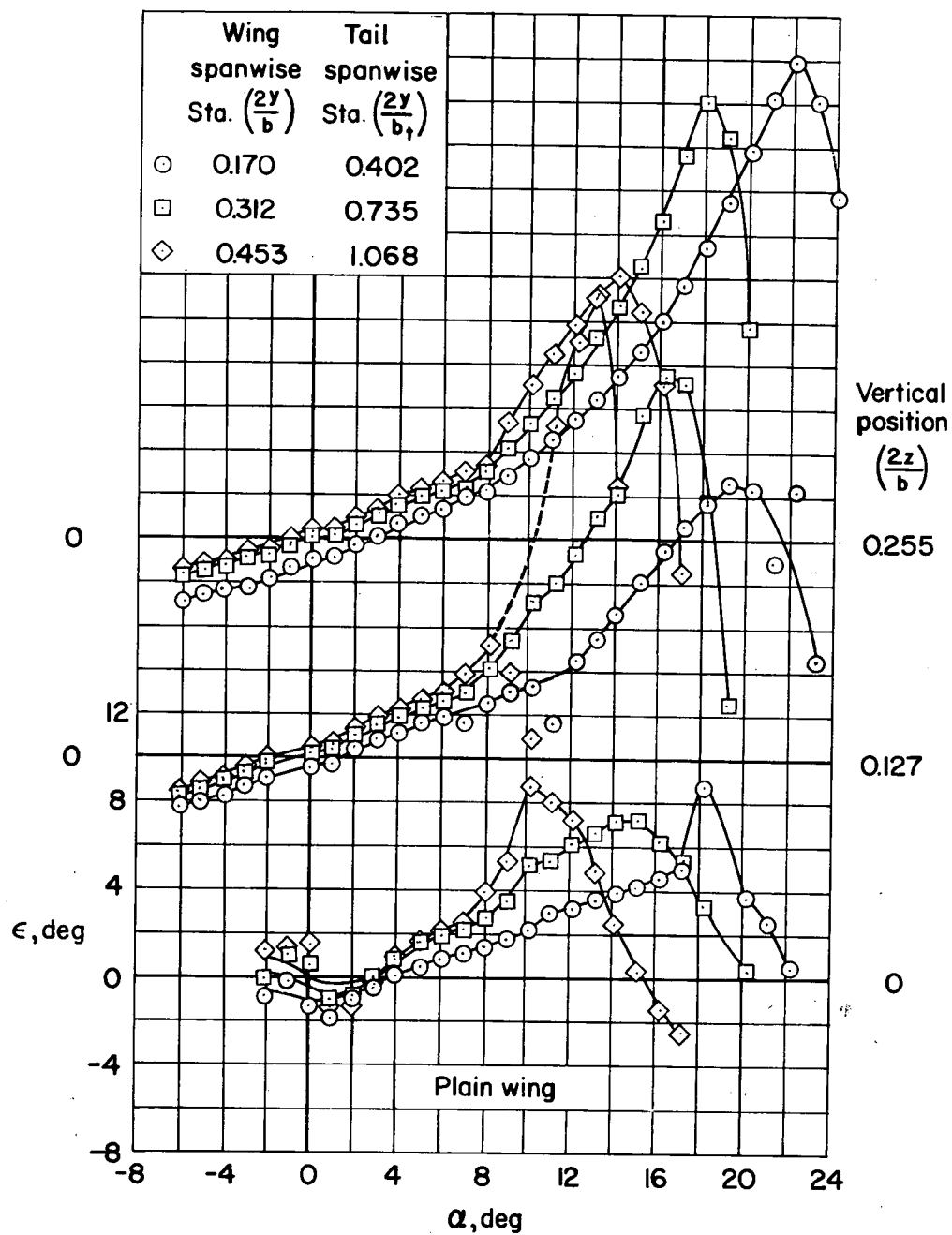
(c) $M=0.80$

Figure 10.- Continued.

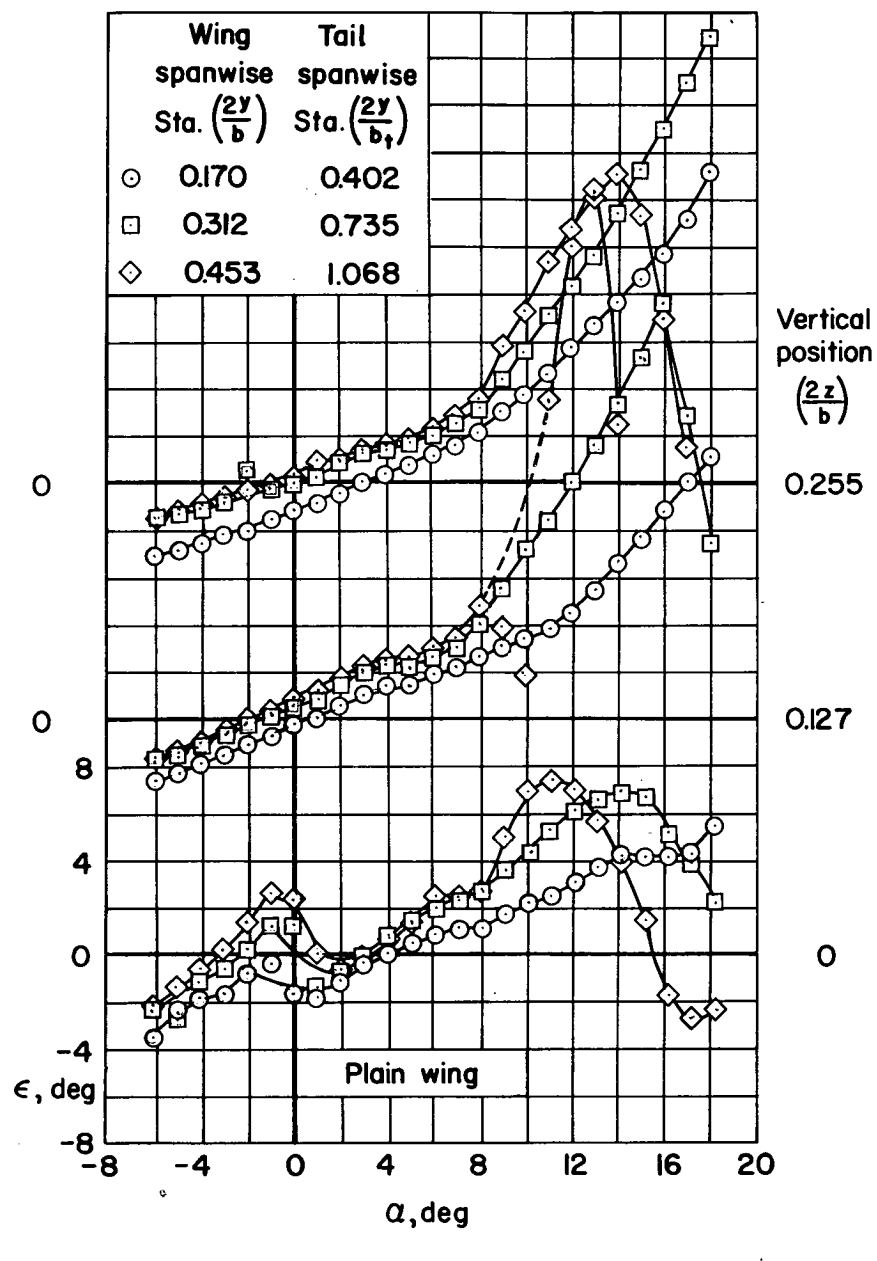


Figure 10.- Continued.

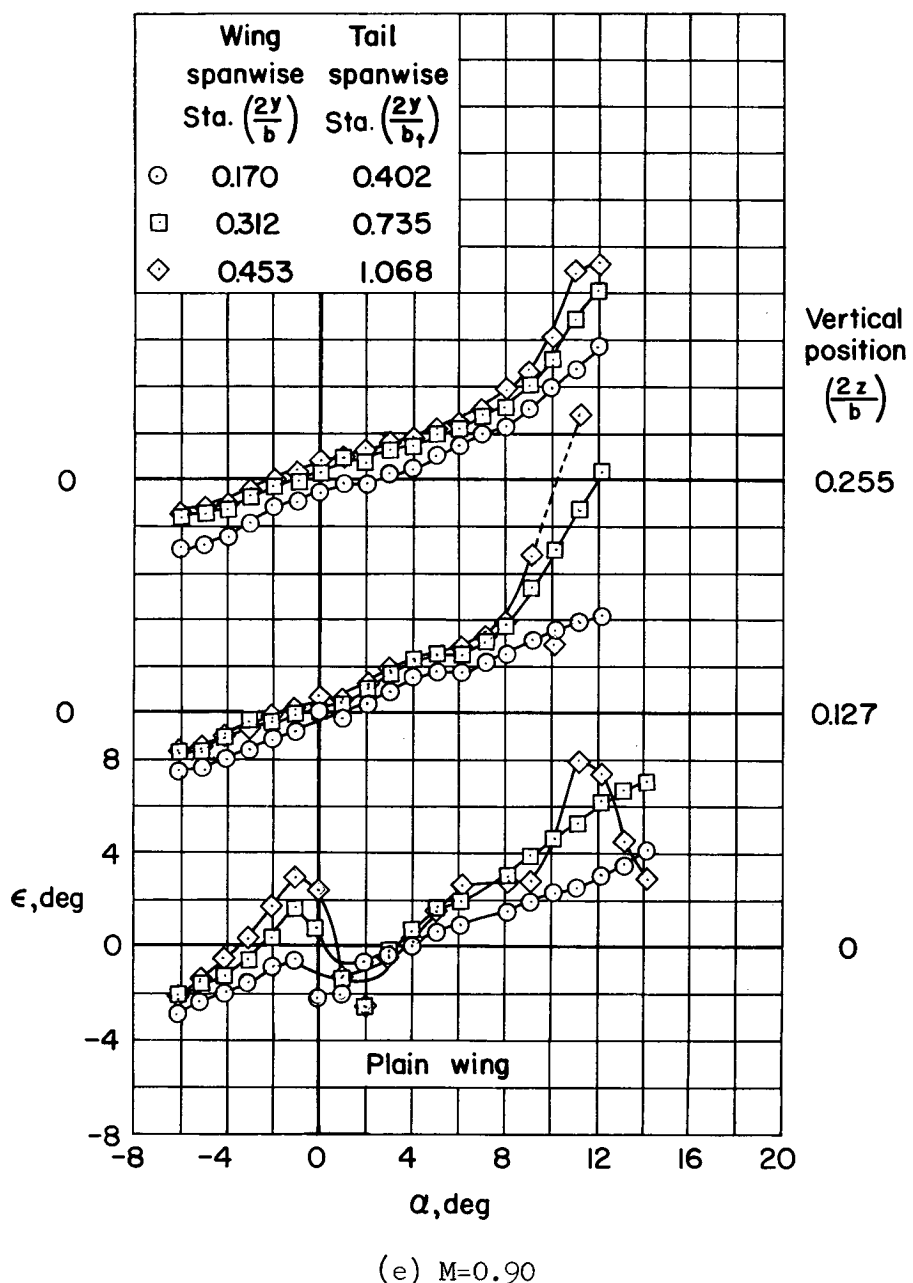


Figure 10.- Continued.

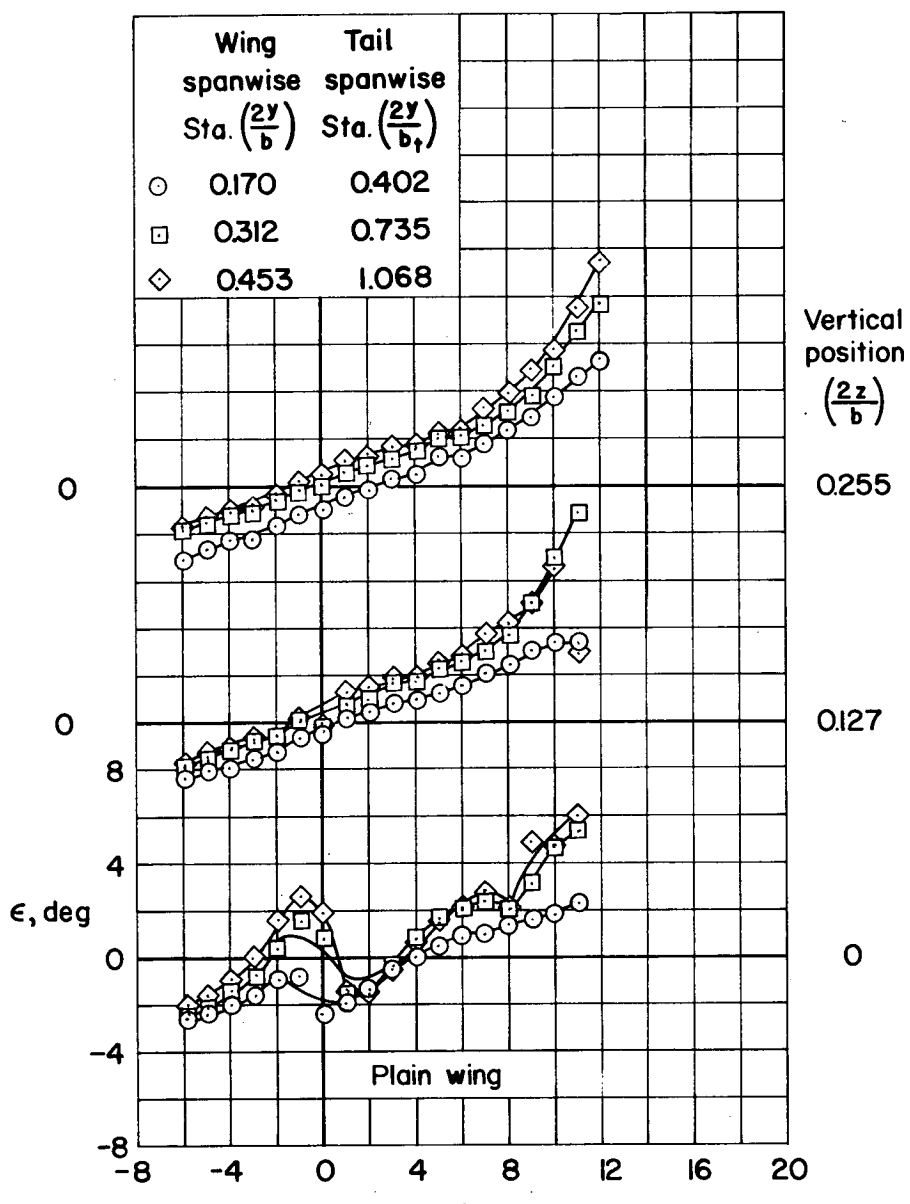
(f) $M=0.92$

Figure 10.- Concluded.

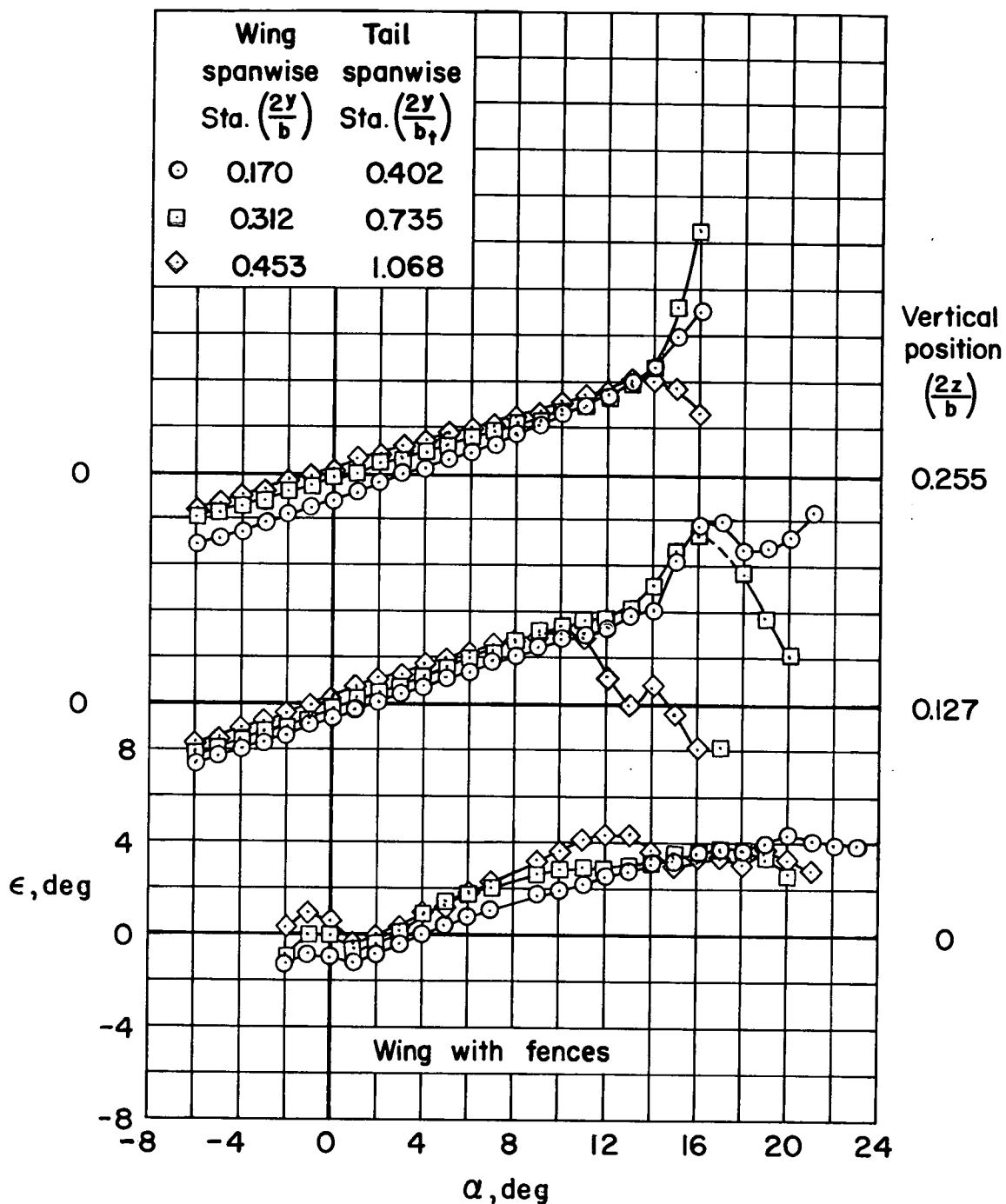


Figure 11.- The variation of local downwash with angle of attack at various points along the horizontal tail span and for three vertical locations. Wing with fences; $M=0.25$; $R=10,000,000$.

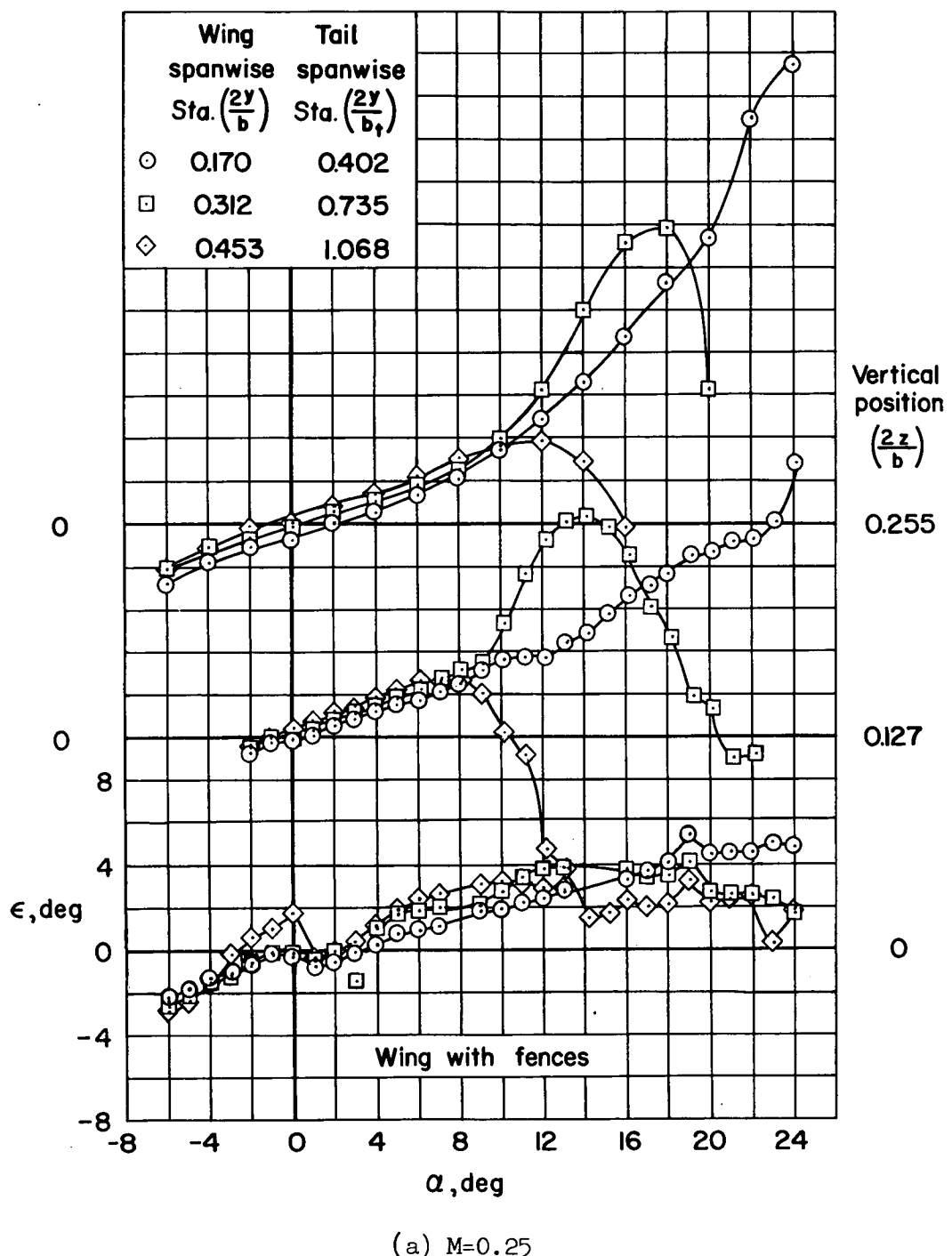


Figure 12.- The variation of local downwash with angle of attack at various points along the horizontal tail span and for three vertical locations. Wing with fences; $R=2,000,000$.

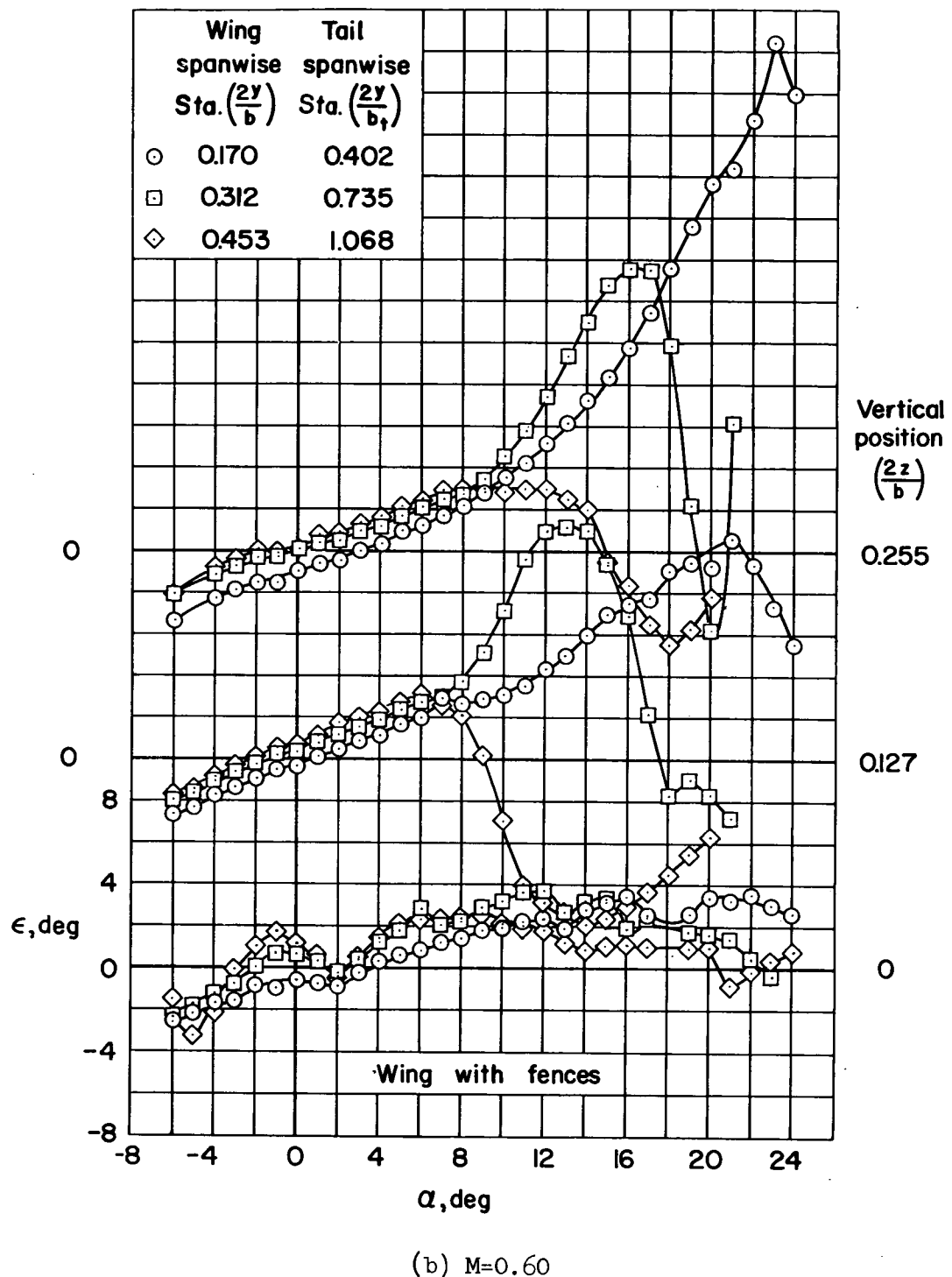


Figure 12.- Continued.

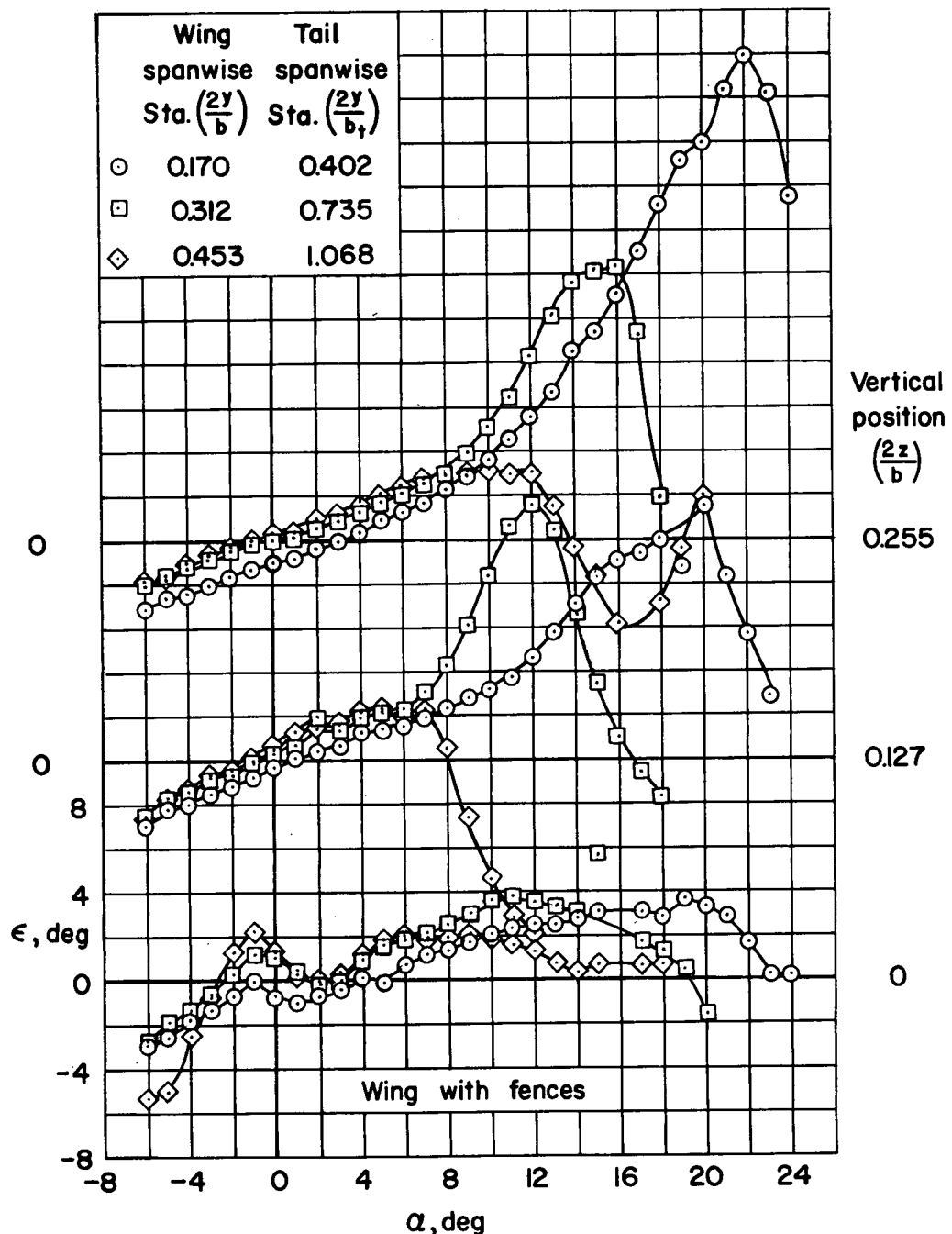
(c) $M=0.80$

Figure 12.- Continued.

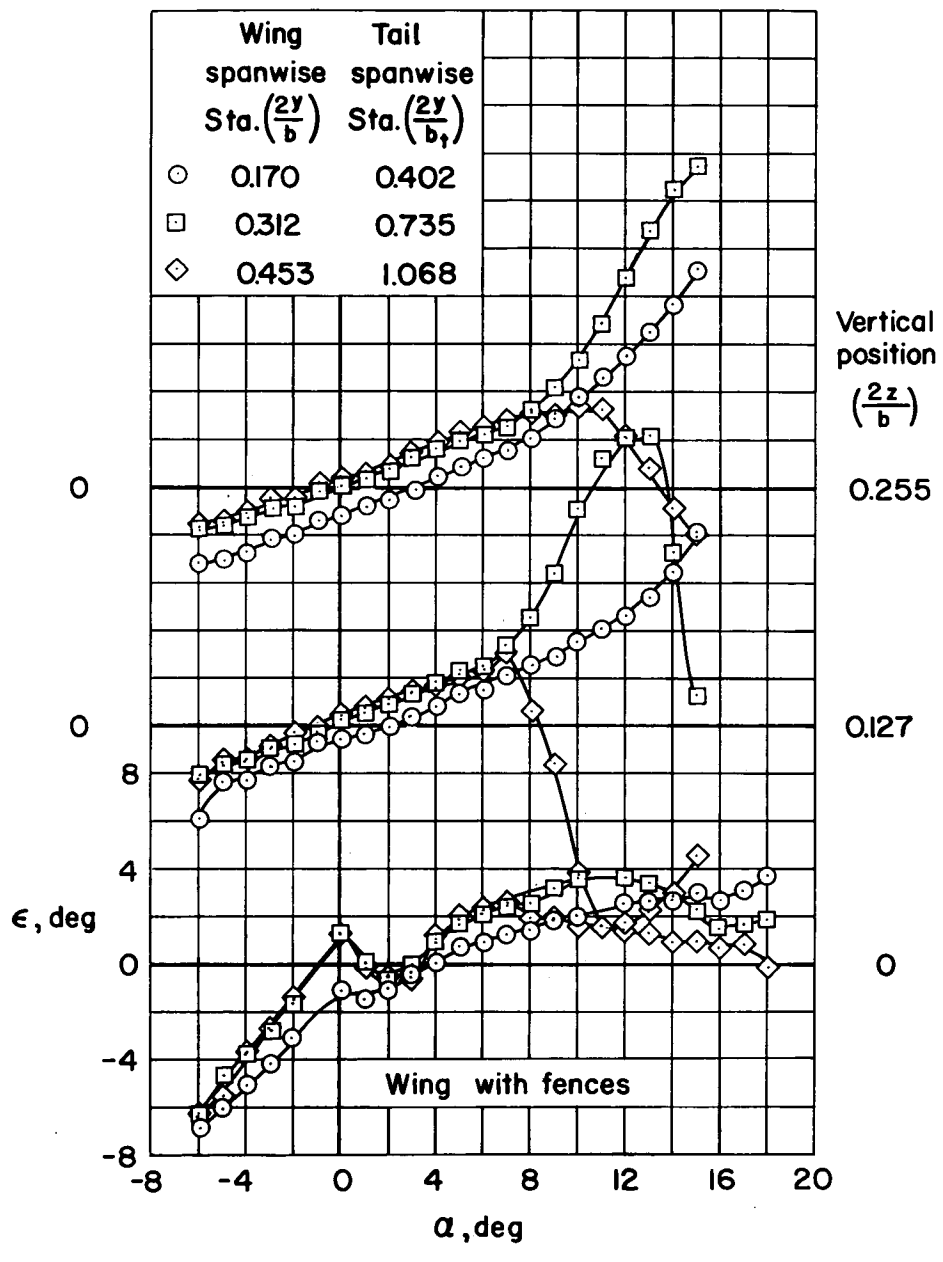


Figure 12.- Continued.

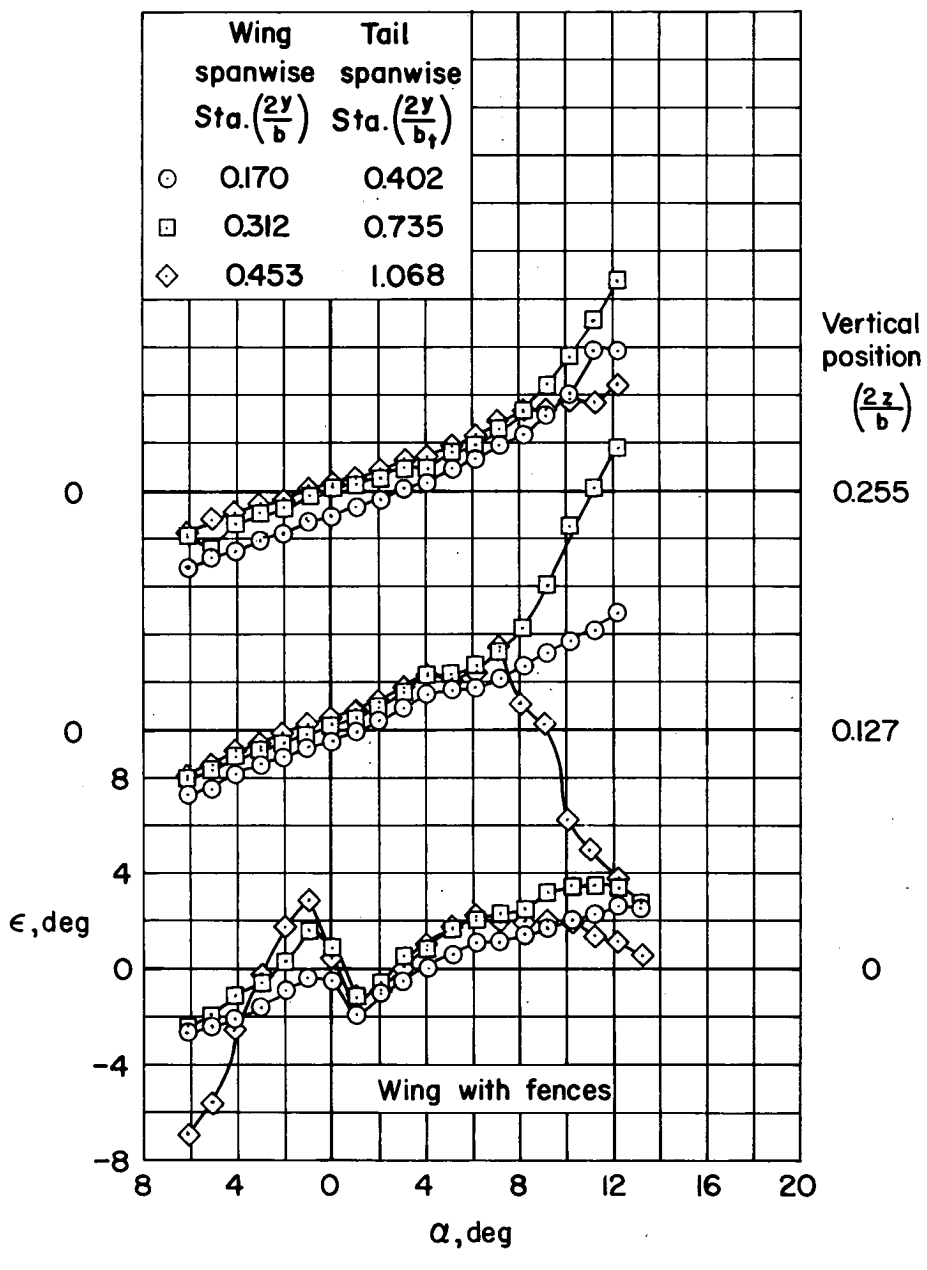


Figure 12.- Continued.

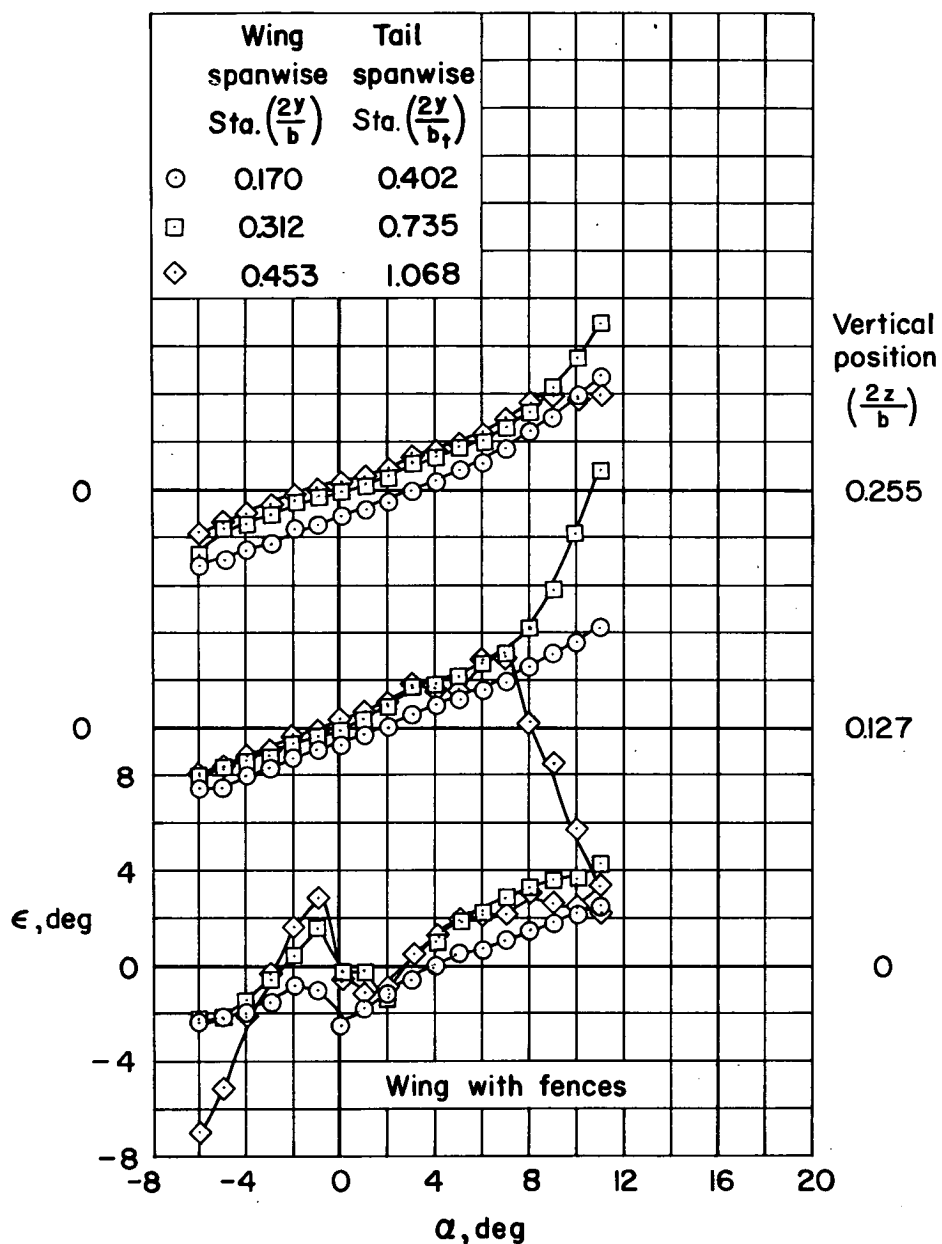
(f) $M=0.92$

Figure 12.- Concluded.

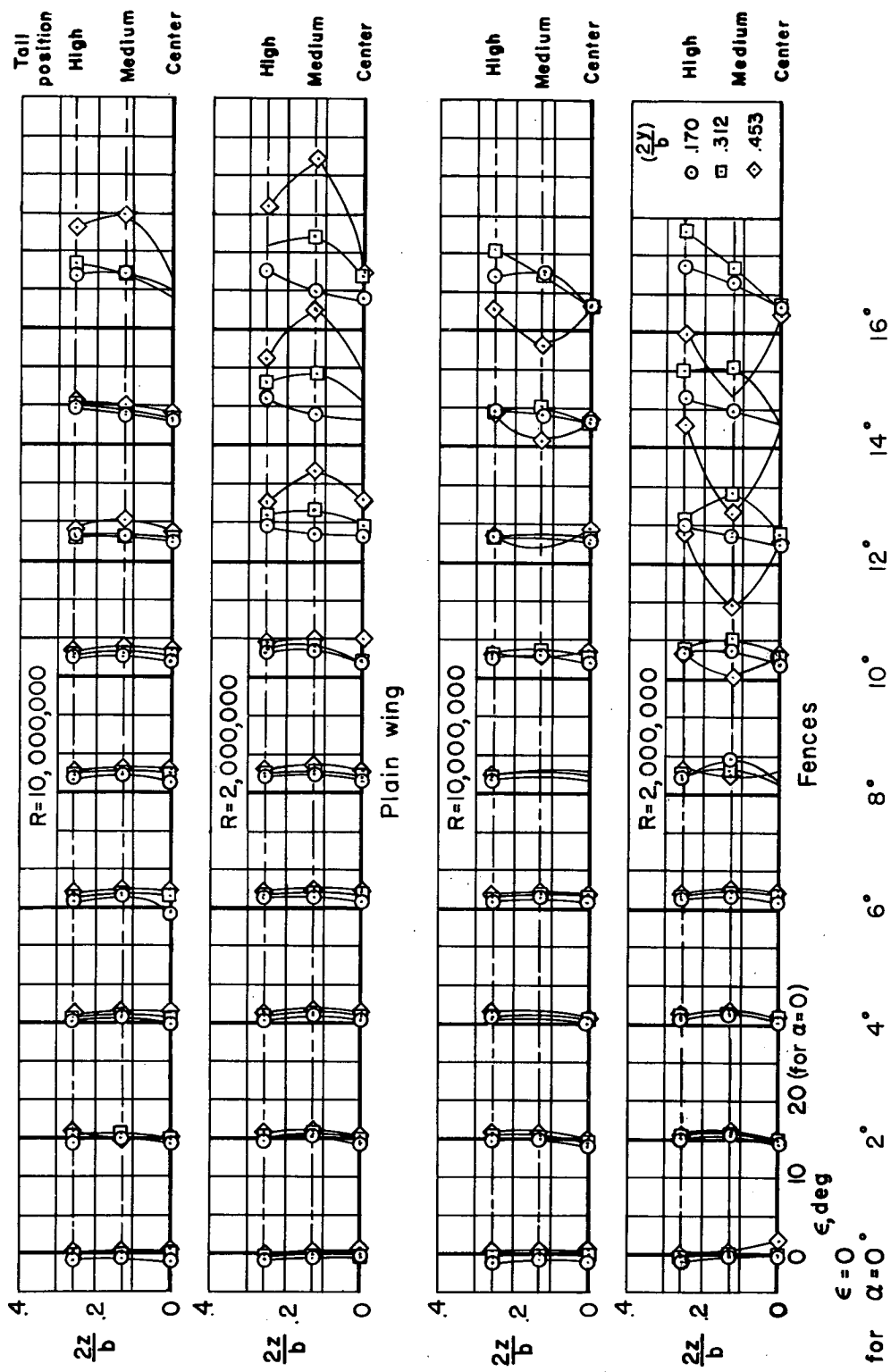
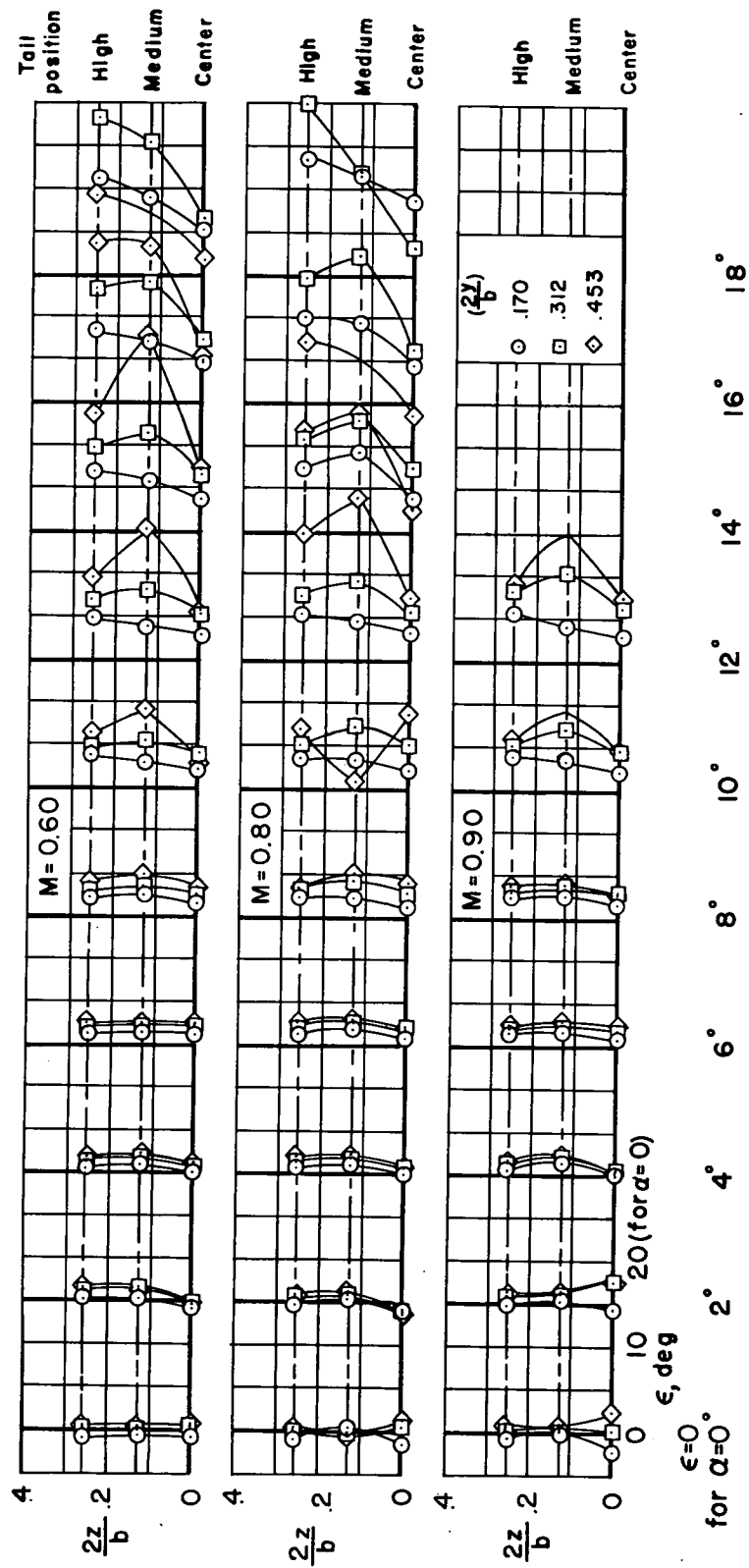
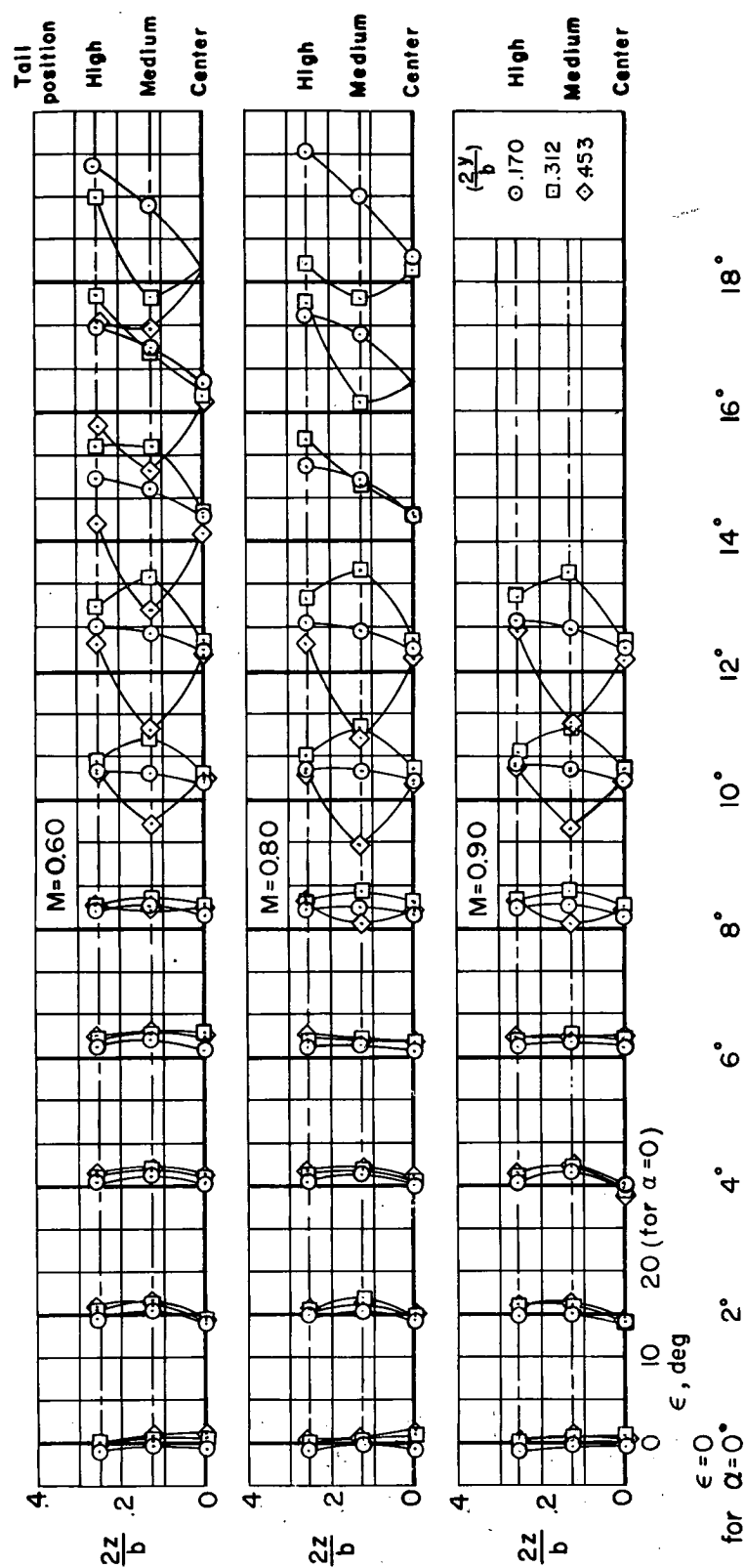


Figure 13.- The vertical distribution of measured local downwash for various angles of attack;
 $M=0.25$.



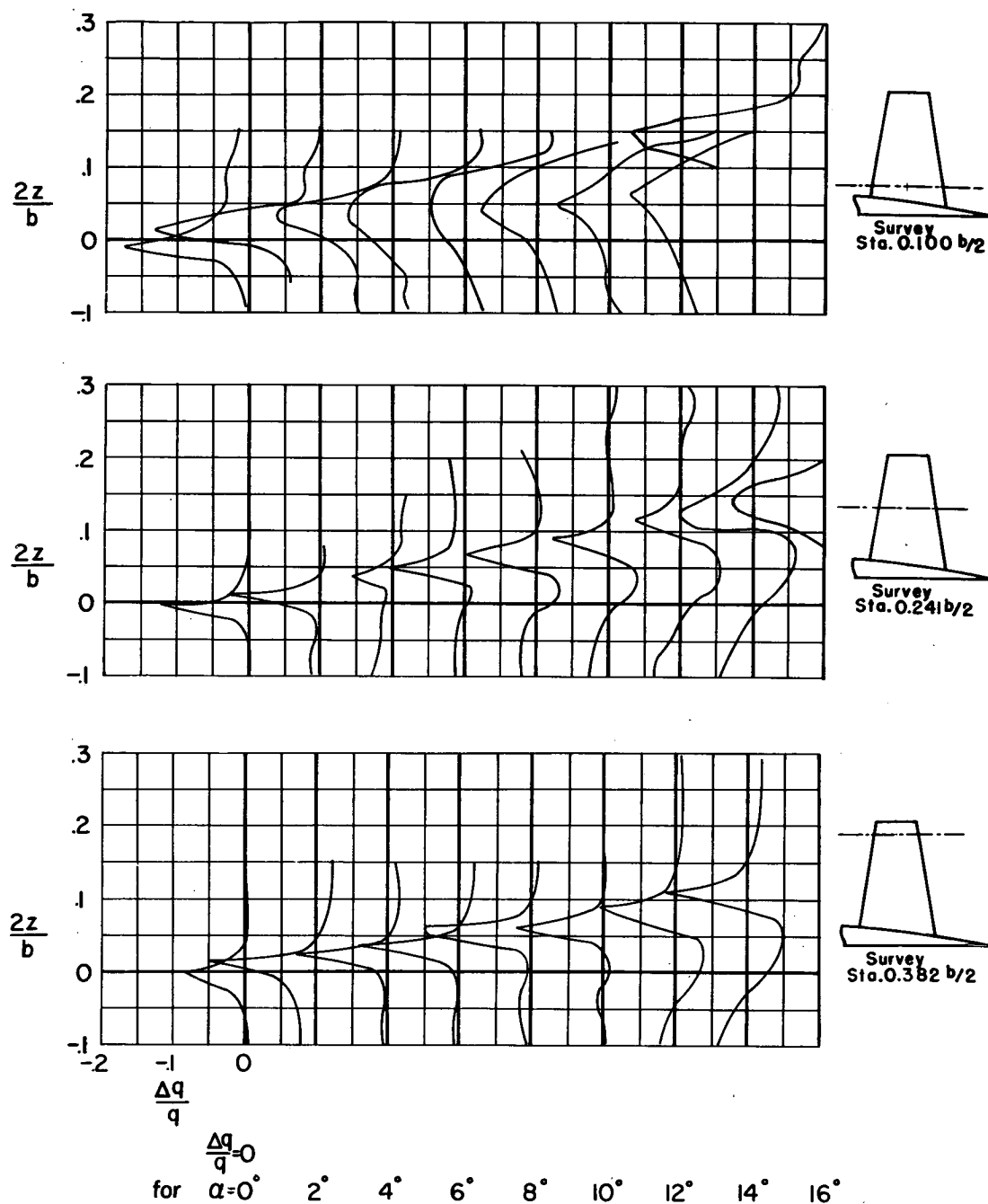
(a) Plain wing.

Figure 14.- The vertical distribution of measured local downwash for various angles of attack;
 $R=2,000,000$.



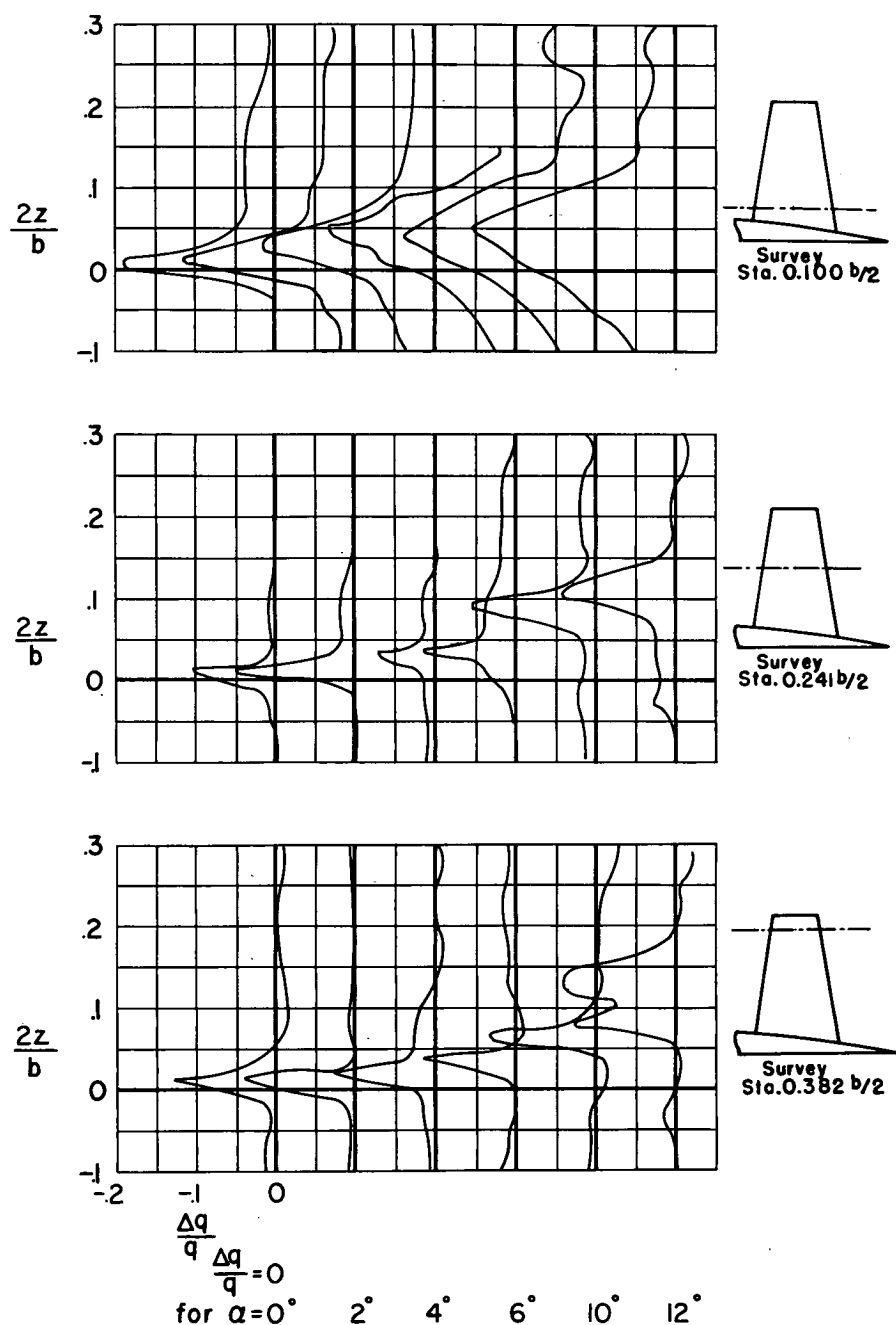
(b) Wing with fences.

Figure 14.- Concluded.



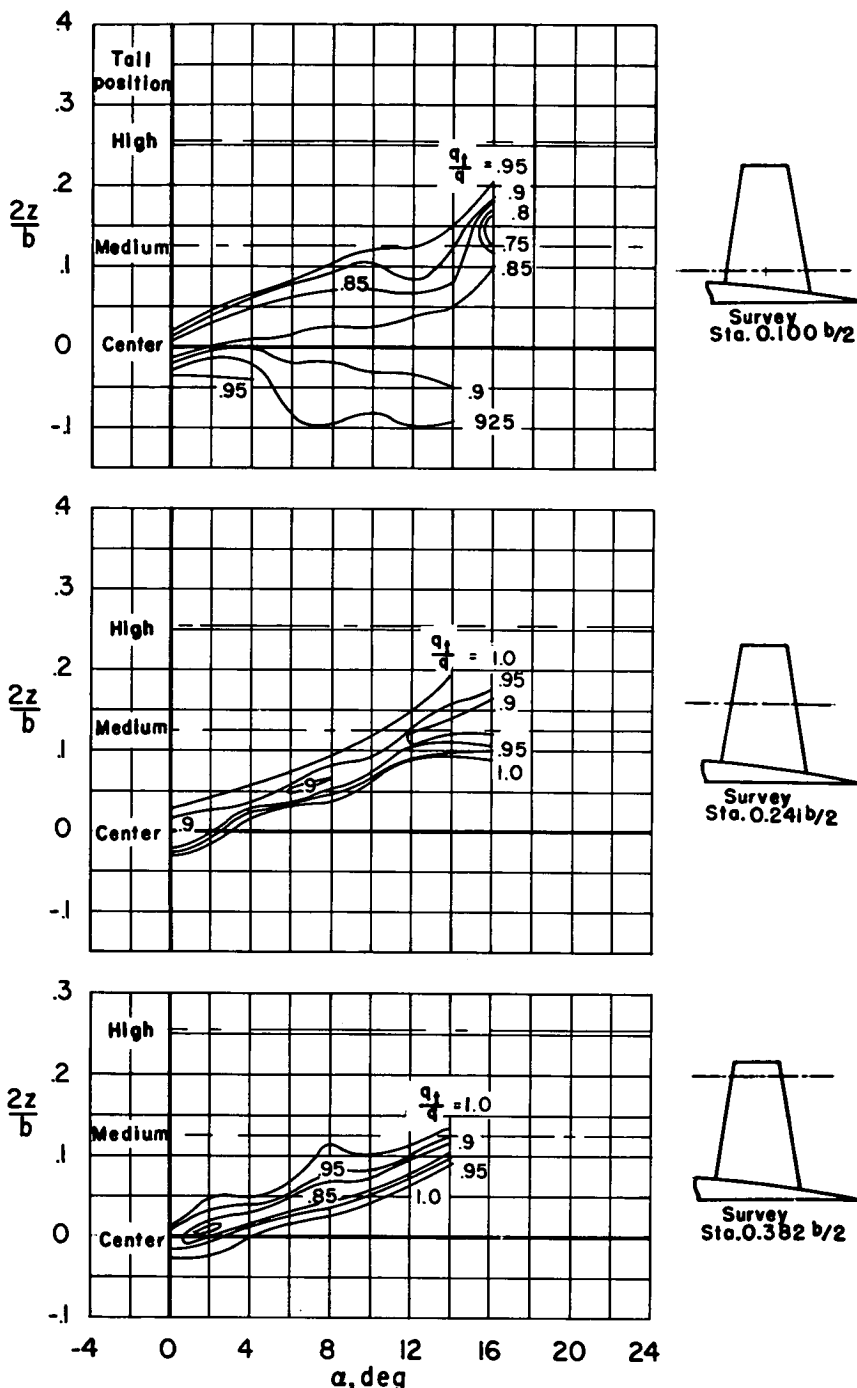
(a) Plain wing.

Figure 15.- The vertical distribution of dynamic-pressure increment in the wing wake at various angles of attack for three spanwise stations along the tail; $M=0.25$; $R=10,000,000$.



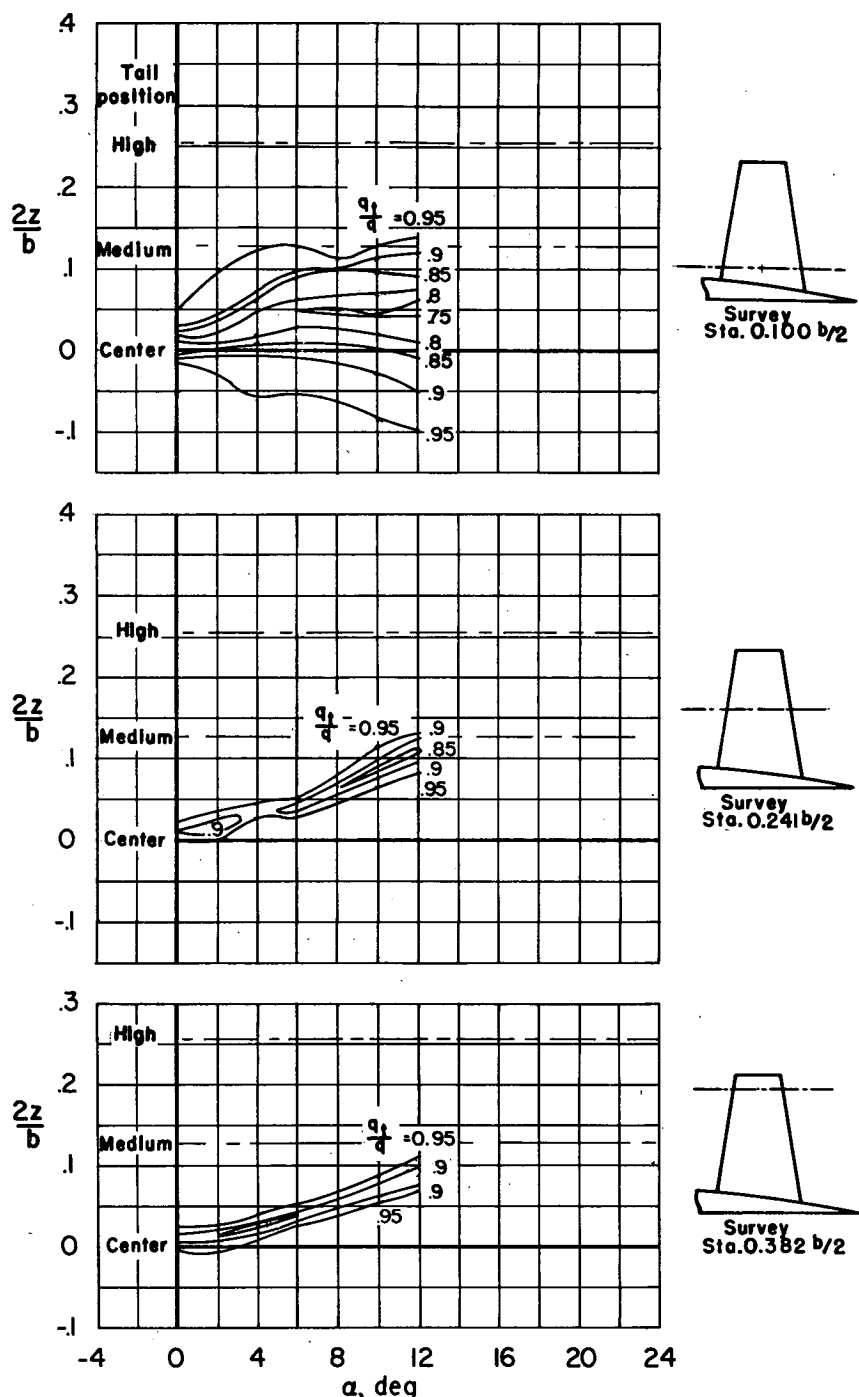
(b) Wing with fences.

Figure 15.- Concluded.



(a) Plain wing.

Figure 16.- The effect of angle of attack on the vertical distribution of dynamic pressure at the tail at three spanwise stations; $M=0.25$; $R=10,000,000$.



(b) Wing with fences.

Figure 16.- Concluded.

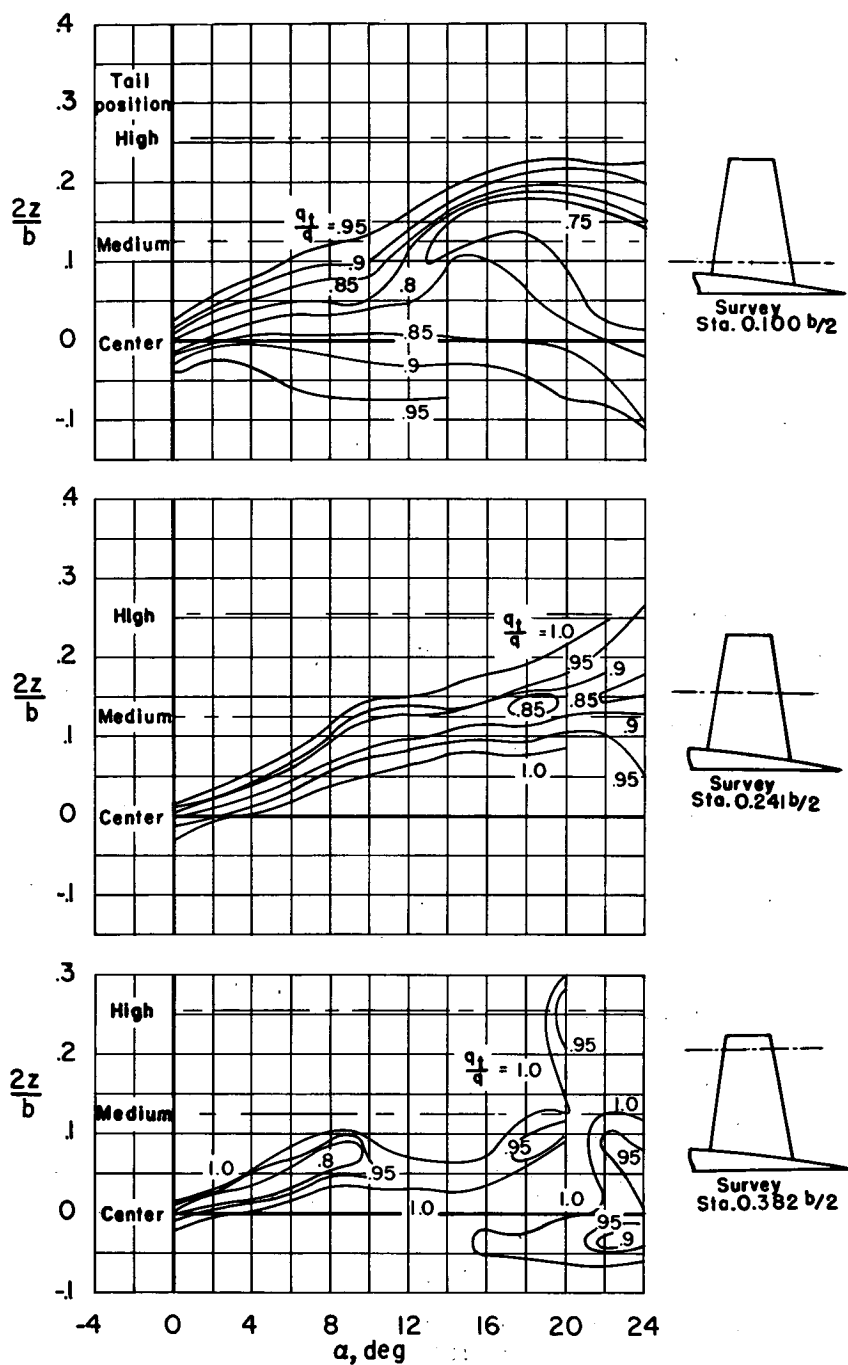
(a) $M=0.25$

Figure 17.- The effect of angle of attack on the vertical distribution of dynamic pressure at the tail at three spanwise stations. Plain wing; $R=2,000,000$.

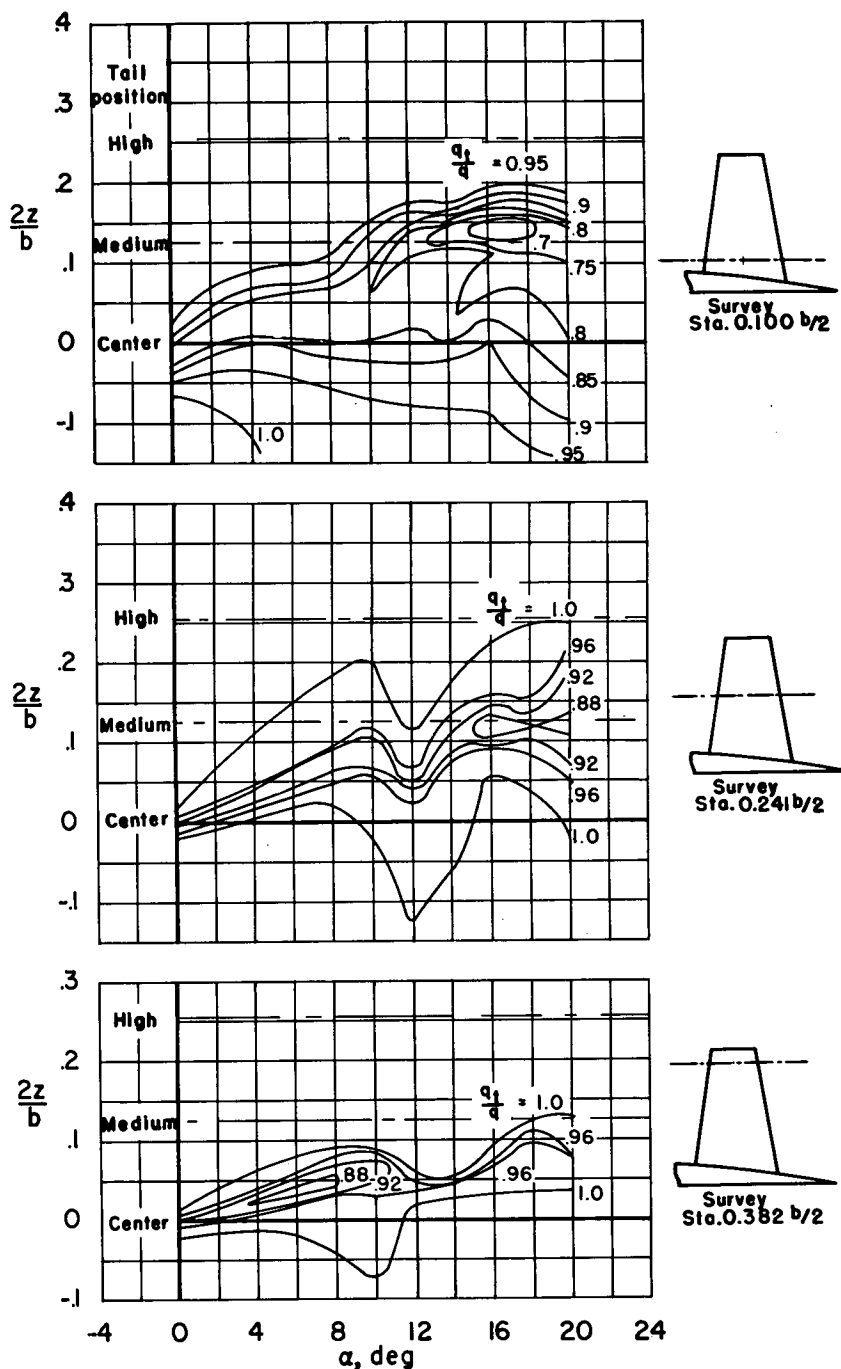
(b) $M=0.60$

Figure 17.- Continued.

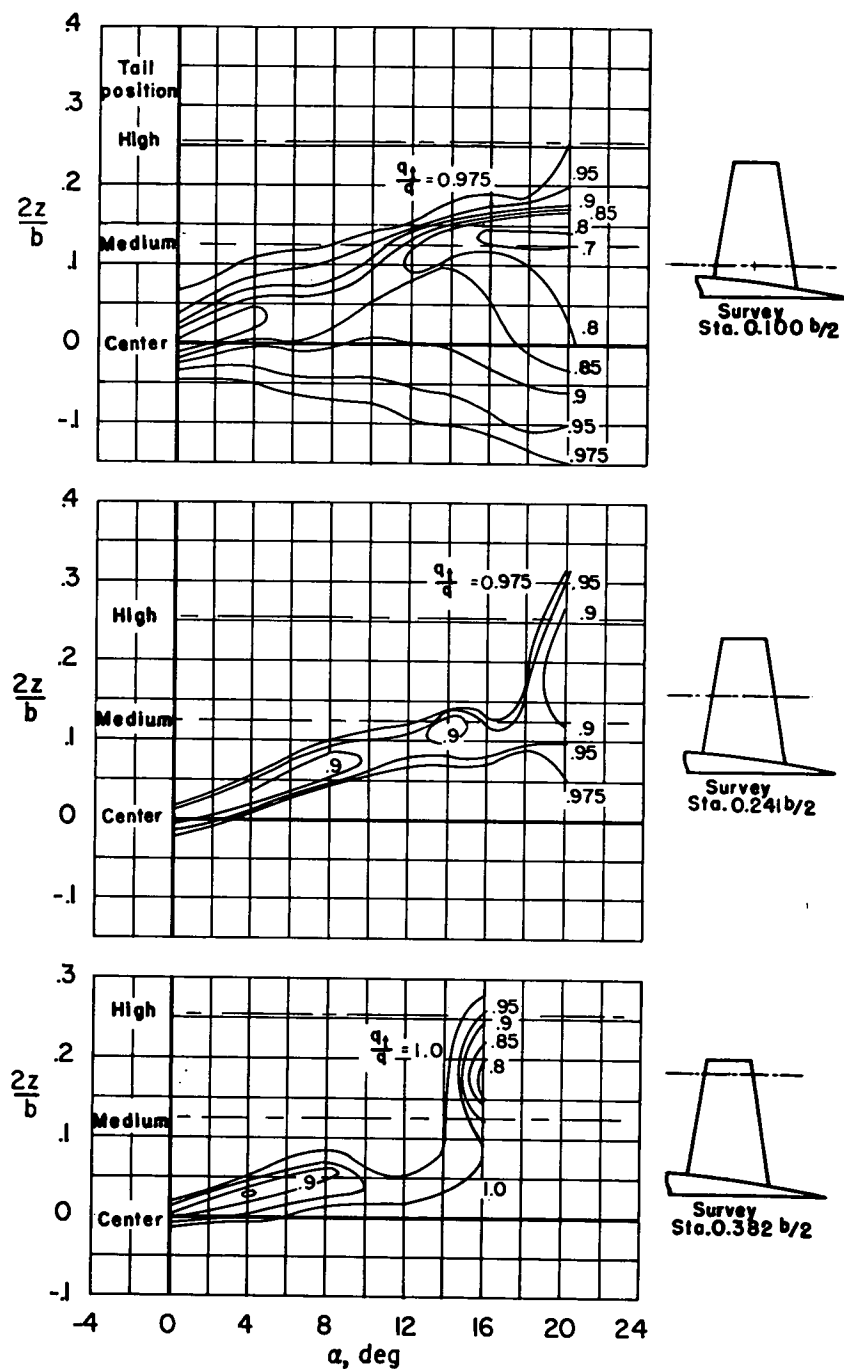
(c) $M=0.80$

Figure 17.- Continued.

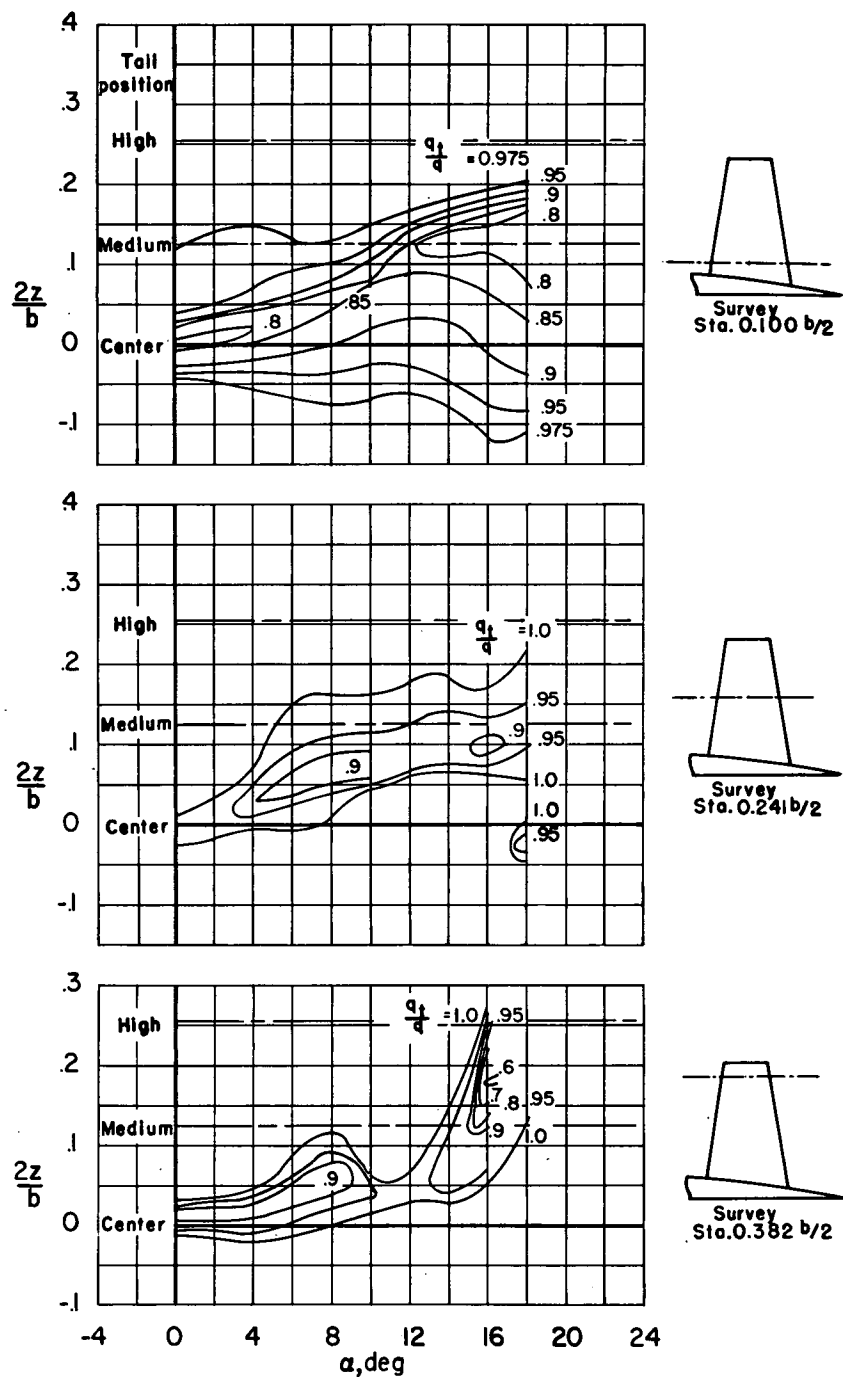
(d) $M=0.85$

Figure 17.- Continued.

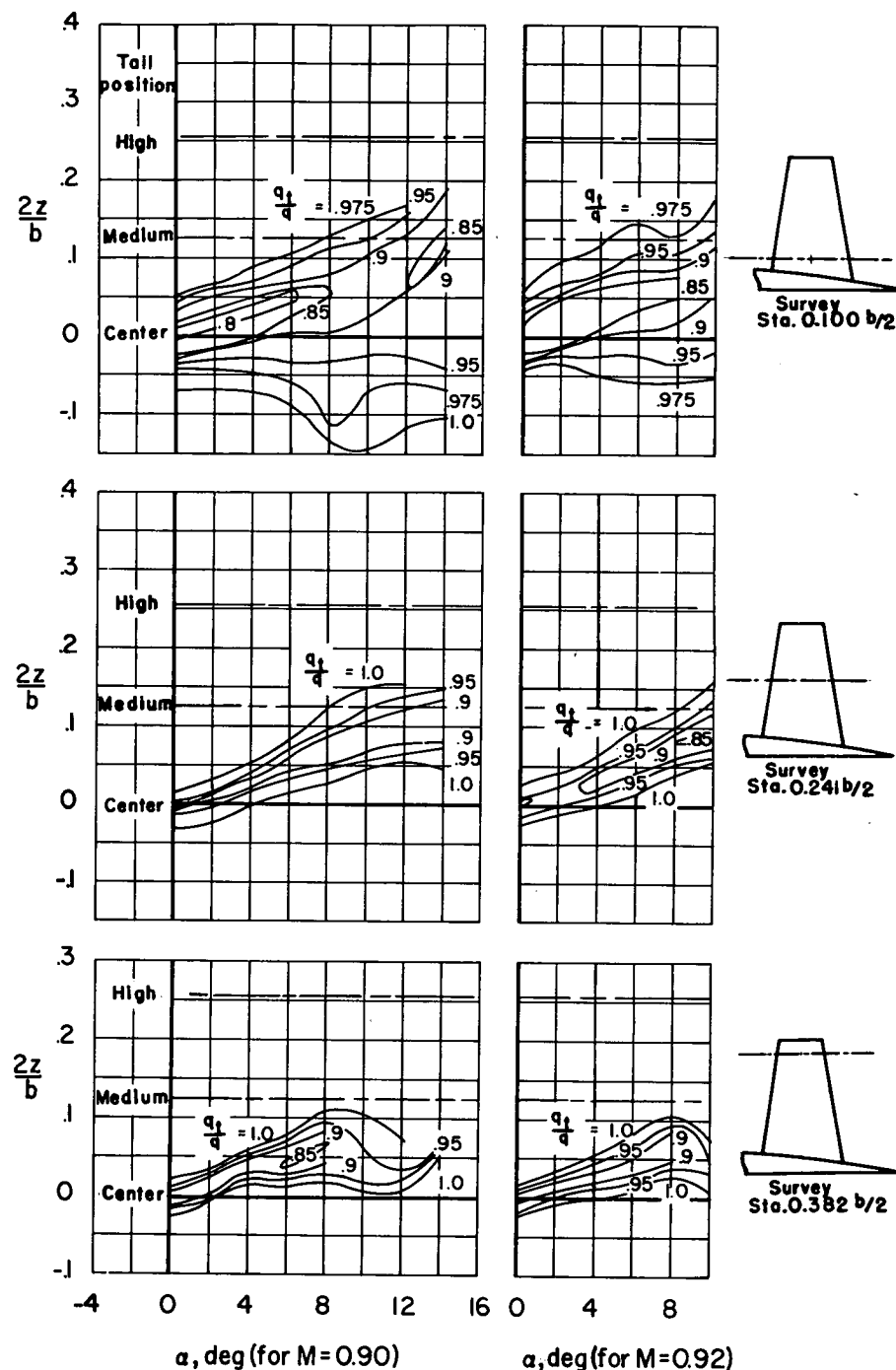
(e) $M=0.90, 0.92$

Figure 17.- Concluded.

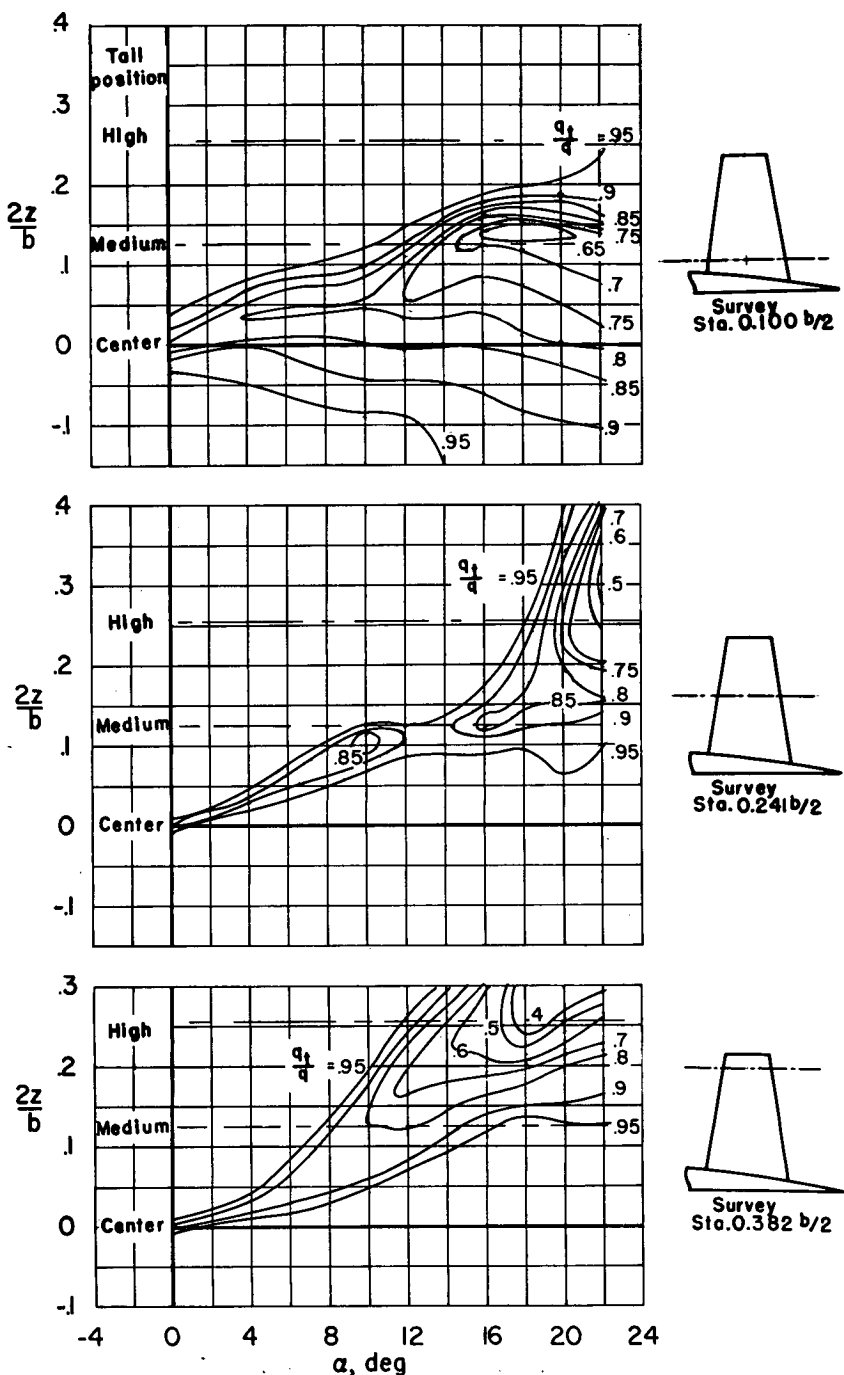
(a) $M=0.25$

Figure 18.- The effect of angle of attack on the vertical distribution of dynamic pressure at the tail at three spanwise stations. Wing with fences; $R=2,000,000$.

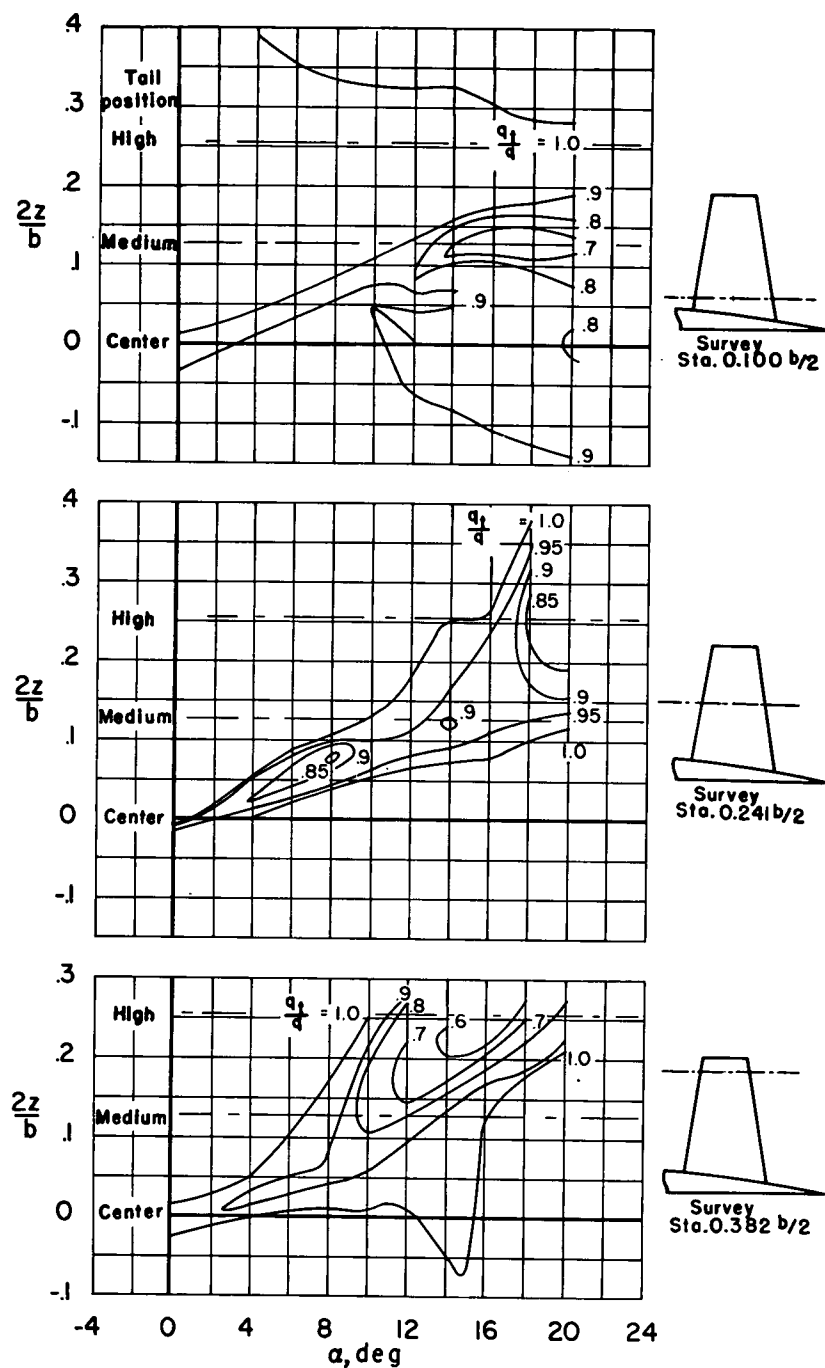
(b) $M=0.60$

Figure 18.- Continued.

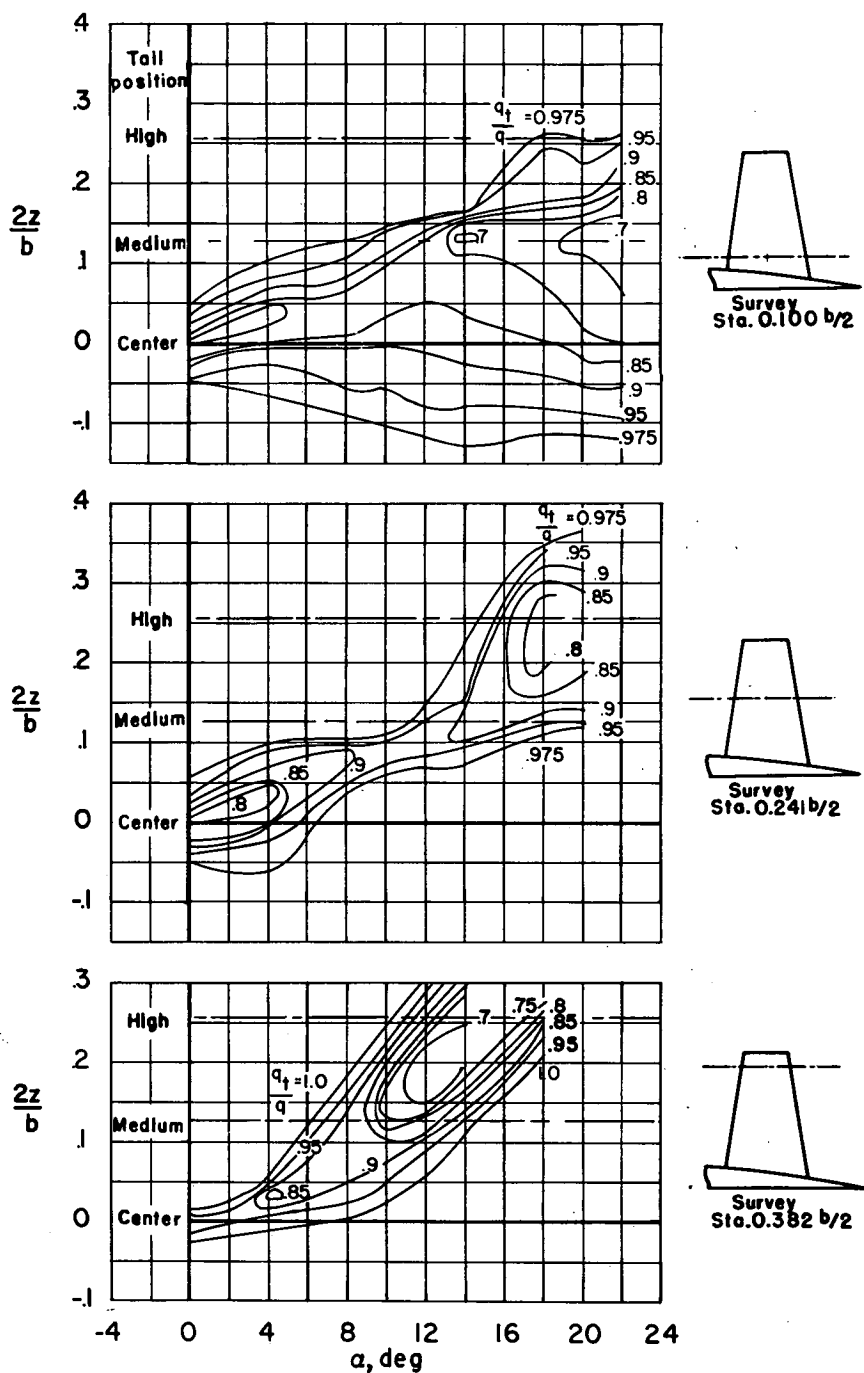
(c) $M=0.80$

Figure 18.- Continued.

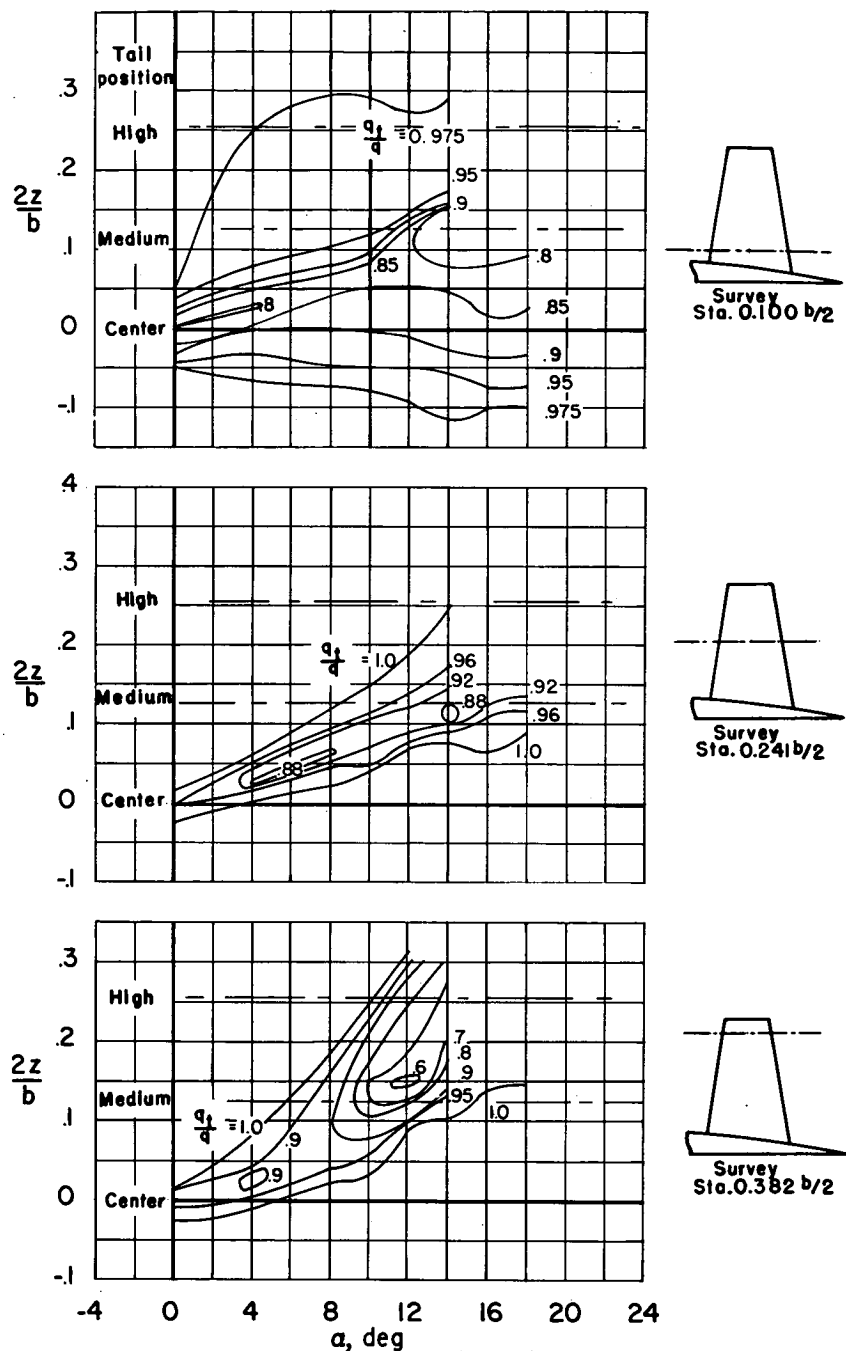
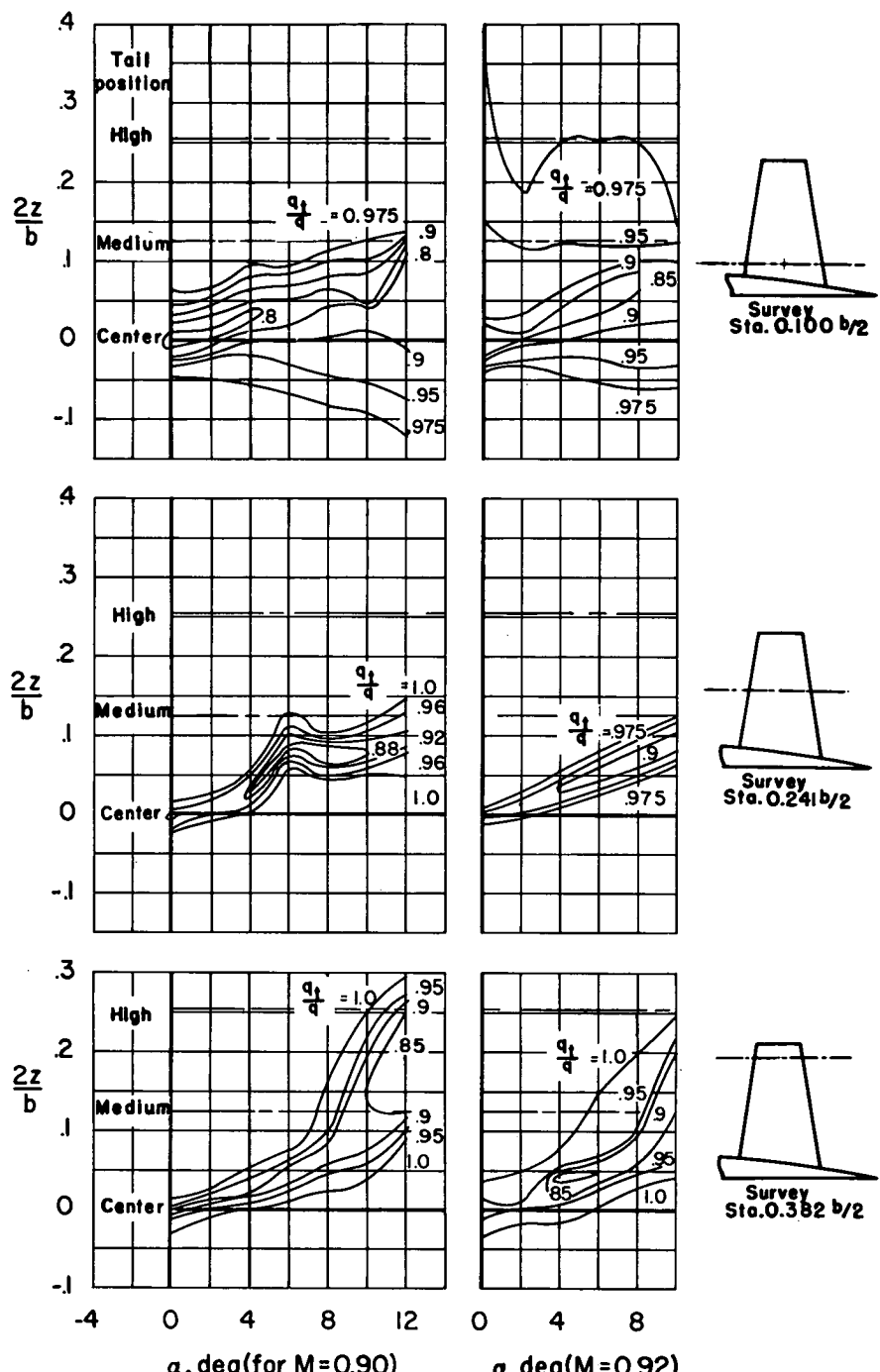
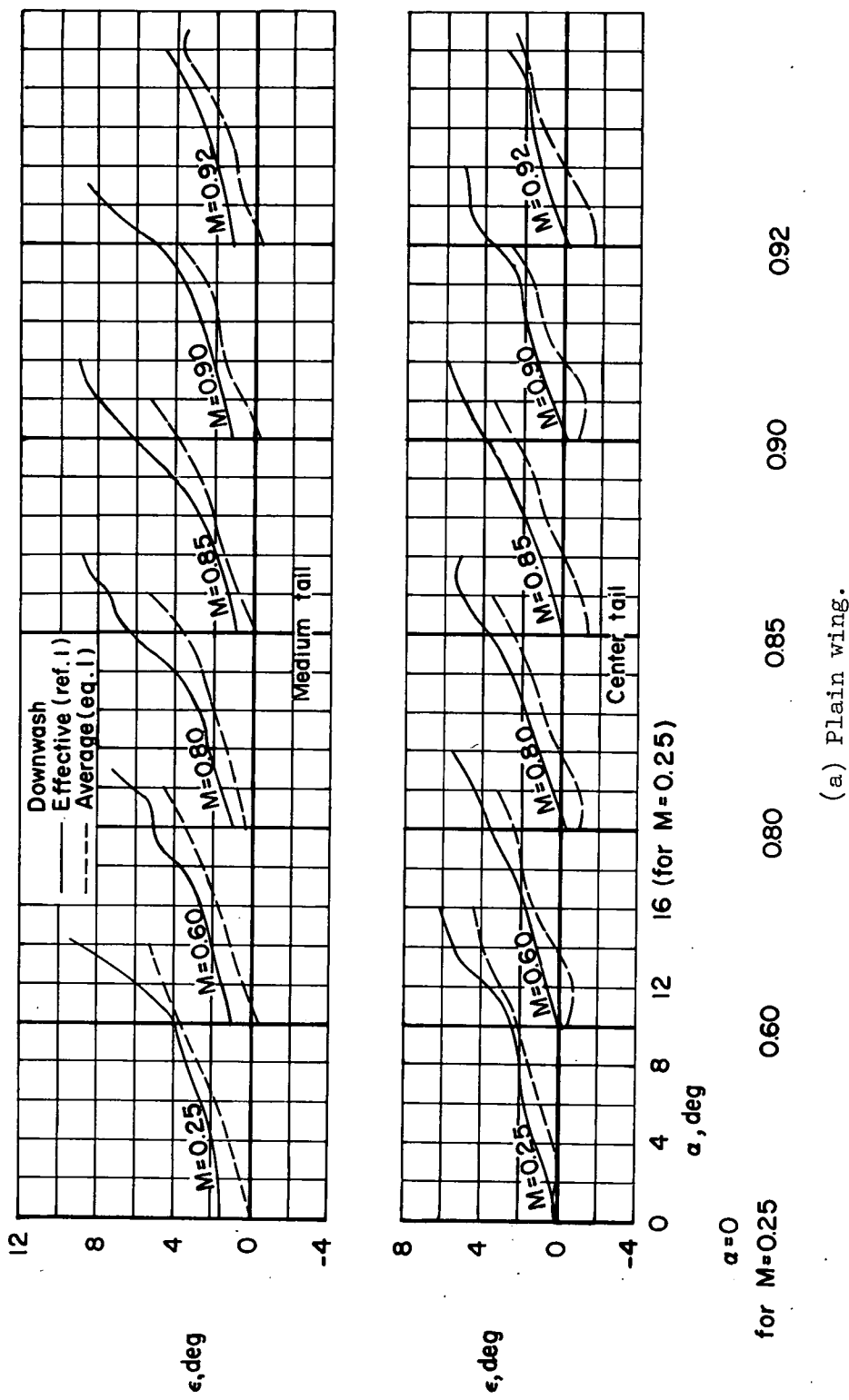
(d) $M=0.85$

Figure 18.- Continued.



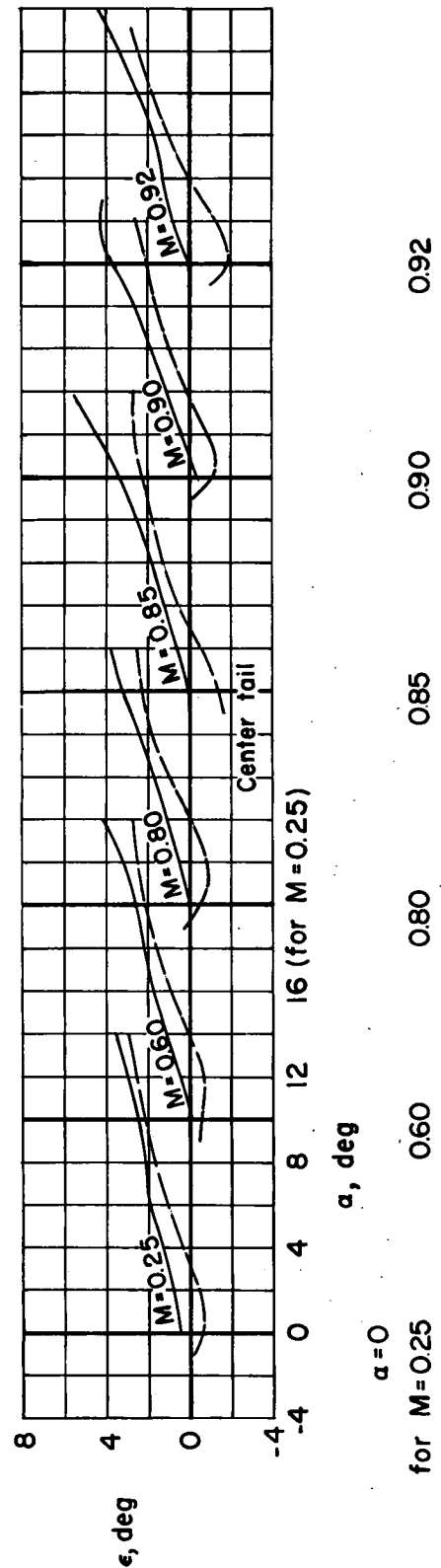
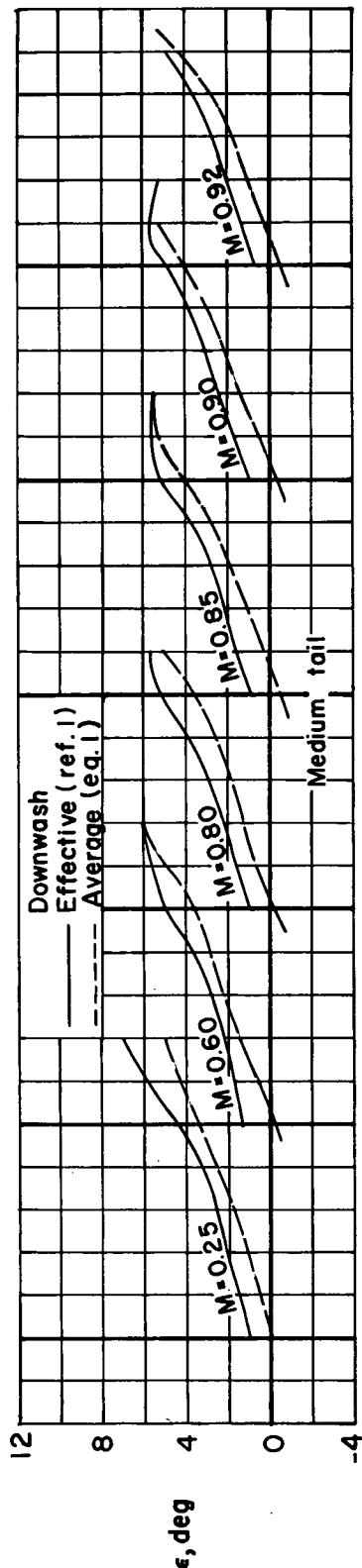
(e) $M=0.90, 0.92$

Figure 18.- Concluded



(a) Plain wing.

Figure 19.- The variations of effective and average downwash at the tail with angle of attack for various Mach numbers.



(b) Wing with fences.

Figure 19.- Concluded.

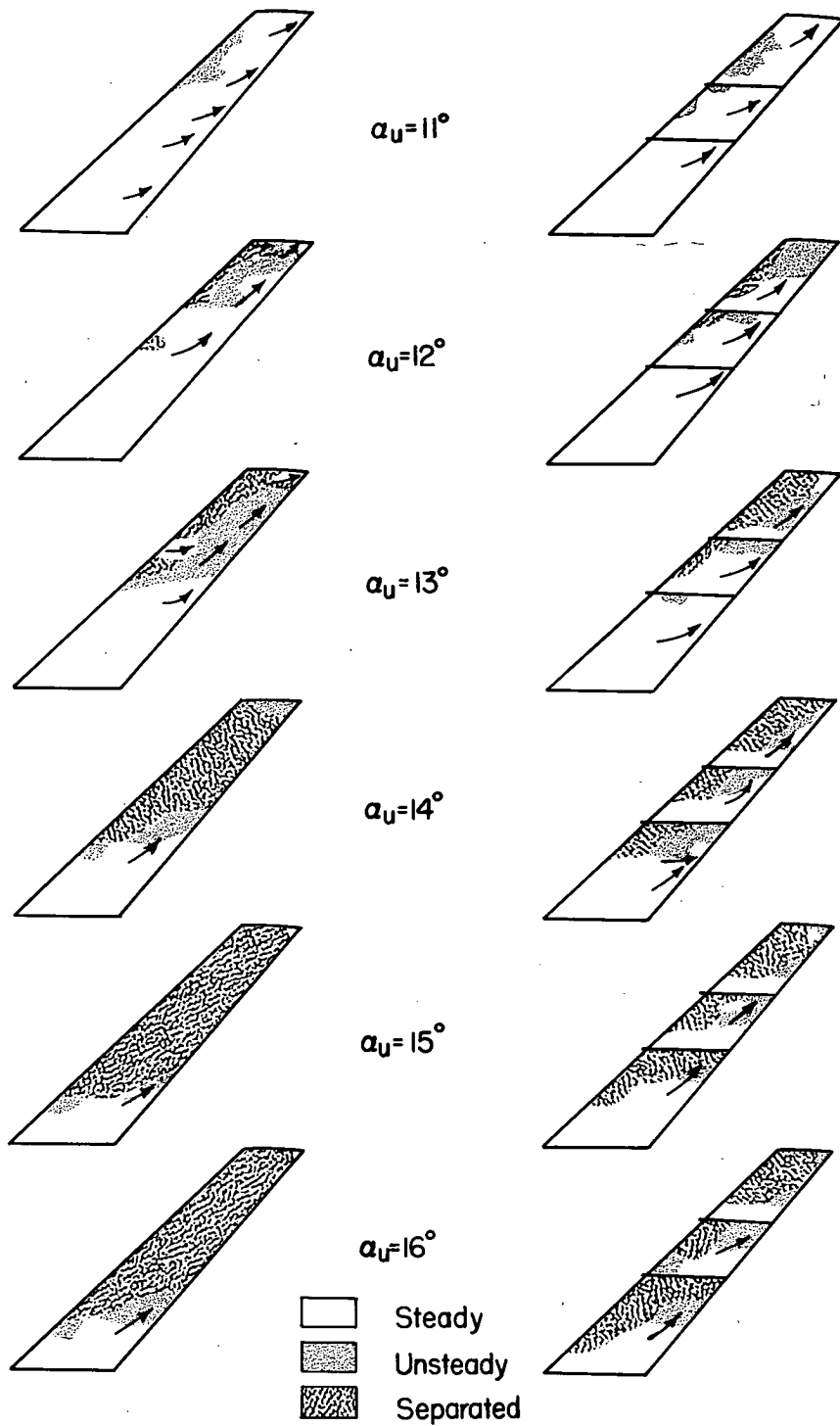


Figure 20.- Separation patterns on the wing, with and without fences;
 $M=0.25$; $R=10,000,000$.

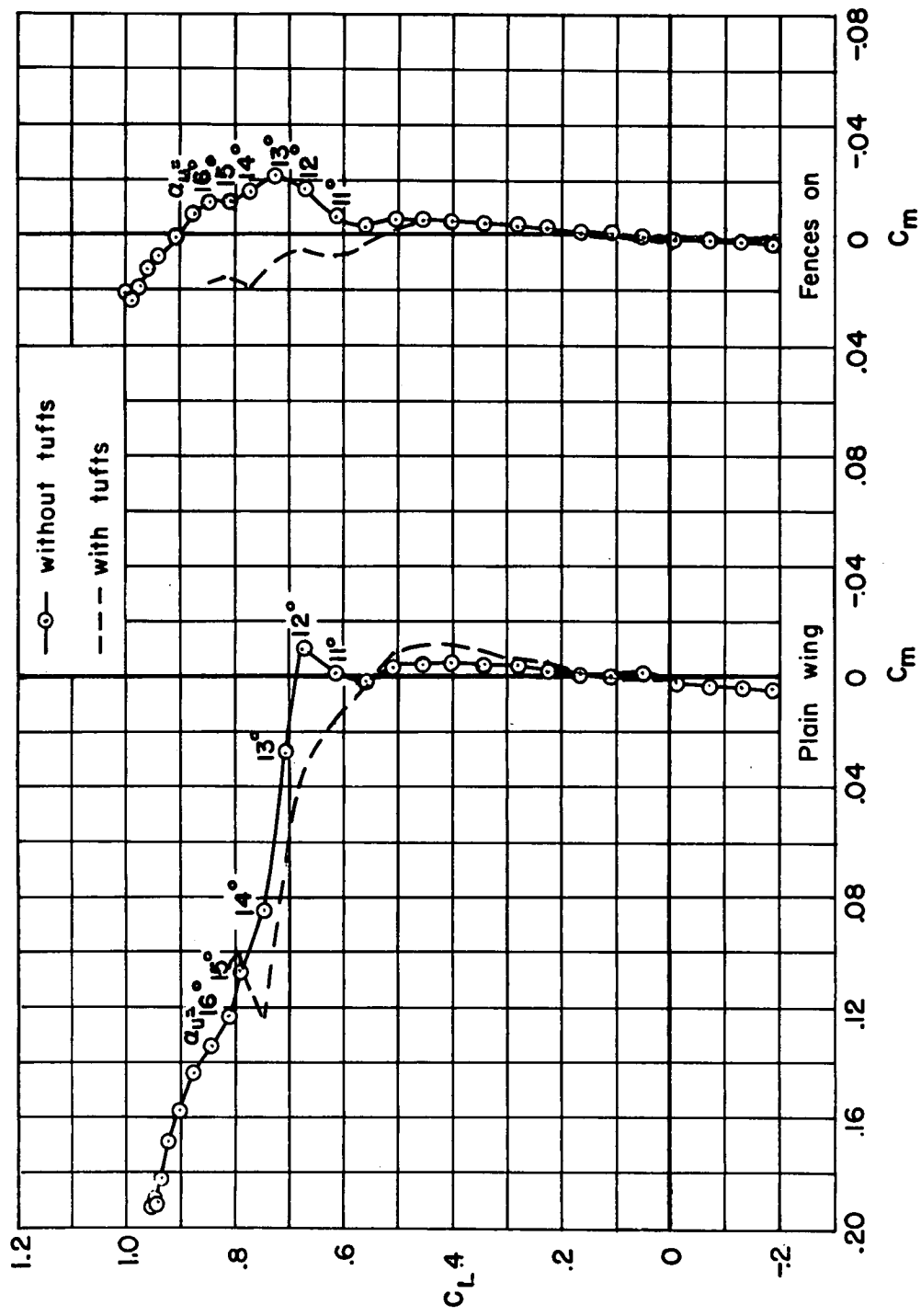


Figure 21. - Pitching-moment characteristics of the model with and without tufts; $M=0.25$; $R=10,000,000$.

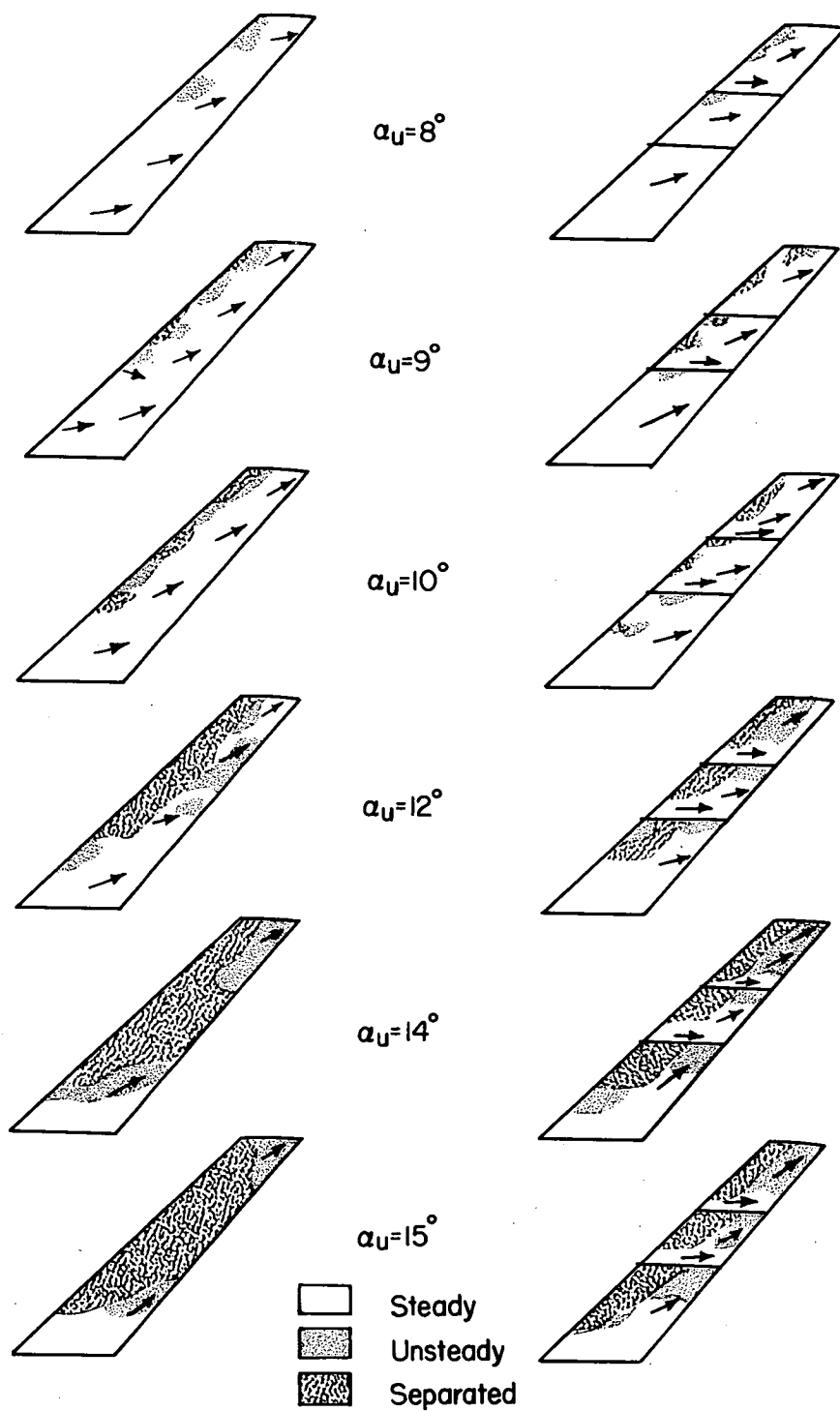


Figure 22.- Separation patterns on the wing, with and without fences;
 $M=0.25$; $R=2,000,000$.

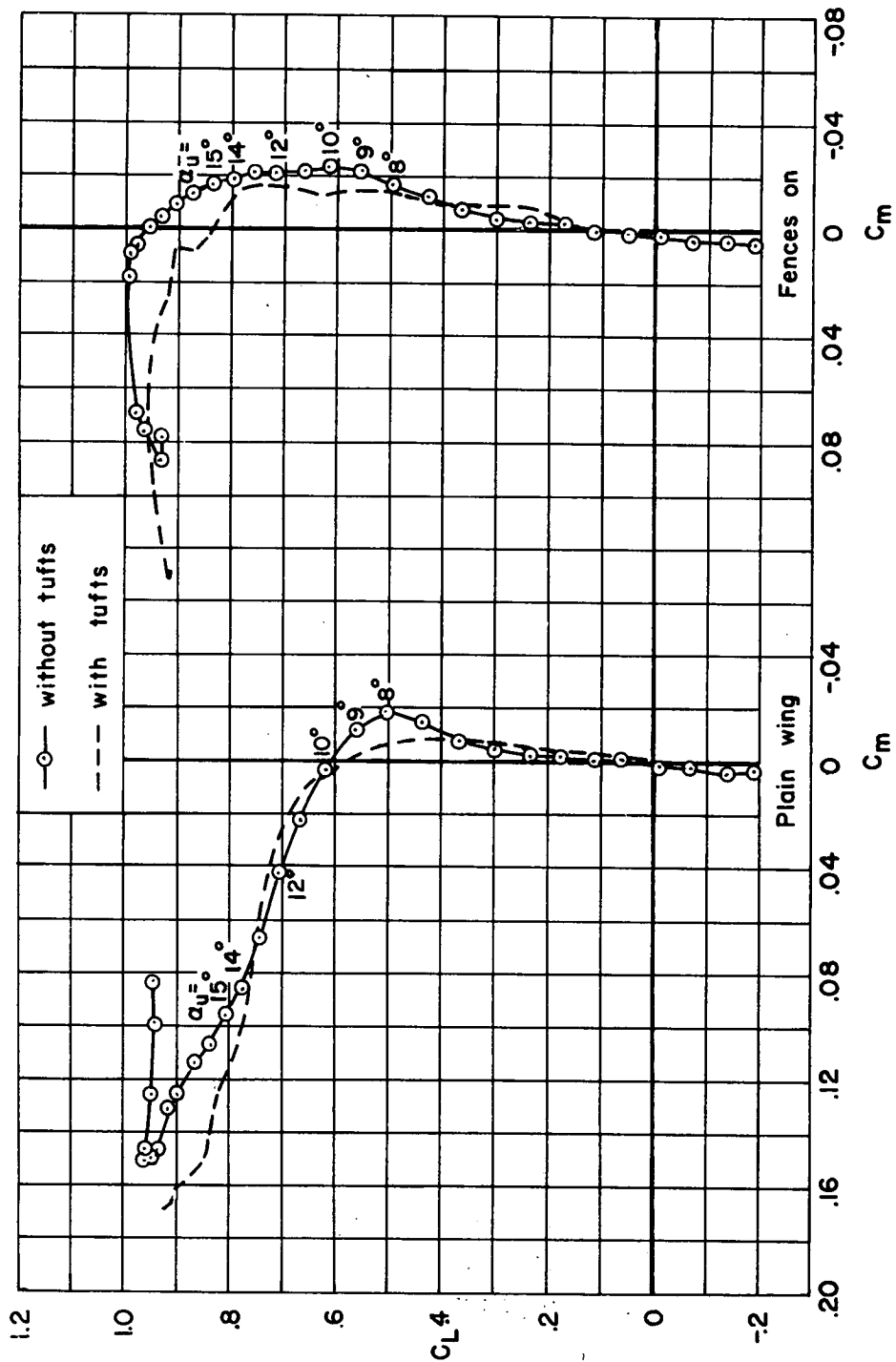


Figure 23. - Pitching-moment characteristics of the model with and without tufts; $M=0.25$; $R=2,000,000$.

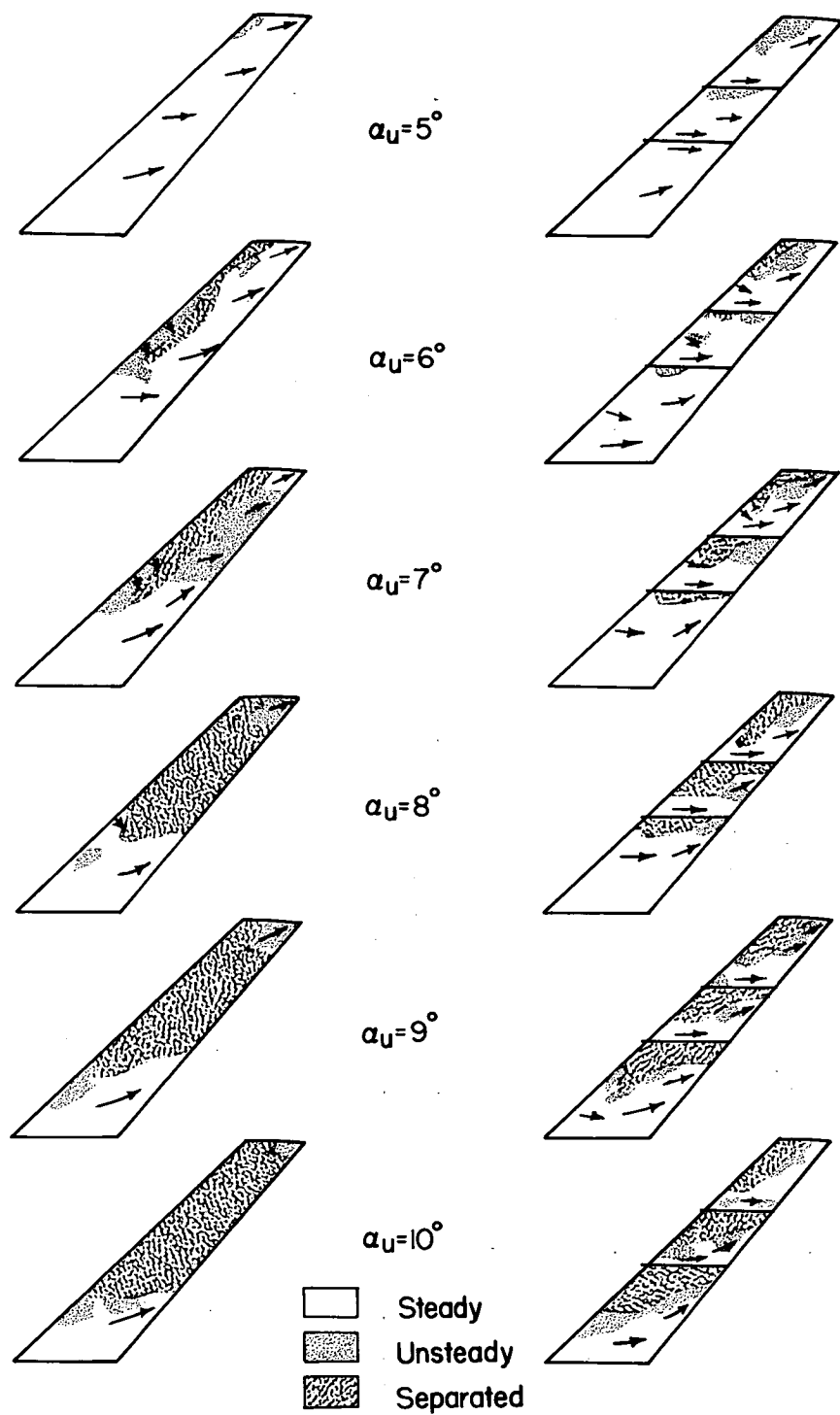


Figure 24.- Separation patterns on the wing, with and without fences;
 $M=0.85$; $R=2,000,000$.

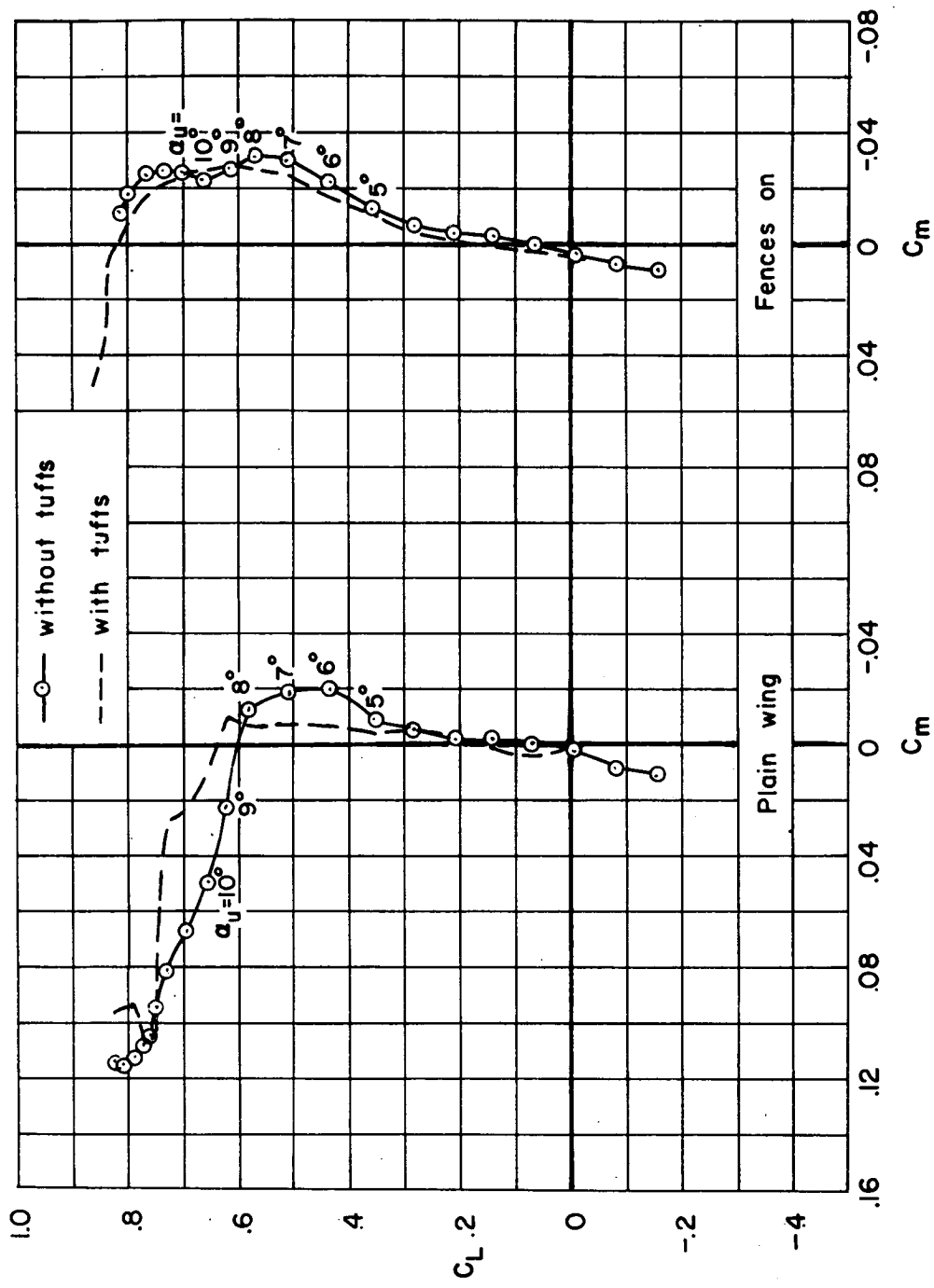


Figure 25.— Pitching-moment characteristics of the model with and without tufts; $M=0.85$; $R=2,000,000$.

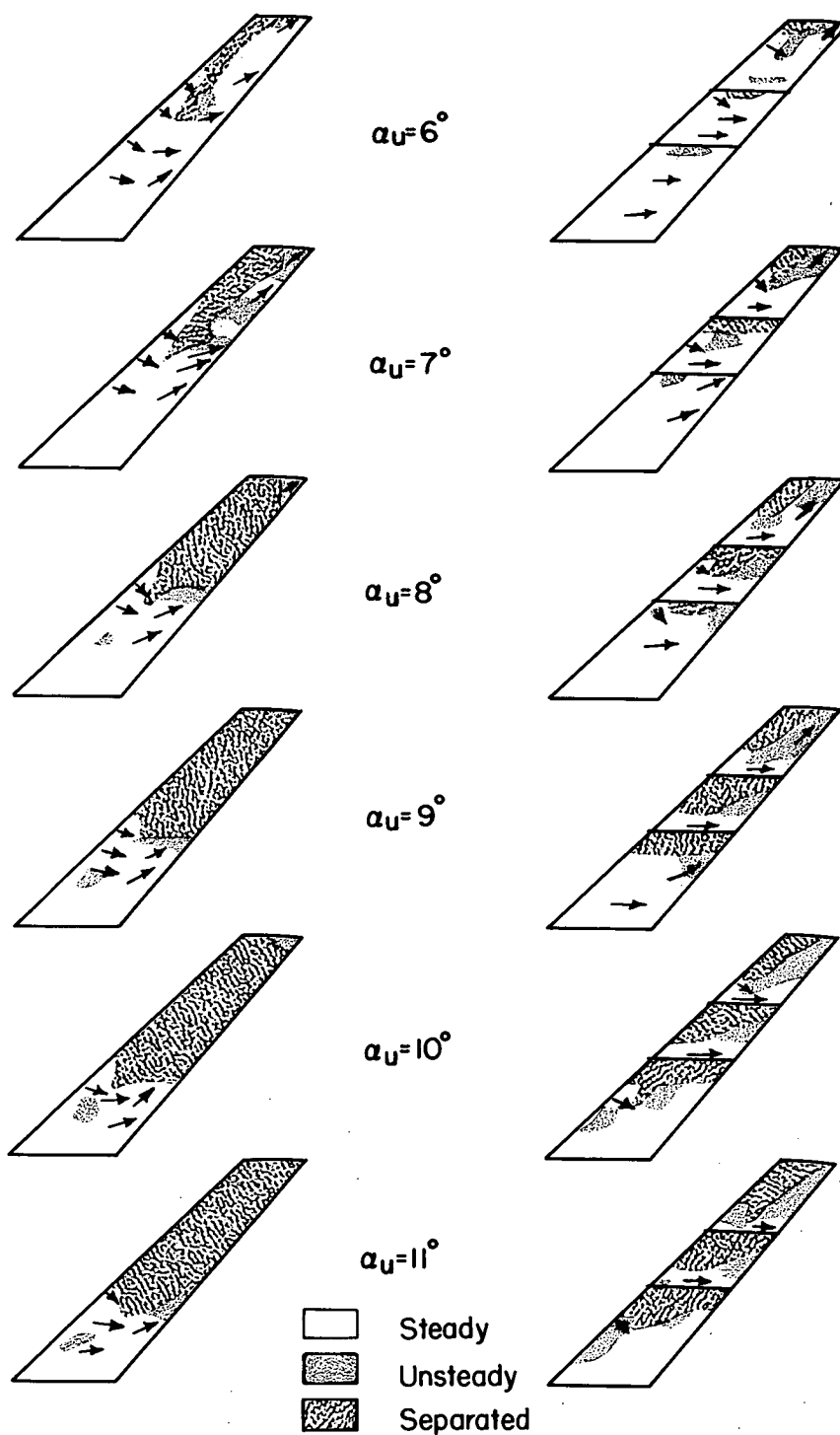


Figure 26.- Separation patterns on the wing, with and without fences;
 $M=0.90$; $R=2,000,000$.

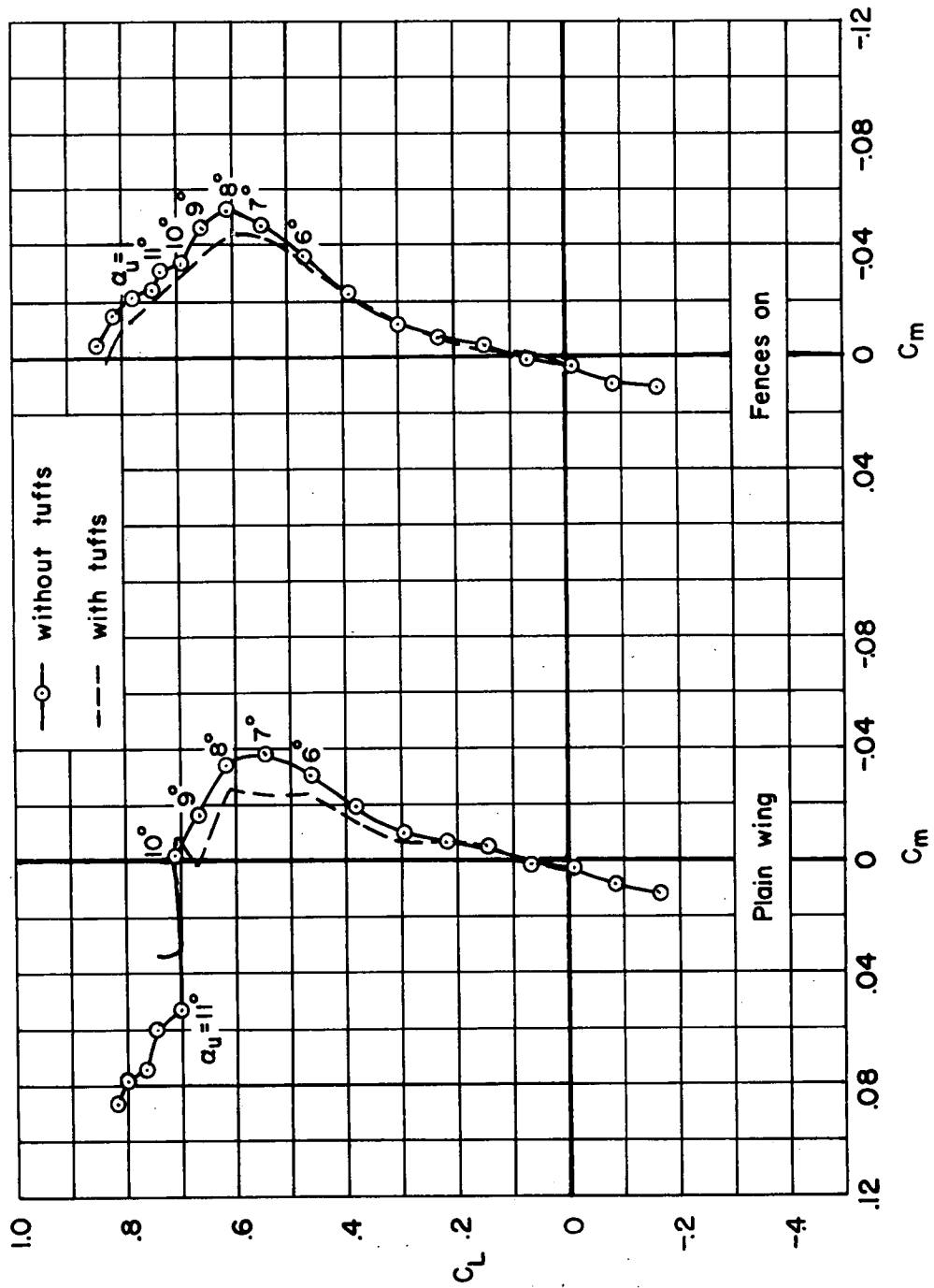


Figure 27.- Pitching-moment characteristics of the model with and without tufts; $M=0.90$; $R=2,000,000$.

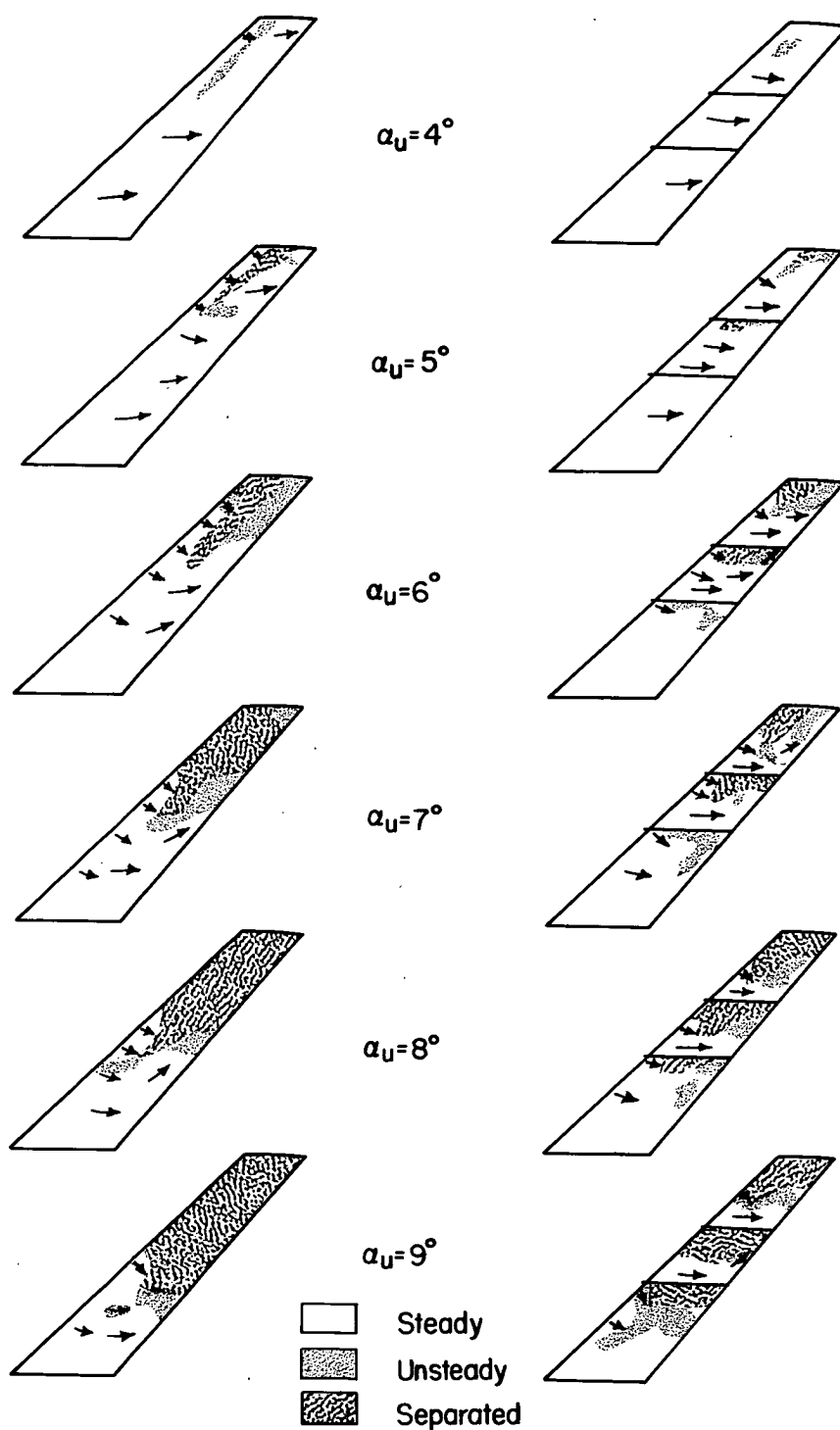


Figure 28.- Separation patterns on the wing, with and without fences;
 $M=0.92$; $R=2,000,000$.

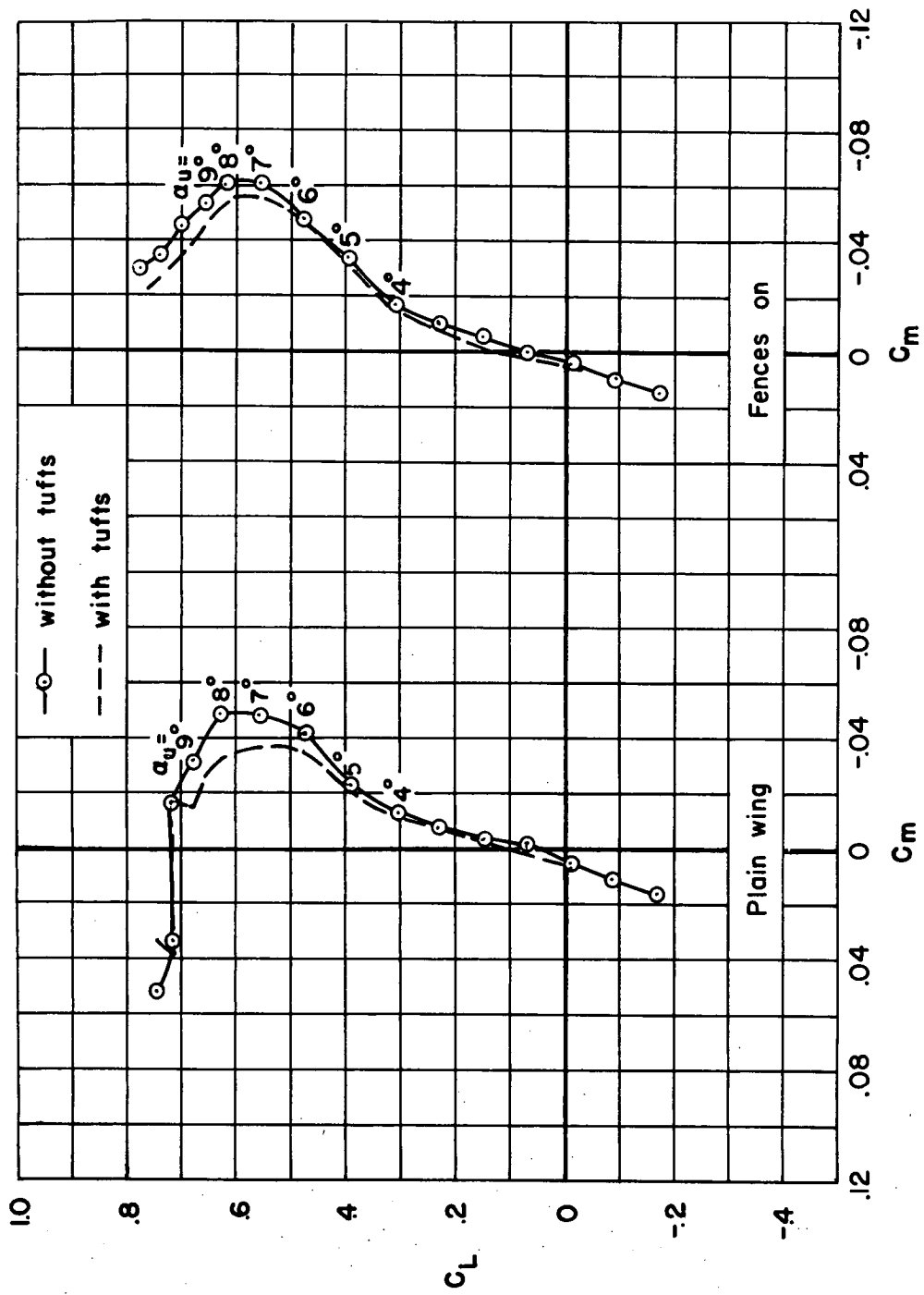


Figure 29.- Pitching-moment characteristics of the model with and without tufts; $M=0.92$; $R=2,000,000$.

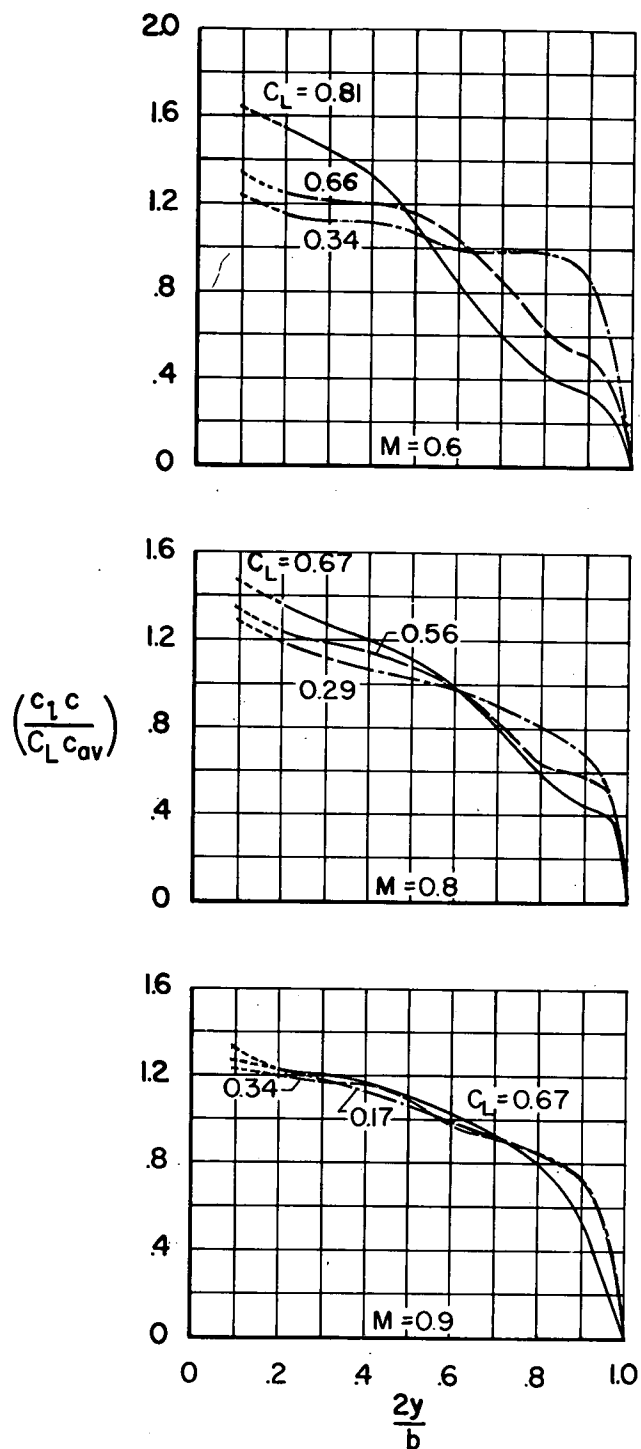


Figure 30.- Experimental spanwise loading for various lift coefficients.
Plain wing.

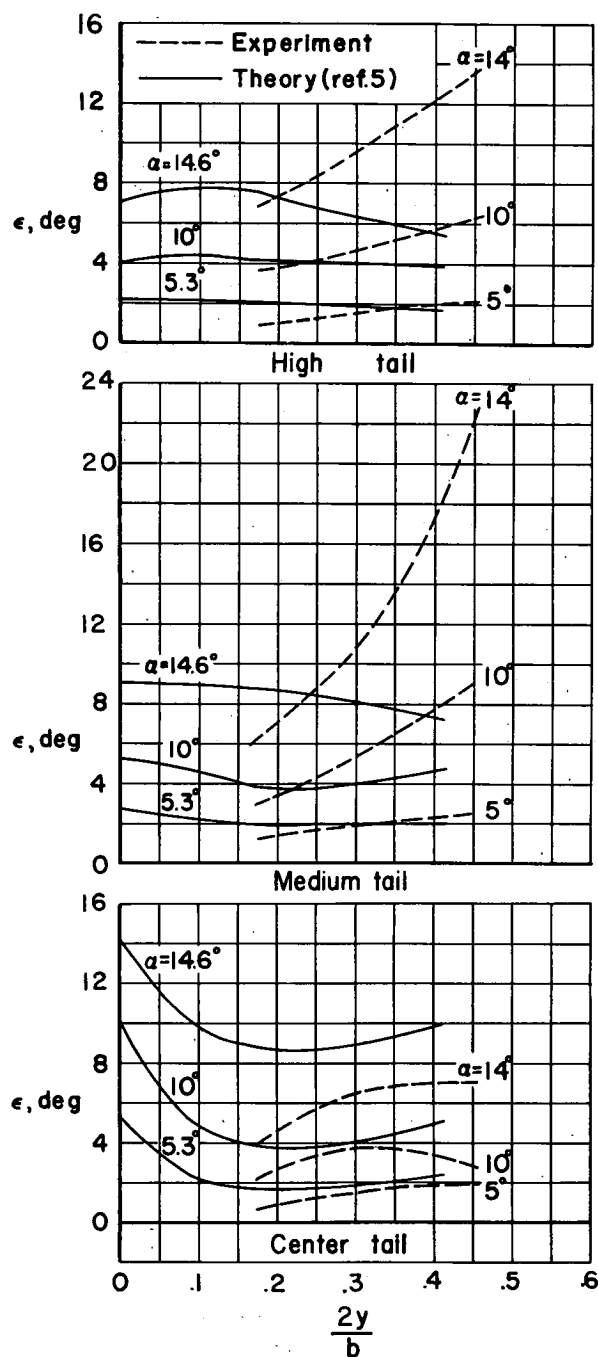
(a) $M=0.60$

Figure 31.- Comparison of the spanwise distribution of theoretical downwash (ref. 5) with measured local downwash at various angles of attack and at three vertical positions of the horizontal tail. Plain wing.

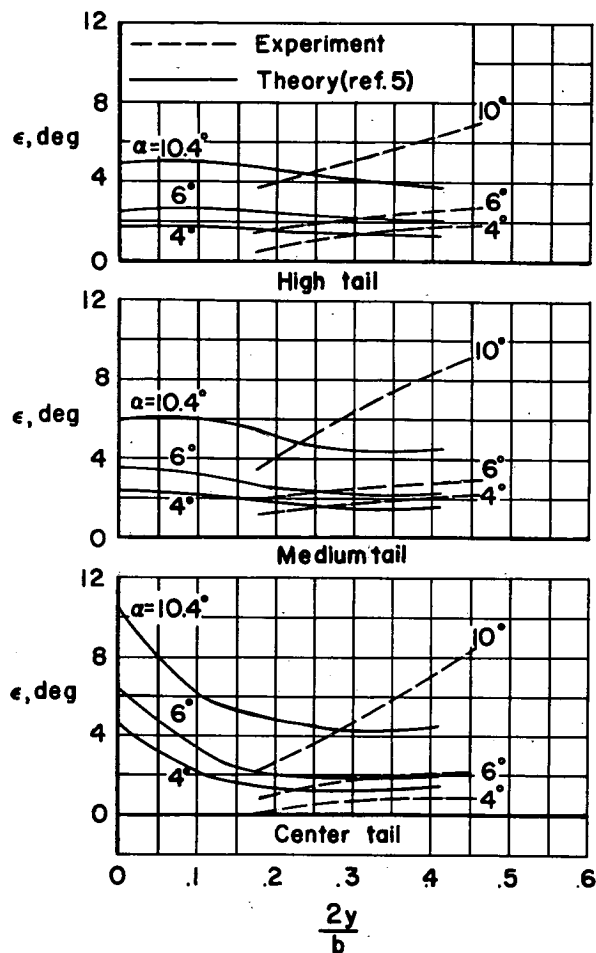
(b) $M=0.80$

Figure 31.- Continued.

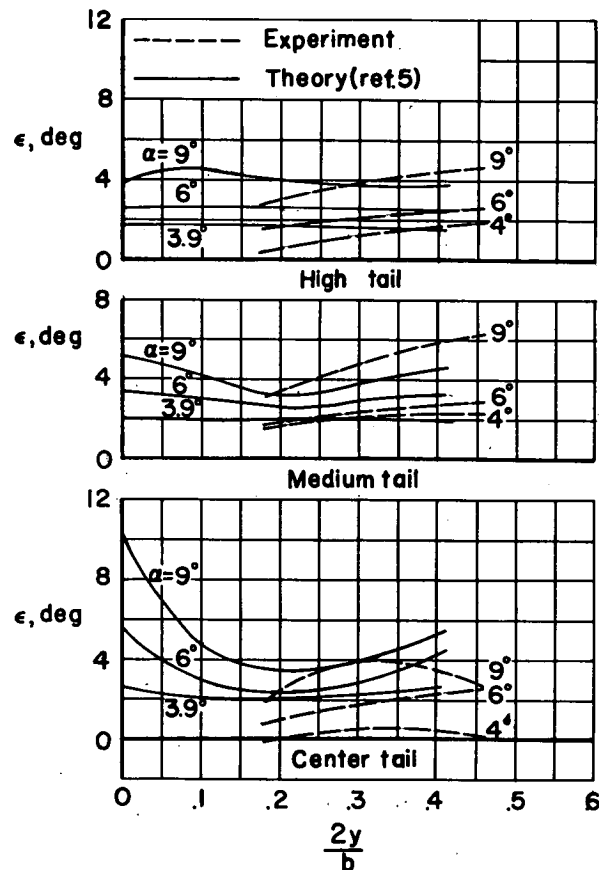
(c) $M=0.90$

Figure 31.- Concluded.

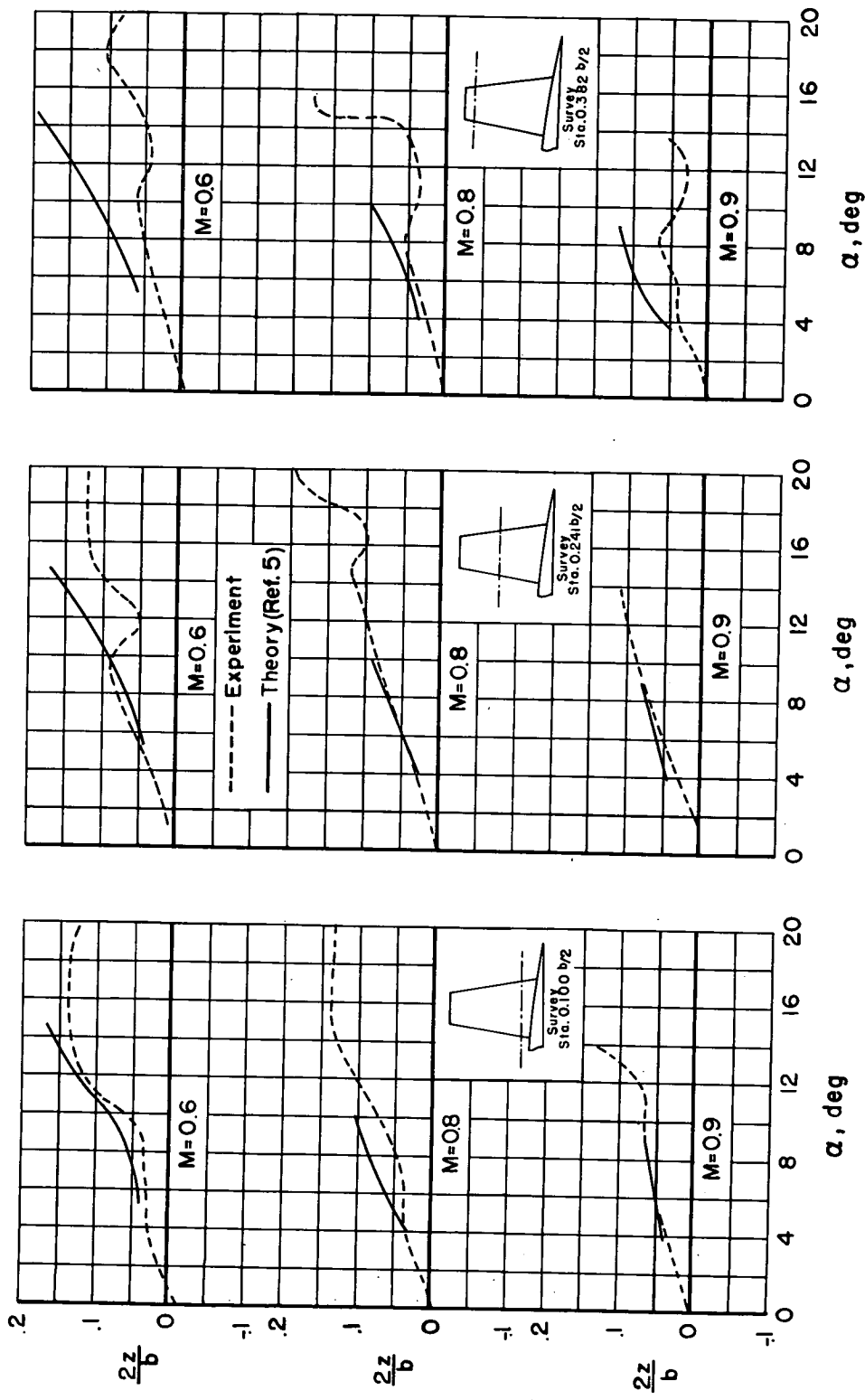


Figure 32.- The variations of theoretical and experimental wake-center location with angle of attack for three Mach numbers. Plain wing.

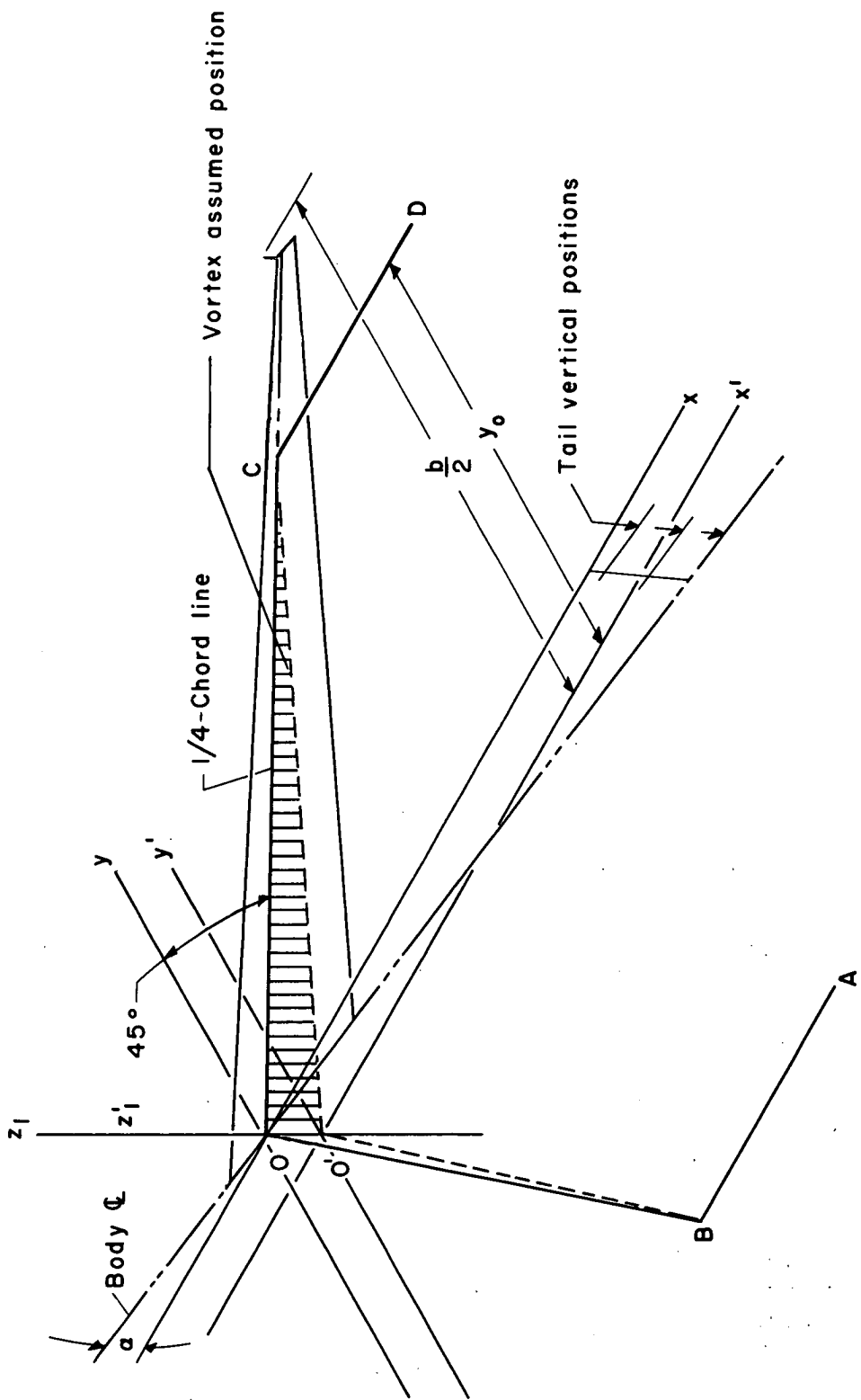


Figure 33. - Orientation of the swept vortex used in calculating downwash at the tail behind a 45° sweptback wing.

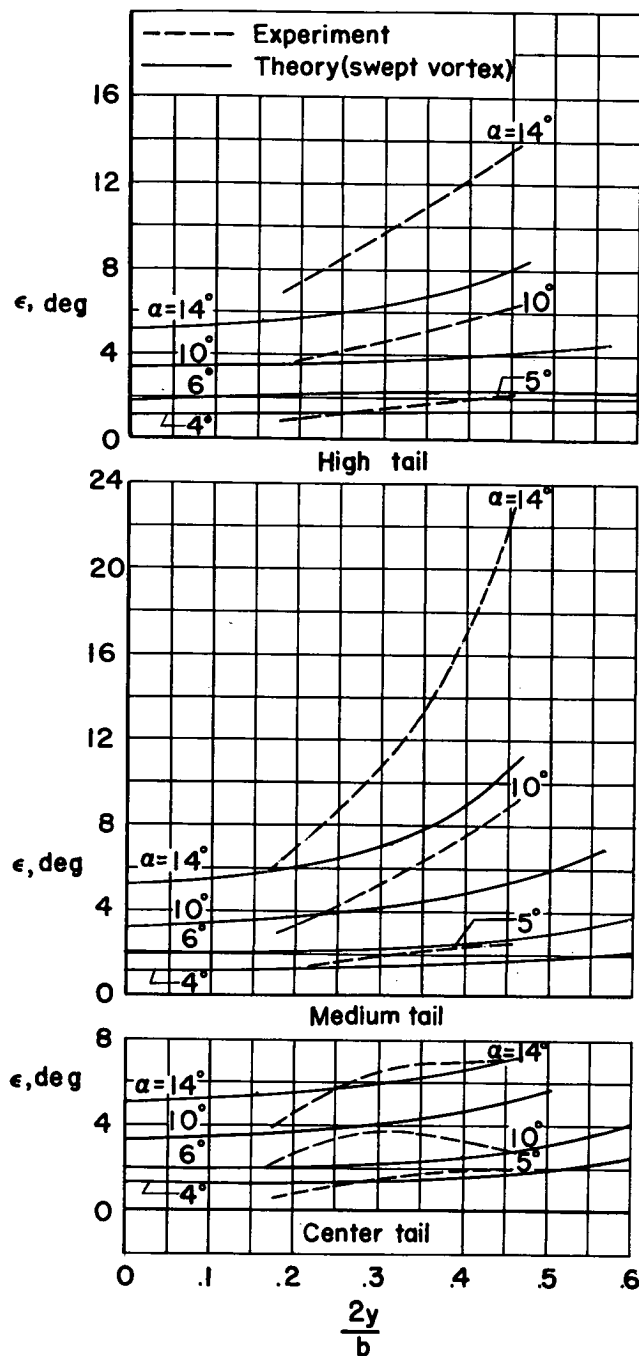
(a) $M=0.60$

Figure 34.- Comparison of the spanwise distribution of theoretical downwash (computed assuming a single swept vortex) with measured local downwash at various angles of attack and at three vertical positions of the horizontal tail. Plain wing.

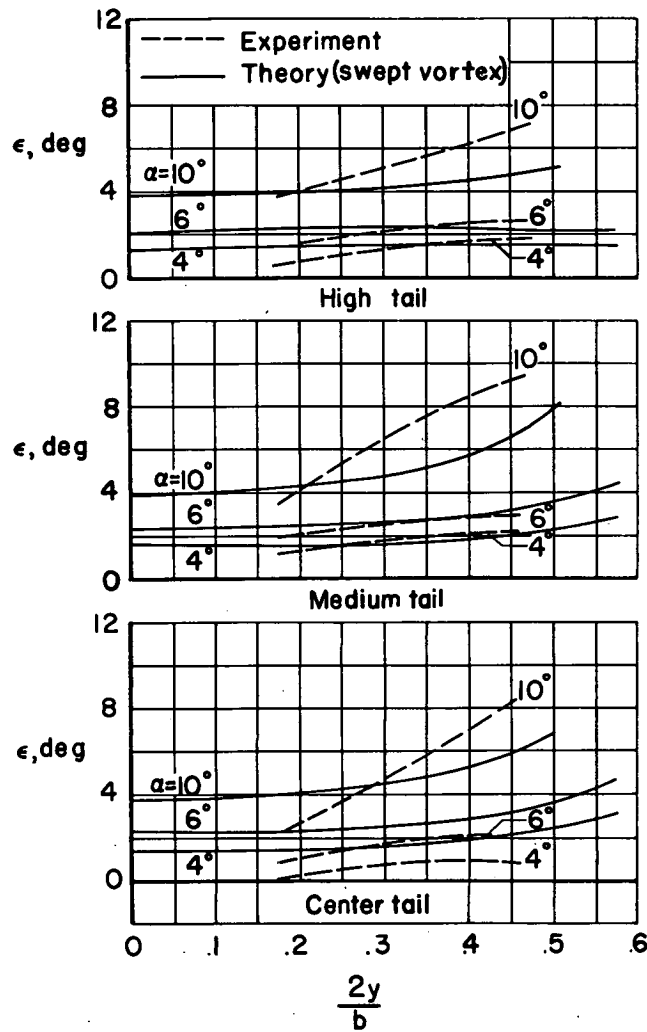
(b) $M=0.80$

Figure 34.- Continued.

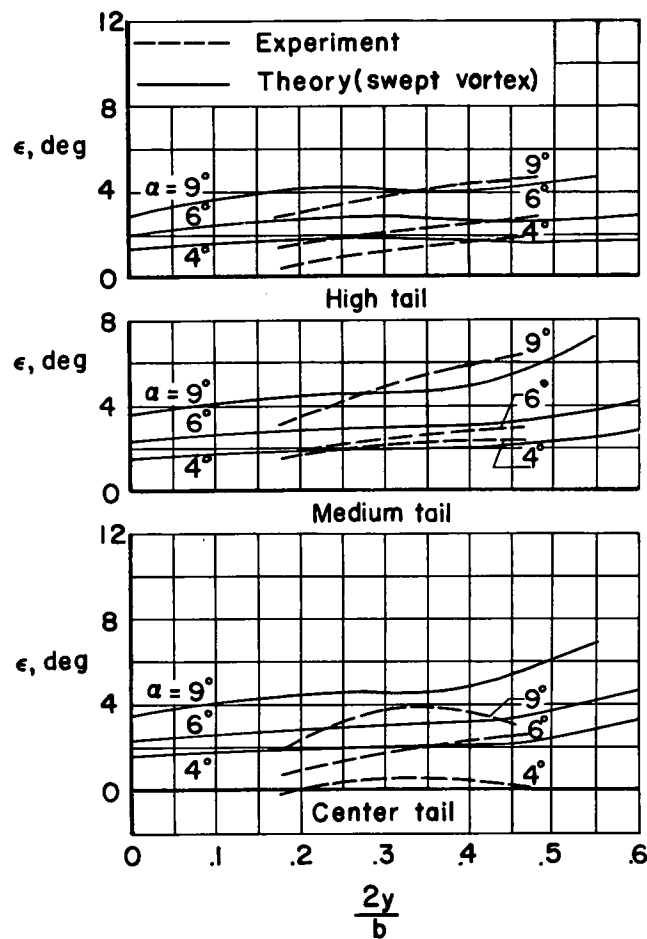
(c) $M=0.90$

Figure 34.- Concluded.